Design and Transformation of Three Dimensional Pupils: Diffractive and Subwavelength

by

Hanhong Gao

B.S., Peking University (2009)
S.M., Massachusetts Institute of Technology (2011)

Submitted to the Department of
Electrical Engineering and Computer Science
in partial fulfillment of the requirements for the degree of

Doctor of Philosophy in Electrical Engineering and Computer Science

at the

MASSACHUSETTS INSTITUTE OF TECHNOLOGY

June 2014

Author .....
Department of
Electrical Engineering and Computer Science
May 21, 2014

Certified by .....
George Barbastathis
Professor of Mechanical Engineering
Thesis Supervisor

Accepted by .....
Leslie A. Kolodziejski
Chair, Department Committee on Graduate Students

Design and Transformation of Three Dimensional Pupils: Diffractive and Subwavelength

by

Hanhong Gao

Submitted to the Department of
Electrical Engineering and Computer Science
on May 21, 2014, in partial fulfillment of the
requirements for the degree of
Doctor of Philosophy in Electrical Engineering and Computer Science

Abstract

Three dimensional pupils are investigated in both diffractive and subwavelength regimes and in various applications to shape the flow of light. In diffractive regime, volume holograms are good candidates for pupils of optical imaging systems thanks to their three–dimensional structure, which provides richer design flexibility compared to conventional two–dimensional pupils. In this thesis, I will propose the system design as well as the optimization of depth selectivity for enhancing the signal–to–noise ratio of ground–based imaging system for the detection of artificial satellites. In addition, deformations of volume hologram pupils promise additional opportunities to design further, more sophisticated point spread functions which are potentially useful for many imaging purposes. Deformations using multiple point indenters will be investigated in terms of both forward and inverse problems. Bulk transformation is a more general approach for pupil design. The physical relationship between transformation and resulting point spread function will be discussed by deriving the corresponding analytical expressions. In subwavelength regime, I will explore the realization of key materials properties including inhomogeneity and anisotropy. Anisotropy can be implemented by elliptical rod lattices; and with anisotropy, cloaking and accommodation of different components of an optical device become possible. Inhomogeneity is discussed in the context of gradient–index media. The additional thin–film wave guidance effect along the third dimension due to fabrication constraints is investigated in detail with the proposal of an all–analytical solution.

Thesis reader: Leslie A. Kolodziejski, Professor of Electrical Engineering, MIT
Thesis reader: Michael R. Watts, Associate Professor of Electrical Engineering, MIT

Thesis Supervisor: George Barbastathis
Title: Professor of Mechanical Engineering

Acknowledgments

First and foremost, I would like to thank the "lovely" 3D Optical Systems Group. You rock! Especially, I would like to thank my thesis advisor, Professor George Barbastathis, for his patient guidance and support for my research. He is very nice and is definitely a great professor. His instructions and suggestions have been extremely thought–provoking. Just like magic, his suggestions are especially helpful when I was stuck or struggling with difficulties. Also, I enjoy his jokes, admire his talent of languages and his ambition & vast progress in learning "one of the most difficult languages on Earth". I also thank him for teaching me how to pronounce correctly, write professionally, avoid common mistakes, and make fun/jokes in English.

I also appreciate the help, suggestion and criticisms from my committee members, Professor Leslie Kolodziejski and Professor Michael Watts. They offered great advice, and provided me with right paths towards my thesis. I thank for their patience when I had to routinely bother them to check their calendars and make my committee meetings and defense happen. I am also grateful to Professor Steven Johnson. His criticisms on my thin–film metamaterials project have been very useful. My appreciation extends to Professor Tomás Palacios as well, who, as my academic counselor, oversaw my PhD process and asked me to enjoy "the best time of your life."

As for our "3DOSG", I am very grateful to my nice, cute and supportive colleagues (past and present, MIT and Singapore) for their useful discussions, comments and kind help from every aspect: Disi A, Aditya Bhakta, Dipanjan Bhattacharya, Chih-Hao Chang, Wensheng Chen, Zhi Chen, Seongkeun Cho, Hyungryul Johnny Choi, Martin Deterre, Sagrario Dominguez, José A. Dominguez-Caballero, Yubo Duan, Chih-Hung Max Hsieh, Howard Yuanhao Huang, Hyun-Jin In, Jeong-gil Kim, Jason Ku, Justin Lee, Xiaogang Larry Liu, Yi Liu, Nick Loomis, Yen-Sheng Lu, Yuan Luo, Qin Miao, Anthony Nichol, Se Baek Oh, Adam Pan, Jon Petruccelli, Shakil Rehman, Nader Shaar, Yongjin Sung, Satoshi Takahashi, Chee Wee Tan, Kehan Tian, Lei Tian, Nikhil Vadhavkar, Laura Waller, Renze Wang, Jon Watson, Hongyi Xu, Kelli Xu, Se Young Yang, Baile Zhang, Zhengyun Zhang, and Yunhui Zhu. Among them,

I would especially thank Lei and Yi for suggestions and discussions on how to handle different research topics and the future, thank Zhi for lessons on experiments, Max and Satoshi for discussions on nanophotonics and fabrication, Jon (Jonathan Watson) and Scott (J. Scott Stuart) from Lincoln Laboratory for guidance and suggestions on the satellite project, Baile for helping in electromagnetics, Nick for computing guidance and American culture lessons, Laura for help on nonlinear optics, Se Baek and Jon for guidance in phase space optics, and our lovely Singapore crew (Yubo, Zhi, Zhengyun, Wensheng, and Hongyi) for offering me a place to stay. I also thank Irina Gaziyeva, Tuyet-Mai Hoang, Adiana Abdullah and Jaseema Abdul Karim for their help on paperworks and reimbursements. I appreciate the efforts from MIT International Students Office and Singapore's SMART headquarters on maintaining my legal status in both the United States and Singapore.

Last but not the least, I would thank my wife, Yue Wu. Being a spouse of a PhD student is definitely no easy task. This thesis would not be possible without her love, consideration and support. I would also like to thank my parents and parents-in-law for their support and love.

Contents

1 Introduction **21**

1.1 Volume holograms – 3D diffractive pupils 22

1.1.1 VH for satellite detection in daytime 26

1.1.2 PSF design: multiple point indenters 28

1.1.3 PSF design: transformational volume holography 29

1.2 Subwavelength metamaterials 30

1.2.1 Cloaking in subwavelength regime: anisotropy 31

1.2.2 Thin–film gradient index subwavelength metamaterials: inhomogeneity 32

1.3 Outline of the thesis 34

2 Volume holographic filters for mitigation of daytime sky brightness in satellite detection **37**

2.1 VHF system design 38

2.2 Telephoto objective 39

2.3 Analysis methodology 41

2.4 Mitigation of daylight due to longitudinal defocus 42

2.5 Multispectral issue and performance analysis 43

2.6 The SNR and design parameters 46

2.7 Discussion of multi–pixel cameras 49

2.8 Field of view (FOV) 51

2.9 Aberrations 52

2.10 Atmospheric turbulence 56

2.11 Experiment 60
2.11.1 Experimental geometry 60
2.11.2 Result: Case I 61
2.11.3 Result: Case II 62
2.11.4 Result: Case III 63
2.12 Conclusion 63

3 Design of volume holographic point spread functions using point deformations 65
3.1 From single to multiple point deformations 66
3.2 Continuous force 69
3.3 Multiple point deformations: examples 70
3.4 Inverse problem: optimization 70
3.5 Inverse problem: examples 73
3.6 Conclusion 75

4 Transformational volume holography 77
4.1 Volume holographic imaging systems 78
4.2 Transformation analysis 79
4.3 Affine transformations 81
4.3.1 Hologram shrinkage 81
4.3.2 Compression 83
4.3.3 Rotation 84
4.3.4 Shearing 85
4.4 Non–affine transformations 87
4.4.1 Bending 87
4.4.2 Stationary phase method 89
4.4.3 Twisting 95
4.5 Conclusion 101

5 Subwavelength dielectric photonic cloak **103**

5.1 Motivation 104

5.2 Implementation of anisotropy with elliptical rods 105

5.3 Cloaking and accommodating examples 106

5.3.1 Accommodation of peripheral non–photonic components . . . 106

5.3.2 Accommodation of internal non–photonic components 108

5.4 Gradient–index antireflection layers 109

5.5 Conclusion 111

6 Thin–film subwavelength Lüneburg lens **119**

6.1 Analytical method for effective refractive index estimation 121

6.1.1 Effective guiding medium (EGM) method 122

6.1.2 Relationship between effective refractive index and rod radius 126

6.2 Corrected design of the subwavelength Lüneburg lens 128

6.3 Anisotropic guidance correction 129

6.4 Conclusion 135

7 Conclusions and future work **137**

THIS PAGE INTENTIONALLY LEFT BLANK

List of Figures

1-1 (Left) Setup for volume hologram recording process. (Right) Example of recorded permittivity distribution on the hologram when $\theta_s = -\theta_f$. Color shading denotes the value of permittivity (see Eq. 1.4). 24

1-2 Setup for probing of recorded volume holograms. 25

1-3 Two types of subwavelength metamaterial lattices. Black dots are rods of certain material, e.g. silicon, and white ambient is other material, e.g. air. Red dashed lines highlight the corresponding unit cell of the lattice. 33

1-4 (a) Structure of designed subwavelength aperiodic nanostructured Lüneburg lens under 2D assumption. (b) Finite–difference time–domain simulation and ray tracing simulation results. Red circle outlines the edge of the Lüneburg lens and blue curves are ray tracing results. Black dots are silicon rods of infinite height (thus 2D assumption) immersed in air. Color shading denotes the field of the wave propagating through this subwavelength lens. 35

2-1 VHF design architecture. As an example, this VHF is assumed to be used for Iridium satellite detection. Inset: a typical diffraction efficiency plot with respect to longitudinal defocus δ. 38

2-2 (top) VHF system architecture using a telephoto as objective, and (bottom) its effective configuration. PP1: first principal plane. 40

2-3 Comparison of three computational methods for a simple VHF system architecture. 41

2-4 Diffraction efficiency of atmospheric scatterers for VHF system designed for Iridium satellite detection, calculated used analytical method (left) and MATLAB+ZEMAX method (right). 42
2-5 Diffraction efficiency of atmospheric scatterers for Geosynchronous detection VHF system architecture, calculated used analytical method (left) and MATLAB+ZEMAX method (right). 43
2-6 (a) Radiance of daylight scattering at different altitudes, (b) spectral radiance of the sky background at ground level, and (c) solar spectral irradiance. All figures are calculated using MODTRAN 4 [113] assuming 23 km ground visibility and rural extinction haze model. The angle was 10 degrees east of zenith at 3:00 PM local time on June 21 at 45 degrees latitude (mid–latitude summer atmospheric model). 45
2-7 Multispectral performance of the VHF system for probe source at different altitudes, calculated using (a) analytical method and (b) MATLAB+ZEMAX method. 46
2-8 (a) Signal diffraction efficiency, (b) noise diffraction efficiency, and (c) total system SNR enhancement with respect to hologram thicknesses and recording angles. 49
2-9 (a) Diffraction efficiency for satellites at different altitudes, when the system is solely designed for detection of Iridium satellites. Diffraction efficiency (I_d/I_0) is normalized to the readout intensity when the hologram is probed by Iridium satellites. (b) Turbulence–free point spread functions at multi–pixel cameras for satellites at different orbit heights. From left to right, top to bottom: Sputnik-1 (215 km), International Space Station (340 km), Hubble Space Telescope (595 km), and Iridium (780 km). Color shading denotes the normalized intensity. Note that different axes are used for these four pattern plots. 51
2-10 (a) Illustration of FOV along y direction; (b) Angle detuning along x direction. 52
2-11 Profiles of phase introduced by five main types of aberrations. 53

2-12 Diffraction efficiency at different longitudinal defocus for each type of aberration. Red curves are cases without aberration and blue curves are with aberration. The following values are used for the coefficient of each aberration: spherical aberration $B = 100$, astigmatism $C = 2 \times 10^3$, curvature of field $D = 5 \times 10^3$, distortion $E = 1 \times 10^4$, and comma $F = 50$. 54

2-13 (Top) Diffraction efficiency of objects at various altitudes for our VHF system considering spherical aberration (left) and astigmatism (right). Blue curves are without aberration, red and black curves are with aberration of different signs. (Bottom) Zoomed–in view of top row for objects with height below 30 km. Spherical aberration coefficients are chosen as $B = 10$ and $B = -10$, and astigmatism coefficients are chosen as $C = 4 \times 10^2$ and $C = -4 \times 10^2$. 55

2-14 Typical Zernike polynomials. When they are weighted by certain coefficients for each polynomial term, their summation gives the phase profile of atmospheric turbulence. 56

2-15 Examples of phase profiles for atmospheric turbulence at different values of FWHM of astronomical seeings. 58

2-16 Examples of point spread functions at the detector when probed by signal beams without defocus, for atmospheric turbulence at different values of FWHM of astronomical seeings. 59

2-17 Diffraction efficiency of objects at various altitudes for our VHF system considering atmospheric turbulence at different values of astronomical seeings. Left figure shows the entire range from 0 to 780 km, right figure is a zoomed–in at the altitudes of atmospheric scatterers from 0 to 30 km. 59

2-18 Scale down experimental geometry. BS: Beamsplitter, L1: Positive lens, L2: Negative lens, VH: volume hologram, TL: Tube lens. 60

2-19 (Left) Images from the conventional system (top, Camera 1) and the VHF system (bottom, Camera 2), with illumination from both satellite (monochromatic) and daylight (broadband). (Right) Line profile across the signal spot for both images. 62

2-20 (a) Contrast ratio comparison of the conventional and VHF systems with only satellite. (b) Contrast ratio comparison of the conventional and VHF system with both satellite and daylight. (c) Rate of contrast decrease after introducing daylight. (d) Images at detectors for the conventional (i) and VHF (ii) system with only satellite, as well as the conventional (iii) and VHF (iv) system with both satellite and daylight. 64

3-1 (a) Fourier geometry of reflection volume hologram. (b) PSF of geometry (a) with and without the point load. 67

3-2 (a) Imaging system geometry utilizing a reflection volume hologram. (b) Illustration of VH deformations with multiple point indenters. . . 68

3-3 Approximation of a continuous force using discrete point indenters, or vice versa. 69

3-4 (a)(b)(c) Three different kinds of desired PSFs normalized to the peak intensity of the PSF without deformation at Bragg matched probe beam $\theta_p = 172°$. (d)(e)(f) Combination of point loads to achieve the above PSFs, and the corresponding fringe patterns. Red dashed lines and blue solid lines denote the pattern before and after the deformation, respectively. (g)(h)(i) Angle detuning Bragg mismatched PSFs. The brightness plotted is the normalized intensity. 71

3-5 (Left) Designed PSFs, (middle) combinations of point loads, and (right) the corresponding fringe patterns for a shifted PSF. For fringe pattern plots, red dashed lines and blue solid lines denote the pattern before and after the deformation, respectively. 73

3-6 (Left) Designed PSFs, (middle) combinations of point loads, and (right) the corresponding fringe patterns for: (from top to bottom) wide rectangular PSF (Case I), wide rectangular PSF (Case II), narrow rectangular PSF. For fringe pattern plots, red dashed lines and blue solid lines denote the pattern before and after the deformation, respectively. 74

3-7 (Left) Designed PSFs, (middle) combinations of point loads, and (right) the corresponding fringe patterns for (top) PSF with narrowed main lobe, and (bottom) PSF with suppressed side lobes. For fringe pattern plots, red dashed lines and blue solid lines denote the pattern before and after the deformation, respectively. 75

4-1 Two analysis approaches for including bulk transformations in volume holographic imaging systems. For each case, left and right figures show coordinates used for calculating the integrals without and with the transformation, respectively. 80

4-2 (Left) Shrinkage of the VH along (a) z'' and (c) x'' directions. (Right) The resulting PSFs when the compression ratio (b) $\delta = 0.1$ & (d) $\delta = 0.02$, respectively. 83

4-3 (a) Rotation of the VH and (b) the resulting PSF when the rotation angle $\theta = 2^{\circ}$ calculated using both derived analytical equations and direct full numerical solution. 85

4-4 (a) Shearing of the VH along x'' direction and (b) the resulting PSF when the shearing ratio $\alpha = -0.04$. 86

4-5 (a) Bending of the VH. (b) Resulting PSFs at different bending ratios. 87

4-6 PSFs calculated using Eq. 4.32 by including the contributions (a) only poles and (b) both poles & boundaries, compared with full numerical solution. 91

4-7 Expressions of $f(x)$ (left), $\Lambda\phi(x)$ (middle) and real($\exp(i\Lambda\phi(x))$)(right) for one dimensional integral of Eq. 4.24 at detector positions of $x' = 0$ (top), $x' = -3.2 \times 10^{-4}$ m (middle), and $x' = -3.1 \times 10^{-4}$ m (bottom) (see Fig. 4-6). Note that only part of the integral range is shown. . . 92

4-8 PSF at the detector for a bent hologram calculated using stationary phase approximation combining four critical points, compared with full numerical solution. 95

4-9 (a) PSFs calculated from Part 1–3 and combined. (b)–(d) Contributions from Part 1–3 separately. 96

4-10 PSFs for twisting at different maximum twisting angles: (a) $\theta_m = 0^o$ (without deformation), (b) $\theta_m = 0.5^o$, and (c) $\theta_m = 1^o$. Note that in order to show sidelobes clearly, $\sqrt{q(x', y')}$ is plotted instead of the actual intensity, which is proportional to $|q(x', y')|^2$. 97

4-11 Intuitive explanation of the PSF shape after twisting. 98

4-12 Approximation of jinc function (Eq. 4.50). 100

4-13 (a) PSF calculated using stationary phase method approximation, and (b) its difference to the result calculated using full numerical result (Fig. 4-10(b)). Maximum twisting angle is $\theta_m = 0.5^o$. 101

5-1 Illustration of accommodating mechanical components into photonic components, reducing the size of optical elements. 104

5-2 Elliptical (a) and circular (b) silicon rod lattice structure. Isofrequency diagrams of silicon elliptical (c) and circular (d) rod unit cells, where only the first TM band is shown. The size of the unit cell is $a \times a$. The long and short axes of the elliptical rod in (a) are $0.95a$ and $0.5a$, respectively; the radius of circular rod in (b) was chosen as $0.294a$ to match the effective index of the isotropic circular rod case with the effective value of the index along the x axis in the anisotropic elliptical rod case. Labels on the lines denote the corresponding normalized frequency $\omega a/2\pi c$. The bold blue lines correspond to the free space wavelength $\lambda = 8a$ used in this thesis. 112

5-3 Space transformation of the first design example. More peripheral area (green) for accommodating mechanical components is created by squeezing the uniform medium into an anisotropic medium. Blue arrows are ray trajectories, and red lines illustrate wavefronts. 113

5-4 (a)(b) Original structure and the structure of the first design example. Blue boxes are the zoomed–in view of the lattices. Red lines denote the interfaces between different media: PEC, isotropic and anisotropic medium. (c)(d) FDTD results of original structure and accommodating design. Illumination is TM Gaussian source with incident angle of 45°. Black stripe is PEC and green stripe is area for accommodating mechanical components. Color shading denotes the magnetic field (H_z) distribution. Red is positive and blue is negative. 114

5-5 Transformation of space to create a parallelogram for accommodating internal mechanical components. Ray tracing results are illustrated. "Iso–" means isotropic and "Aniso–" means anisotropic. 115

5-6 Structure of the second design example, composed of uniform elliptical and circular silicon rod arrays. Grey parallelogram in the middle is region for mechanical components and magenta arrows are the optical axes of the anisotropic media. The dimensions are $D = 50a = 6.25\lambda$, $\alpha = 38.5°$ and $\beta = 13.3°$. Note that this implementation is for proof–of–concept and is definitely scalable. 115

5-7 FDTD simulation results of this design illuminated by plane wave with $\lambda = 8a$ at time $t = 6.25\lambda/c$, $12.5\lambda/c$, $18.75\lambda/c$, $25\lambda/c$, respectively. Color shading denotes the magnetic field (H_z) distribution, where red is positive and blue is negative. 116

5-8 Amount of reflection and scattering for diamond–shape cloak (Fig. 5-6) at different cloaking sizes (β angles) in (a) linear and (b) logarithmic scale. 117

5-9 One example of gradient–index antireflection layers, where four layers are used. 117

5-10 FDTD simulation results and sampled ray tracing of the photonic cloak without (a) and with (b) gradient–index antireflection layers. Ray trajectories for (a) are duplicated (black arrows) in (b) as a comparison to the trajectories for (b) (light blue arrows), illustrating the resulting lateral shift. Green lines illustrates the boundary or antireflection layers between circular and elliptical rod lattices. Color shading denotes the magnetic field [H_z] distribution. 117

5-11 Reflection coefficient (a) and lateral shift (b) with respect to the number of antireflection layers for different incident angles. Negative value for the lateral shift means a shift to negative–x direction from the correct position. 118

6-1 (a) Finite height rod lattice structure. (b) 2D rod lattice structure assuming infinite height. 121

6-2 Effective guiding medium (EGM) approximation of 2D finite height rod lattice structure. 122

6-3 Graphical solutions of wave guidance condition [Eq. (6.6) and (6.7)] for TE (a) and TM (b) polarizations. Blue and red lines are the left and right hand sides of these equations, respectively. Operating frequencies $\omega_1 = 0.11 \times 2\pi c/a$, $\omega_2 = 0.16 \times 2\pi c/a$, $\omega_3 = 0.14 \times 2\pi c/a$ and $\omega_4 = 0.18 \times 2\pi c/a$. Rod radius $r = 0.50a$. 124

6-4 (a) The supercell used in the DBD method for the finite height rod lattice structure. (b) Isofrequency contour of the supercell with $r = 0.50a$ where the first band only is shown. Labels on the lines denote the corresponding normalized frequency $\omega a/2\pi c$. The bold blue line corresponds to the wavelength $\lambda = 6a$ used in this chapter. (c) Field distribution of the waveguide slab at a particular x slice. Color shading denotes magnetic field (H_y) distribution and black contours illustrate silicon rods. 125

6-5 (a) Comparison between the dispersion relation for finite–height silicon rod lattice [Fig. 6-1(a)] calculated from the EGM and DBD method, and the dispersion relation for infinite–height 2D rod lattice [Fig. 6-1(b)]. For each case, the two lowest bands representing the TM and TE modes are shown. (b) Relationship between effective refractive index and rod radius calculated from both methods, compared with the relationship for infinite–height 2D rod lattice. Free space wavelength of light is $\lambda = 6a = 1550$ nm. 127

6-6 Relationship between calculated effective refractive index and height of the thin–film, at different polarizations and rod radii. 127

6-7 (a) Top view and side view of the thin–film subwavelength Lüneburg lens designed by EGM method for TE mode and (b) the corresponding 3D FDTD and Hamiltonian ray tracing results. (c) Top view and side view for TM mode and (d) the corresponding 3D FDTD and ray tracing results. Red circles outline the edge of Lüneburg lens, where radius $R = 30a$. Blue lines are the ray tracing results and color shading denotes the field [H_y for (b) and E_y for (d)] distribution, where red is positive and blue is negative. 130

6-8 Structure and the corresponding 3D FDTD and Hamiltonian ray tracing for the thin–film subwavelength Lüneburg lens shown in Fig. 6-7, but designed by the DBD method instead. 131

6-9 Structure and the corresponding 3D FDTD and Hamiltonian ray tracing for the thin–film subwavelength Lüneburg lens shown in Fig. 6-7, but designed using the EGM method without second–order terms when estimating the effective refractive indices. 132

6-10 FDTD and Hamiltonian ray–tracing results of the subwavelength Lüneburg lens made of finite height silicon rods, but designed assuming infinite height. The color conventions are the same as in Fig. 6-7(b&d). . . . 133

6-11 Polarization of electrical and magnetic fields while propagating along the thin–film under (left) TM–like and (right) TE–like polarizations. TE–like polarization results into an anisotropic effective medium. . . 133

6-12 Three–layer effective structure for a thin–film slab under TE–like polarization. The middle layer now becomes anisotropic effectively. . . . 134

Chapter 1

Introduction

Three dimensional (3D) optical pupils offer richer opportunities for shaping the propagation of light comparing with conventional two dimensional (2D) elements. The addition of the third dimension enables many novel system characteristics to be investigated, in the contexts of imaging, communications, etc. Often placed in the pupil plane (i.e. at the Fourier plane of a 4F system), these pupils are able to manipulate the resulting point spread functions (PSFs) of imaging systems with more design freedom. Typically, 3D pupils, especially in diffractive regime, result in a shift–variant system (a system where a shift/translation of the input along the lateral plane does not result in the same shift of the output), further enhancing the design flexibility.

Generally, 3D optical pupils function in two main regimes, diffractive and subwavelength. In diffractive regime, the operating wavelength is comparable or smaller than the feature of grating/lattice structures of the pupil. Diffractive elements typically operate by means of interference and diffraction in order to generate desired light distributions (in both amplitude and phase), or to aid the design of optical systems. While for subwavelength regime, the feature of elements is assumed to be much smaller than the wavelength of the light (thus "sub–wavelength"). As a result, light propagating through these devices only "sees" the effective ambient material properties, e.g. permittivity, permeability and (possibly) absorption. Complex three dimensional material distributions including inhomogeneity, anisotropy as well as dispersion can be realized by fine–tuning the structure of each subwavelength cell. These

optical pupils control the light in a fashion which is desired by the system.

In this thesis we will design and optimize some different 3D pupils, explore with various applications in both diffractive and subwavelength regimes. The main investigations can be classified into the following three categories:

- 3D diffractive pupils for cases when shift variance is desirable, e.g. detecting artificial satellites in daytime (Chapter 2).
- Transformation 3D diffractive pupils when shift variance and PSF manipulation are both desirable, e.g. transformational volume holography (Chapter 3 & 4).
- Subwavelength transformation pupils for cases when shift variance is not desirable but the PSF needs to be manipulated, e.g. anisotropic cloaks and Lüneburg lenses (Chapter 5 & 6).

1.1 Volume holograms – 3D diffractive pupils

Volume holograms (VHs) are 3D holograms where the thickness along the optical axis is not negligible so the Raman–Nath approximation does not hold. Instead, diffraction is said to occur "in the Bragg regime". VHs have been utilized in various applications, including signal processing [88, 109, 110], communication [28, 85], information storage [65, 66, 71, 87], and imaging [8, 120, 121, 122, 123, 133, 135]. Contrary to a conventional hologram, whose thickness is assumed to be negligible, typical VH thickness is in the order of millimeters.

VH is usually recorded by the interference of two plane waves: signal and reference beams with a certain angle, resulting in a periodic refractive index distribution [82]. A typical setup for the recording process is shown in Fig. 1-1. A signal point source is located at position x_s ($x_s < 0$). After the lens, this source beam becomes a plane wave of angle $\theta_s = -x_s/f_1$ where f_1 is the focal length of the lens. The signal field illuminated on the hologram is

$$E_s(x'', z'') = \exp\left[-i\frac{2\pi}{\lambda}\left(\frac{x_s}{f_1}x''\right)\right] \exp\left[+i\frac{2\pi}{\lambda}z''\left(1 - \frac{1}{2}\frac{x_s^2}{f_1^2}\right)\right], \tag{1.1}$$

where x'' and z'' are the coordinates centered at the hologram. Note that contributions from "y" components are ignored, since hologram setups are invariant along y'' axis in most of the following calculations. An exception is the twisting transformation discussed in Chapter 4, where the "y" components are necessary and thus included. Similarly, the reference field is

$$E_f(x'', z'') = \exp\left[-i\frac{2\pi}{\lambda}\left(\frac{x_f}{f_1}x''\right)\right] \exp\left[+i\frac{2\pi}{\lambda}z''\left(1-\frac{1}{2}\frac{x_f^2}{f_1^2}\right)\right]. \tag{1.2}$$

After the exposure, the permittivity of the holographic material is modulated according to the following relationship

$$|E_s + E_f|^2 = |E_s|^2 + |E_f|^2 + E_f^* E_s + E_f E_s^*. \tag{1.3}$$

Only the third term of the above expression is relevant to the read–out process. Therefore, by neglecting the other three terms, the permittivity recorded on the VH can be expressed as

$$\epsilon(x'', z'') = E_f^* E_s = \exp\left[i\frac{2\pi}{\lambda}\left(-x''\frac{x_s - x_f}{f1} + z''\frac{x_f^2 - x_s^2}{2f_1^2}\right)\right]. \tag{1.4}$$

This permittivity distribution has been illustrated in Fig. 1-1 in the case that $\theta_s = -\theta_f$. Note that the permittivity is modulated by the real part (cosine) of the interference pattern; but we write the permittivity distribution in analytic form to simplify subsequent calculations.

After the recording, this hologram is then probed with a probe beam (see Fig. 1-2). The optical field probing on the hologram is

$$E_p(x'', z'') = \exp\left[-i\frac{2\pi}{\lambda}\left(\frac{x_p}{f_1}x''\right)\right] \exp\left[+i\frac{2\pi}{\lambda}z''\left(1-\frac{1}{2}\frac{x_p^2}{f_1^2}\right)\right]. \tag{1.5}$$

Here we assume that the hologram is weakly diffracting, which is valid for most of the holograms we have been using. Thus, instead of the rigorous coupled wave theory [83], we can apply the first–order Born approximation; that is, the modulated material of

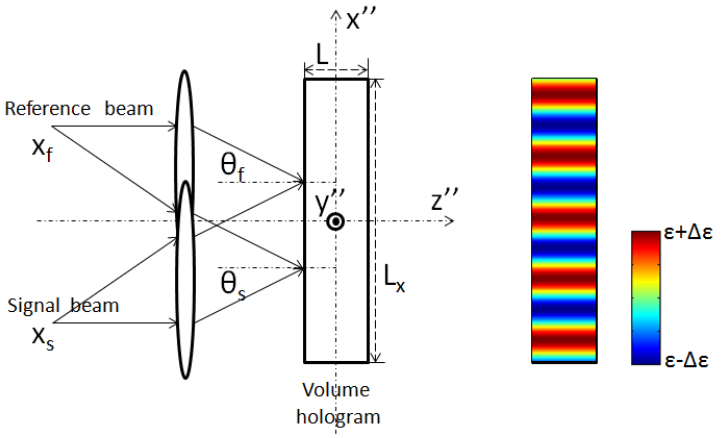

Figure 1-1: (Left) Setup for volume hologram recording process. (Right) Example of recorded permittivity distribution on the hologram when $\theta_s = -\theta_f$. Color shading denotes the value of permittivity (see Eq. 1.4).

the hologram responds to the probe beam illumination as a coherent superposition of secondary point sources of

$$g(x'', z'') = E_p(x'', z'') \times \epsilon(x'', z'') \tag{1.6}$$

at each (x'', z'') inside the hologram. The diffracted field is then collected by the second lens (also referred as collecting lens) of focal length f_2 and focused on the detector located at a distance of f_2 away. Barbastathis *et al* [8] and Sinha *et al* [124] have shown that the optical field on the detector can be calculated as

$$\begin{aligned} q(x') \;=\; & \iint E_p(x'', z'')\epsilon(x'', z'')s(x'', z'') \exp\left(-i2\pi \frac{x'x''}{\lambda f_2} \right) \\ & \cdot \exp\left[-i2\pi \left(1 - \frac{x'^2}{2f_2^2} \right) \frac{z''}{\lambda} \right] \mathrm{d}x''\mathrm{d}z'' \end{aligned} \tag{1.7}$$

where $s(x'', z'')$ is the hologram shape function and x' & z' are coordinates centered at the detector (see Fig. 1-2). Here we assume a rectangular volume hologram so

$$s(x'', z'') = \mathrm{rect}\left(\frac{x''}{L_x} \right) \mathrm{rect}\left(\frac{z''}{L} \right), \tag{1.8}$$

where L_x and L are the lengths of the hologram along x and z axes, respectively.

When the hologram is probed by a probe beam which is exactly the same as the previous reference beam, VH is Bragg matched and the identical signal beam will be read–out. Setting $x_p = x_f$, we can calculate the final field at the detector by solving Eq. 1.7:

$$q(x') = L_x \cdot L \cdot \mathrm{sinc}\left[\frac{L_x}{\lambda}\left(\frac{x_s}{f_1} + \frac{x'}{f_2}\right)\right]\mathrm{sinc}\left[\frac{L}{2\lambda}\left(\frac{x_s^2}{f_1^2} - \frac{x'^2}{f_2^2}\right)\right]. \tag{1.9}$$

Physically, the first sinc term corresponds to the finite lateral aperture of the hologram, and the second sinc term is a result of the non–negligible thickness of the hologram. The second term only appears when the pupil's thickness should be considered. This result also clearly indicates that volume holographic imaging systems are shift–variant.

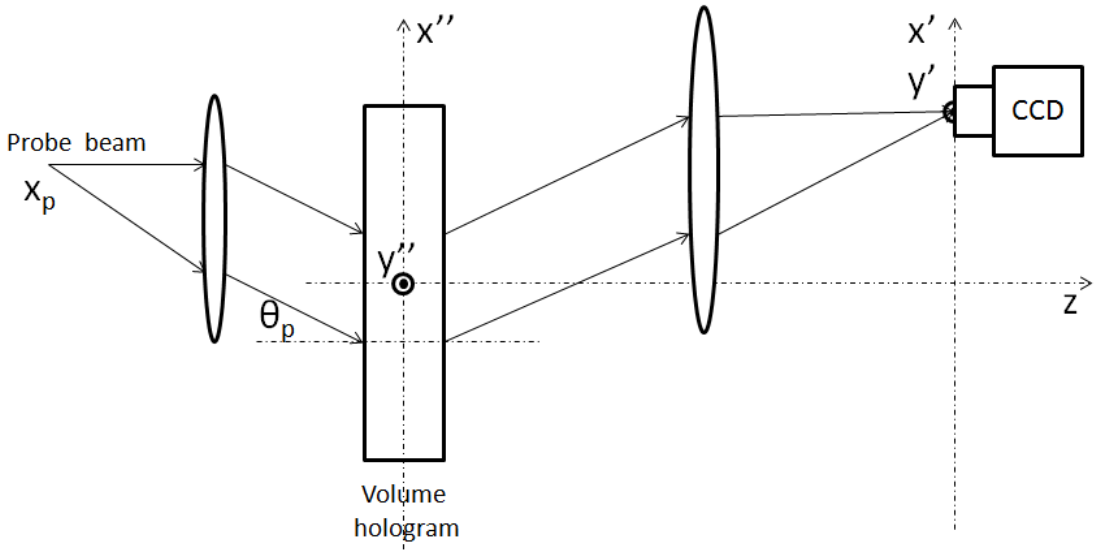

Figure 1-2: Setup for probing of recorded volume holograms.

However, when probed by beams different than the reference beam, VH is no longer matched thus the diffracted efficiency is reduced. Therefore, only those objects located very close to the objective plane have large enough diffraction after the VH; any objects at different depths experience minimal diffraction and thus are absent from the final image [11, 124]. This is the depth selectivity property, which is very useful especially in microscopy and other medical/biological imaging applications [7,

96, 97]. VH systems provide images of a sample at different depths simultaneously, thus depth scanning is not required any more.

VH is usually inserted into the pupil plane of an optical system to achieve desired system performance [103]. Pupil engineering in this scenario becomes VH engineering. By changing the VH, e.g. applying deformation, different system properties can be realized. Potentially if the VH can be adjusted *in vivo*, targets can be probed by different types of beams without changing system setup.

In addition, VH located at optical system's pupil plane can be deformed to achieve numerous point spread functions (PSFs). These PSFs are potentially useful for different applications, e.g. super–resolution imaging [107] and optical memory storage [87]. Possible deformations include point indenters, rotation, compression, bending, etc. This thesis aims at finding the relationship between the transformation of VH and the resulting PSF, especially in terms of analytical expressions.

Note that in this thesis we assume that the volume hologram has been recorded by two planes, and we do not focus on the detailed recording process of the hologram, including choice of hologram materials, possible wavelength responses, typical ranges of recorded permittivity, and robustness of the material in terms of multiple recording and reading processes. Detailed discussions on these topics have been covered in literature (for example, [96, 124]).

1.1.1 VH for satellite detection in daytime

For a ground–based optical telescope system operating in daytime, the majority of the background noise comes from sunlight scattered by the atmosphere within 30 kilometers (km) of the sensor [5, 74]. Our targets of interest, satellites, are a minimum of 200 km from the sensor. A volume hologram can be inserted into the observation system as a 3D pupil to provide the ability to selectively modify incoming light based on the range to the source, thanks to the depth selectivity property of VHs discussed above. We developed a design for the filter to use for suppression of daylight sky background, and modeled its performance against all the important design parameters.

Now the signal beam is from an object at the altitude of satellites. The recorded

VH is then probed to obtain an image. If the probe beam is from the object at the same altitude, VH is Bragg matched and provides the maximum diffraction efficiency. Otherwise, for atmospheric scatterers, i.e. at daylight, the beam after the objective lens is no longer a plane wave; thus, the hologram is Bragg mis–matched, resulting in a reduction of diffracted intensity. In this way, VH provides depth selectivity based on the distance of the probe source, and the daylight is then mitigated with reduced intensity.

However, because both the satellite and atmospheric scatterers are far away from the detector, the wavefronts illuminating on the system for both cases have no significant difference (i.e. far–away enough objects result into wavefronts close to plane waves). Therefore, satellite and daylight scatterers are indistinguishable in such a simple system. In this thesis, we present that a telephoto objective [15] should be used in this filter system to effectively reduce the front focal length, thus enhancing the depth selectivity at the orbit of the satellite target. A simulation method combining MATLAB®and ZEMAX®to perform the wave propagation and imaging is used to calculate the diffraction efficiency for objects at different altitudes [140]. Also, a method is presented to include the effects of the spectra of both sunlight and daylight; this approach is considered in the final calculation of signal–to–noise ratio (SNR) enhancement.

In this volume hologram filter system, six parameters have significant influence on the final system performance, including aperture radius, hologram thickness, recording angle, hologram refractive index, wavelength, and effective focal length. These parameters were optimized based on physically motivated system restrictions to maximize the SNR enhancement. In this process, the diffraction efficiency of atmospheric scatterers should be minimized, at a minimal cost of satellite efficiency reduction. The field of view of the total system will also be discussed, as well as the advantages of using multi–pixel detectors, which will further enhance the SNR and provide additional information on the types of satellites. Furthermore, aberrations as well as atmospheric turbulence will be investigated. Both of them result into a deformed wavefront on top of the existing system, and their amount and type determine their

effects on the final image quality. Kolmogorov model including Zernike polynomials will be used to model atmospheric turbulence [19].

1.1.2 PSF design: multiple point indenters

Volume holograms are inherently shift–variant and are able to provide richer opportunities for PSF design. In the previous satellite imaging case, VH is only inserted into the pupil plane of an imaging system. Because the interference pattern recorded on the hologram by two plane waves is of limited flexibility, the full 3D structure of the hologram is definitely not fully utilized. To achieve more flexibility, we present "3D pupil engineering", an analysis and design procedure for engineering the PSF by deforming exterior of a hologram. In this sense, both shift variance and PSF manipulation are desirable.

Here we propose to use multiple point indenters. Each point indenter applied on the exterior of the hologram induces a deformation of the fringes (permittivity distributions); the deformations from a combination of indenters can be used to design the desired PSF of an imaging system. Both the forward and inverse problems will be discussed. "Forward problem" provides the combination of point indenters, and we calculate the resulting PSF. A more interesting version is the 'inverse problem": given the required PSF, we calculate the possible superposition of point indenters.

Starting from a single point indenter, the elastic displacement inside the volume can be calculated [79, 134]. By analyzing the redistribution of refractive index pattern, final PSF is achieved through a 3D integration of the diffracted field. Based on this single indenter case, it is easy to extend this method to multiple point indenters at different positions. Each indenter results into an elastic displacement; the total deformation is approximately the superposition of the individual deformations (linear/elastic approximation). Here we assume that every point deformation is small enough that it can be treated as an independent perturbation. This analysis approach can be potentially applied to continuous forces as long as the continuous force can be well approximated in terms of multiple point indenters. In this way, continuous forces could be investigated with the same procedure.

For "inverse problem", a robust approach is "nonlinear least squares method". The difference between current–realized PSF and desired PSF can be minimized using least squares method to locate the best combination of point indenters. In this thesis, I will also discuss key points related to this approach which require special attention. We could decide a proper initial condition by utilizing the "forward problem" approach mentioned above. Note that although all the discussions are assuming a 2D system setup along $x - z$ plane, this problem is readily to be generalized to 3D. This thesis will present some interesting and potentially useful design examples.

1.1.3 PSF design: transformational volume holography

Not all PSFs are achievable by multiple point indenters. Fortunately, there are also more mechanical deformations besides point load, including compression, shearing, bending, twisting, etc. These choices of deformations provide richer opportunities for more general and sophisticated VH design. By transforming the volume hologram, i.e. the pupil of the imaging system, the system performance can be tuned to fit a design criterion such as spectral composition of the PSF, anisotropic behavior, etc. This general approach is called transformational volume holography.

Numerically, it is straightforward to compute the resulting PSF given a certain type of transformation. This is similar to the "forward problem" mentioned above using point deformations. However, these computations require integrations where the corresponding integrands are usually highly oscillatory. Thus, excessive sampling is required, especially in 3D, posing unattainable demands on extensive memory and CPU cost. In addition, a physically intuitive relationship between transformation of the VH and final PSF is not easy to find.

Therefore, in this part of the thesis, I will focus on finding quasi–analytical expressions for the relationship between transformation and resulting PSF. Analytical equations are always much easier to compute, and give better physical intuitions. For some of the transformations, especially affine transformations, analytical expressions are straightforward to derive and the relationship to the transformation itself can be observed clearly in the final expression. These transformations include compression

and extension, rotating, shearing, etc. However, for many non–affine transformations, e.g. bending and twisting, exact analytical solutions are not possible; instead we employ approximations.

We present the stationary phase method [16, 25, 30] to be a good solution for the approximation. Bulk transformation results in a Bragg–mismatched diffraction. This means that the expression inside the integral is fast oscillating in most of the hologram region except a few stationary points where the first–order derivative is zero. This satisfies the condition to apply stationary phase method. A simple and intuitive analytical solution can be derived in this case. Transformations including bending and twisting have been investigated.

1.2 Subwavelength metamaterials

For diffractive 3D pupils like volume holograms, the operating wavelength is comparable or smaller than the feature of grating/lattice structures. Here we will also discuss another important type of 3D pupils, subwavelength metamaterials, functioning in subwavelength regime, where the wavelength of light is significantly larger than the size of the lattice element. Unlike the diffractive case, here shift variance is not desirable but the system should have full capacity of manipulating light propagation.

Metamaterials [22, 27, 31, 37, 61] aim at design of artificial materials which possess properties not found in nature. Metamaterials are generally composed of periodic or aperiodic structures or cells that are much smaller than the operating wavelength of light. Metamaterials use small structures to mimick large effective macroscopic behavior [32, 126, 127]. Metamaterials have attracted attention in many research fields and applications. Interesting applications have been reported, including superlens [21, 93], negative refraction and perfect lens [3, 33, 39, 75, 107, 125], cloaks [38, 42, 98, 99, 118, 137], antennas [141], surface plasmons [13, 63], polarized beam generation [14], antireflection structures [81, 106], memory storage [35], as a number of interesting and important examples.

In this thesis, we focus on subwavelength metamaterials made of dielectrics. Dif-

ferent structures can be implemented to achieve various material properties including inhomogeneity and anisotropy. The key thing here is to find a particular design of cell unit in order to realize the required refractive index (or permittivity) distribution. Note that even though the subwavelength designs in this thesis are not in the pupil plane of a 4F system, these designs are steps in the direction of building 3D pupils in the future. We here focus on light manipulation. These subwavelength metamaterials discussed in this thesis typically do not have the shift–variant properties of a diffractive 3D pupil.

1.2.1 Cloaking in subwavelength regime: anisotropy

An important application of subwavelength metamaterials is cloaking. Invisibility cloaking device is a technology that can make objects invisible to an observer as if these objects do not exist. For example, a plane wave passing through the cloaked object is not scattered, but keeps the same plane wave fronts. Potentially, subwavelength cloaking devices can find many application in optics–on–a–chip and other integrated photonic devices. Invisibility cloaks have attracted a lot of research attention after the original ideas were proposed by Leonhardt [86] and Pendry [108]. Many designs and experiments have been carried out to realize cloaks operating at microwave [92, 118] and optical regimes [20, 38]. Implementations of these cloaks include metamaterials [20, 38, 42, 92, 94, 118, 137], layered structures [111] and so on. Recently, macroscopic cloaks operated at visible wavelengths have also been realized with natural materials as simple as calcite crystal [24, 148]. One important type of cloak is the ground–plane cloak, which is able to hide objects on a flat ground plane under a "carpet" as if these objects do not exist [90]. Through a transformation between the "physical space" and "virtual space", light illuminating the cloak is reflected in the same way as if the light were reflected by a perfect mirror. Transformations result in anisotropic material, which is generally considered difficult to implement in subwavelength regime. To avoid anisotropy, quasiconformal mapping was firstly applied to facilitate metamaterial fabrication of optical cloaks, resulting in slowly–varying inhomogeneous (but *isotropic*) medium [90, 137]. However, this map-

ping only minimizes (but does not eliminate) the anisotropy required; the omission of anisotropy in fabrication still led to a lateral shift at the output which makes the cloak detectable [147]. Also, the cloaking region designed using quasiconformal mapping was limited in size to the order of one wavelength, and inhomogeneity complicated the fabrication process.

In this thesis we discuss subwavelength nanostructured cloaking made of uniform elliptical rod arrays. This method conquers the key difficulty in the realization of cloak materials–anisotropy. Instead of trying to eliminate the anisotropy, our cloaking scheme instead utilizes anisotropic media, implemented as periodic structures of subwavelength elliptical rods. The proposed subwavelength structure consists of square unit cells with elliptical silicon rods immersed in air, which exhibits different effective refractive indices under illumination from different directions. This scheme greatly facilitates the fabrication process [132].

As an application of cloaking, our designed elliptical rod lattices are used to accommodate (i.e. cloaking) non–photonic components of an optical device with photonic components. A typical optical device is composed of the functioning photonic components and those non–photonic components which are used for support and connection of photonic parts. These two types of components usually have to be placed far away enough in order to minimize the influence of non–photonic components on the propagation of light, resulting into excessively large device sizes. Using our cloaking architecture to accommodate these two components together, the size of optical devices can be dramatically reduced without performance degradation.

1.2.2 Thin–film gradient index subwavelength metamaterials: inhomogeneity

Now we turn to the implementation of inhomogeneity using subwavelength metamaterials, in the context of gradient–index (GRIN) media [101]. Since at least Maxwell's time [130], GRIN media have been known to offer rich possibilities for light manipulation. More recent significant examples are the Lüneburg lens [26, 34, 67, 91, 95],

the Eaton lens [36], and the plethora of imaging and cloaking configurations devised recently using conformal maps and transformation optics [86, 108, 119, 128, 137, 138]. GRIN optics are of course also commercially available, but the achievable refractive index profiles $n(\mathbf{r})$ are limited generally to parabolic in the lateral coordinates or to axial without any lateral dependence [72]. There is an ongoing effort to achieve more general distributions using stacking of photo–exposed polymers [1, 117].

For optics–on–a–chip or integrated optics applications, using the idea of subwavelength lattice, it is possible to *emulate* an effective index distribution $n(\mathbf{r})$ by patterning a substrate with subwavelength structures. Because these structures are sufficiently smaller than the wavelength, to a good approximation these subwavelength structures can be thought of as a continuum where the effective index is determined by the pattern geometry. In general there are two different ways to realize subwavelength GRIN media: one can create a lattice of alternating dielectric–air with slowly varying period and fixed duty cycle, or with fixed period but slowly varying duty cycle [77, 114]. Examples have been illustrated in Fig. 1-3. For both lattices, rods can be replaced by other geometries, e.g. rectangles; and materials can be interchanged to make holes instead of rods.

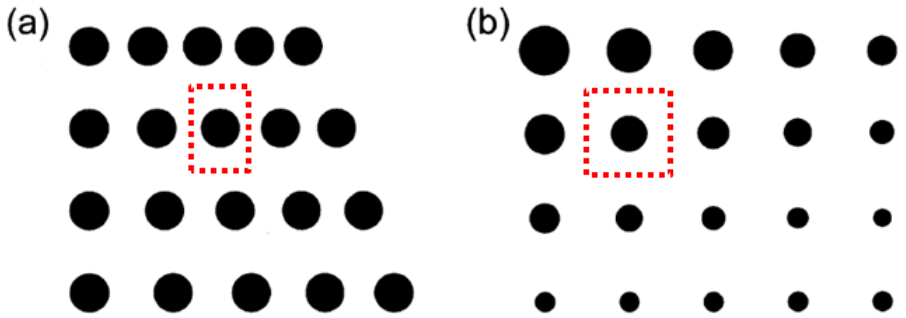

Figure 1-3: Two types of subwavelength metamaterial lattices. Black dots are rods of certain material, e.g. silicon, and white ambient is other material, e.g. air. Red dashed lines highlight the corresponding unit cell of the lattice.

If the critical length of the variation is slow enough compared to the lattice constant that the adiabatic approximation is valid, the lattice dispersion diagram can be used to estimate the local effective index [77, 114]. Refractive indices computed using a 2D approximation are valid for 2D adiabatically variant metamaterials where the

height in the third dimension is much larger than the wavelength so the assumption of infinite height can be justified. Under this 2D approximation, the relationship between geometry inside a unit cell and the effective refractive index (or permittivity) of the unit cell can be easily found. Two approaches can be applied here, one is a full–numerical band solving method in 2D, and the other is a 2D analytical solution. These approaches will be briefly discussed in Chapter 6.

According to the above assumption and analyzing approaches, we have designed a subwavelength aperiodic nanostructured Lüneburg lens [131, 132]. Fig. 1-4 shows one particular design and the corresponding verification using full–wave beam propagation and ray tracing simulation. This lens mimics a GRIN element with refractive index distribution $n(\rho) = n_0\sqrt{2-(\rho/R)^2}$ $(0 < \rho < R)$, where n_0 is the ambient index outside the lens region, R is the radius of the lens region and ρ is the radial polar coordinate with the lens region as origin. For the specific case of Fig. 1-4, optical wavelength $\lambda = 1550$ nm, size of unit cell $a_0 = (1/8)\lambda$, and radius of lens $R = 30a_0$. The Lüneburg lens focuses an incoming plane wave from any arbitrary direction to a geometrically perfect focal point at the opposite edge of the lens [95, 136]. This is also confirmed in Fig. 1-4(b).

However, for most fabricated subwavelength nanostructured devices, the height of the lattice is even smaller than the operational wavelength. The structure is now considered a thin–film waveguide and a large portion of the field exists outside of the slab itself. Clearly for these cases the 2D approximation discussed above are no longer valid, and the wave guidance effect should be taken into consideration when designing thin–film GRIN devices. We will propose an all–analytical approach to include this thin–film effect and re–design the subwavelength aperiodic Lüneburg lens.

1.3 Outline of the thesis

This thesis presents design and optimization of 3D imaging pupils in diffractive and subwavelength regimes. For diffractive elements, volume holography will be discussed in the application of daytime artificial satellite detection. Transformational volume

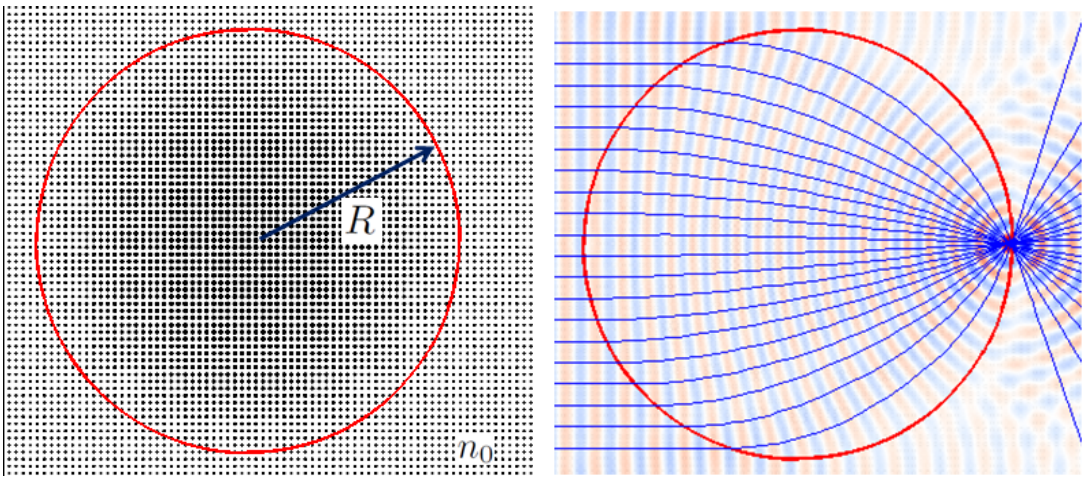

(a) (b)

Figure 1-4: (a) Structure of designed subwavelength aperiodic nanostructured Lüneburg lens under 2D assumption. (b) Finite–difference time–domain simulation and ray tracing simulation results. Red circle outlines the edge of the Lüneburg lens and blue curves are ray tracing results. Black dots are silicon rods of infinite height (thus 2D assumption) immersed in air. Color shading denotes the field of the wave propagating through this subwavelength lens.

holography is analyzed as a potential solution to the design of various PSFs by a simple transformation of the hologram shape. For subwavelength structures, we focus on the key realization of material inhomogeneity and anisotropy, in the contexts of gradient–index optical elements and cloaking devices. Subwavelength thin–film slab is analyzed in detail by introducing an all–analytical approach.

In Chapter 2, we present the design of a volume holographic filter system for the detection of artificial satellites in daytime, by including a telephoto as an objective. The parameters used in this system are optimized, including recording angle, size of the VH, etc., to achieve the best signal–to–noise ratio (SNR) enhancement. Its performance considering sunlight spectrum, optical aberrations and atmospheric turbulence is investigated and discussed. A table–top experiment is performed to confirm this design.

In Chapter 3, PSF design of volume holography systems using multiple point indenters is presented in detail. Both forward and inverse problems are discussed. In addition, we discuss the possible extension to a continuous force from multiple point

indenters, and vice versa.

In Chapter 4, transformational volume holography is presented. For affine transformation, an analytical solution for the resulting PSF is directly possible. However, for non–affine transformation, it is not possible any more and we turn to an analytical solution using the approximation of stationary phase method.

In Chapter 5, subwavelength elliptical rod lattices are discussed, which are used as a cloaking device to accommodate non–photonic and photonic components, reducing the size of a nanophotonic device. Two types of non–photonic components are accommodated: peripheral and internal.

In Chapter 6, in the context of GRIN lens, especially a subwavelength aperiodic nanostructured Lüneburg lens, the effect of fabricated thin–film waveguide structure has been evaluated. An all–analytical approach is presented and verified using rigorous numerical solutions to include the wave guidance phenomenon.

Chapter 2

Volume holographic filters for mitigation of daytime sky brightness in satellite detection

Observing solar–illuminated artificial satellites with ground–based telescopes in daytime is challenging due to the usually bright sky background. The majority of the background noise comes from sunlight Rayleigh–scattered by the atmosphere within 30 kilometers of the sensor [5, 41, 74]. The targets of interest, satellites, are a minimum of 200 km from the sensor. Thus, to enhance the signal–to–noise ratio (SNR) of satellite detection, our goal is to design a system which only images sources located at least 200 km from the sensor, but eliminates the light from nearby atmospheric scatterers. Volume hologram filters (VHF) provide the ability to selectively modify incoming light based on the range to the source, which are good candidates for this application. We built the mathematical models, optical models, and software necessary to model the behavior of a system comprising a telescope, re–imaging optics, a volume hologram filter, and a detector. In addition, we developed a candidate design for a VHF to use for suppression of daylight sky background, and modeled its performance as a functions of range to target, range to atmospheric scatterers, operating wavelength and bandwidth, and key recording parameters [45, 53, 54]. Effects caused by optical aberrations and atmospheric turbulence are also considered. A table–top

scaled–down experiment has been performed to verify this design.

2.1 VHF system design

Our design of the VHF system is illustrated in Fig. 2-1. The signal beam is from an object at the altitude of satellites, i.e. the sunlight reflected from the satellites, and the reference beam is at an angle θ_s with respect to the signal beam. The recorded hologram is then probed to produce an image. If the probe beam is from the object at the same altitude, the hologram is Bragg–matched and provides the maximum diffraction efficiency. Otherwise, for atmospheric scatterers, the beam after the objective lens is no longer a plane wave and is Bragg mis–matched, resulting in a reduction of diffraction intensity at the detector. In this way, the VHF provides depth selectivity based on the distance of the probe source (longitudinal detuning), and the intensity of the sky background is reduced.

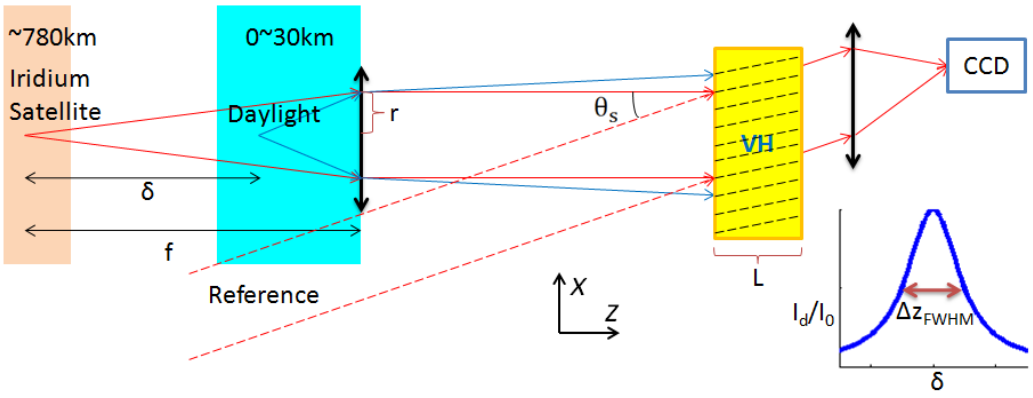

Figure 2-1: VHF design architecture. As an example, this VHF is assumed to be used for Iridium satellite detection. Inset: a typical diffraction efficiency plot with respect to longitudinal defocus δ.

A theoretical equation for calculating the diffraction efficiency of a VHF at various longitudinal defocus positions have been derived in [124]:

$$\frac{I_d}{I_0} = \frac{1}{\pi}\int_0^{2\pi} \mathrm{d}\phi \int_0^1 \mathrm{d}\rho\ \rho\ \mathrm{sinc}^2\left(\frac{aL\theta_s\delta}{n\lambda_f f^2}\rho\sin\phi\right), \tag{2.1}$$

where a is the aperture radius, L is the thickness of the volume hologram, n is the

refractive index of the hologram, λ_f is the recording wavelength, f is the focal length of the front lens, and δ is the longitudinal defocus of the probe source along the optical axis with respect to the position of recording signal source. The diffraction efficiency has its peak value when no longitudinal defocus exists, i.e. in Bragg–matched read–out. When the probe source point moves away from Bragg–matched signal source position, read–out efficiency is reduced. From the above equation, we could characterize the full–width at half–maximum (FWHM) of longitudinal defocus as

$$\Delta z_{\mathrm{FWHM}} = \frac{G\lambda f^2}{aL}, \tag{2.2}$$

where G is a certain constant. To better eliminate the daylight, its diffraction efficiency should be minimized. This means that the defocus of daylight scatterers δ, i.e. the distance between signal satellite and atmospheric scatters, should be at least larger than Δz_{FWHM}. However, we noticed that Δz_{FWHM} increases proportional to the square of lens focal length f. Since the satellites to be detected is at least 200 km away from the first lens, the f^2 term results in a Δz_{FWHM} value much larger than the longitudinal defocus (which is only comparable to f). In this way this simple VHF system architecture will not function as expected.

2.2 Telephoto objective

In order for the VHF to function, we need to minimize Δz_{FWHM} by decreasing the lens focal length f. However since the VHF has to be on the ground, and satellites have fixed orbits, the imaging distance could only be "effectively" reduced. A telephoto objective [15, 124] is a good candidate for this purpose.

A typical telephoto is comprised of two lenses, one positive and the other negative. As can be seen from Fig. 2-2, telephoto effectively reduces the working distance from

front focal length (FFL $= f$) to effective focal length (EFL), which satisfies

$$\frac{r}{a} = \frac{\text{EFL}}{\text{FFL}}, \tag{2.3}$$

where a is the aperture radius of the front lens, and r is the effective aperture radius, as illustrated in Fig. 2-2. With such a telephoto as objective, the FWHM of the longitudinal defocus becomes

$$\Delta z_{\text{FWHM}} = \frac{G\lambda(\text{EFL})^2}{rL}. \tag{2.4}$$

Effectively Δz_{FWHM} has been reduced by a factor of EFL/FFL. For example, when the focal lengths of these two lenses are chosen as 2.5 m and -2.5 mm, Δz_{FWHM} is reduced to 1/1000 of its original value with only a single lens objective. Therefore, longitudinal defocus of daylight scatterers can be larger than Δz_{FWHM}, effectively mitigate the daylight noise on the detector.

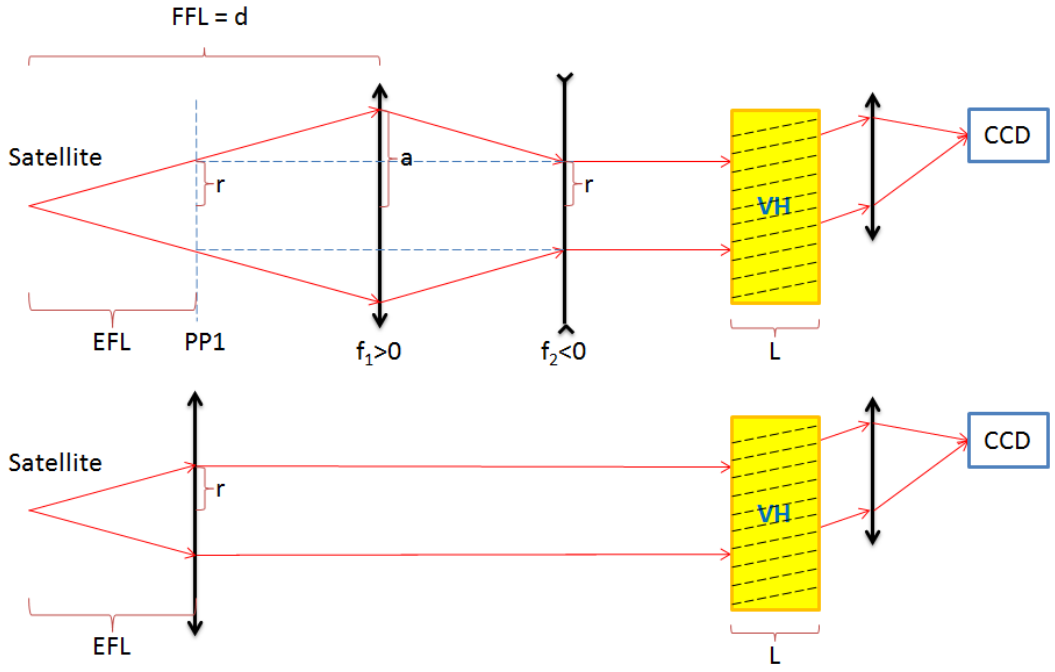

Figure 2-2: (top) VHF system architecture using a telephoto as objective, and (bottom) its effective configuration. PP1: first principal plane.

2.3 Analysis methodology

To explicitly calculate the daylight rejection, three methods are used. The first one is based on an analytical solution shown as in Eq. 2.1, which is similar to Equation (40) of [124]. The second method uses MATLAB®to calculate both the defocused wavefronts and recording/probing of the volume hologram, while the third method uses ZEMAX®instead to calculate the wavefronts [140]. From now on, we refer these three methods as "Analytical", "MATLAB only", and "MATLAB+ZEMAX" method, respectively. It is obvious that "Analytical" method is the fastest but most approximate, while "MATLAB+ZEMAX" method yields most accurate results but is computationally most expensive.

In order to demonstrate that all three methods yield reasonable results, we first applied them to a simple VHF system architecture with a single lens as objective, which is similar to Fig. 17 of [124]. Results are shown in Fig. 2-3, where we used the following parameters: $\lambda = 488$ nm, $L = 1.0$ mm, $a = 1.5$ mm, $\theta_s = 5^o$, and $f = 5.0$ mm. It can be observed that all three methods yield similar results. The discrepancy at large longitudinal defocus is mostly due to the finite size of detector used and numerical errors.

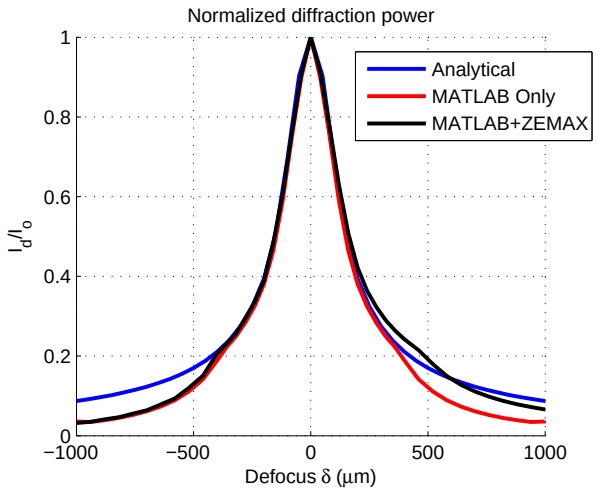

Figure 2-3: Comparison of three computational methods for a simple VHF system architecture.

2.4 Mitigation of daylight due to longitudinal defocus

Equipped with these three analysis methods, in this session we calculate the amount of attenuation of daylight in the VHF system architecture for satellite detection with telephoto objective. Without loss of generality, we aim at detecting Iridium satellites which are located approximately at a height of 780 km. Again here we assume that the majority of the daylight is scattered from atmosphere no higher than 30 km above the ground [74].

Here all the parameters used in this VHF for Iridium satellite detection are listed as follows: $\lambda = 632.8$ nm, $L = 1.0$ mm, $a = 1.0$ m, $\theta_s = 5^o$, $f_1 = 2.50$ m, $f_2 = -2.5$ mm, FFL = 780 km, EFL = 780 m. The reason we chose these values is discussed later. The reduction of daylight intensity is illustrated in Fig. 2-4, where we normalized the diffraction efficiency to the Bragg–matched readout with a probe beam from Iridium satellites. The results from two methods do not match but they both show large attenuation. The noise level of daylight has been lowered to 0.17 of its original value. The MATLAB+ZEMAX method even shows that 98% of the daylight has been eliminated. Again the discrepancy is a result of finite detector size and numerical errors.

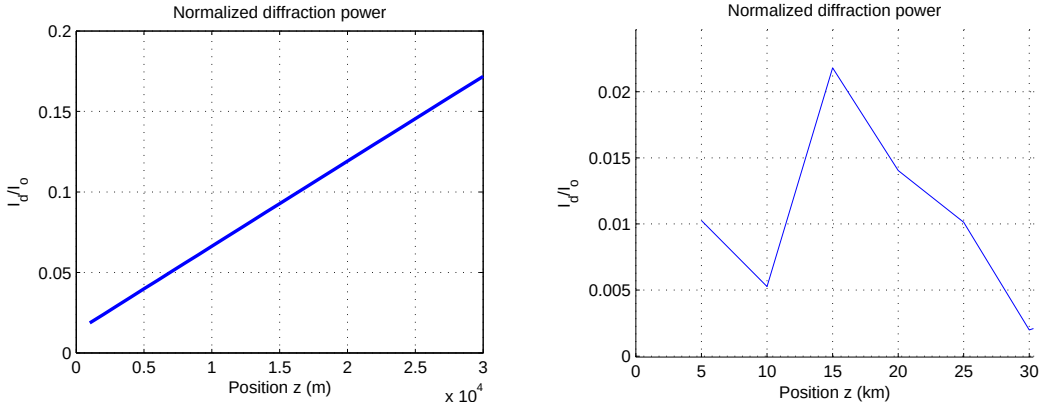

(a) (b)

Figure 2-4: Diffraction efficiency of atmospheric scatterers for VHF system designed for Iridium satellite detection, calculated used analytical method (left) and MATLAB+ZEMAX method (right).

The same design architecture can be applied to the detection of other types of artificial satellites located at different orbits. Here for illustration purpose we show another case with Geosynchronous satellites whose orbit has a height of about 35,786 km, much larger than that of Iridium satellites. Diffraction efficiency results for atmospheric scatterers are plotted in Fig. 2-5, where again a dominant attenuation can be seen, and 98% of the noise has been eliminated. Therefore, our system can potentially increase the SNR of satellite detection by dramatically reduce the intensity of noise from daylight.

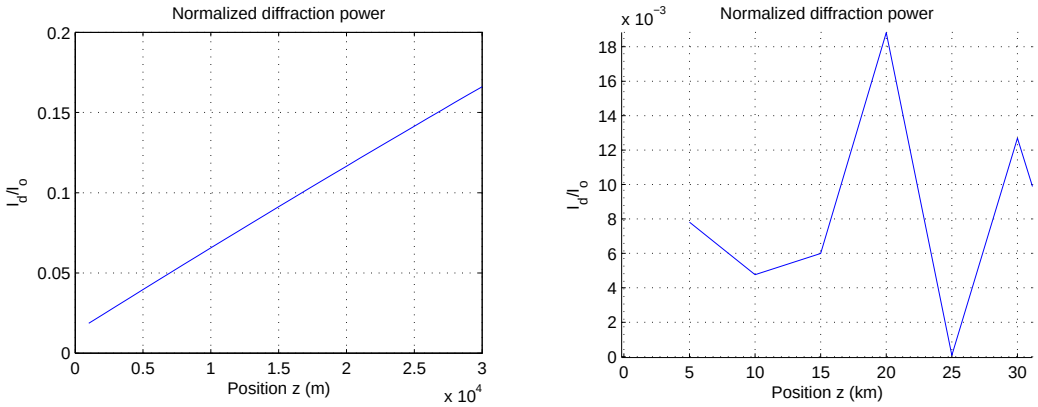

(a) (b)

Figure 2-5: Diffraction efficiency of atmospheric scatterers for Geosynchronous detection VHF system architecture, calculated used analytical method (left) and MATLAB+ZEMAX method (right).

2.5 Multispectral issue and performance analysis

Besides depth selectivity, volume holograms also perform wavelength selectivity, where the diffraction efficiency decreases when the wavelength of probe beam is different to the recording wavelength [11]. In our system, the hologram is recorded by a single wavelength; however, the sunlight reflected from the satellites and the daylight are both broadband, ranging at least from ultra-violet (UV) to infrared (IR). Among all the probe wavelengths, only certain combinations of probe angles and wavelengths are Bragg matched, resulting in reduced diffraction efficiency.

To characterize the relationship between diffraction efficiency and probe wavelength, we again use the three methods mentioned above, except that now we are scanning through wavelength instead of longitudinal defocus, and the equation used for analytical method should be derived as

$$\frac{I_d}{I_0} = \frac{1}{\pi}\int_0^{2\pi} \mathrm{d}\phi \int_0^1 \mathrm{d}\rho\ \rho\ \mathrm{sinc}^2\left(\frac{L\theta_s}{n\lambda_f}\left[\left(\frac{\mu}{2}-\frac{1}{2}\right)\theta_s\right]\right), \tag{2.5}$$

where $\mu = \lambda/\lambda_f$, the ratio between probe and recording wavelengths. Again we applied these three approaches to a simple VHF system architecture in the previous session and their results are in agreement. The multispectral performance of VHF system architecture for Iridium satellite detection has also been calculated, with the following parameters: $\lambda = 632.8$ nm, $L = 1.0$ mm, $a = 1.0$ m, $\theta_s = 12^o$, $f_1 = 2.5$ m, $f_2 = -2.5$ mm, FFL = 780 km, EFL = 780 m. The FWHM of bandwidth around the recording wavelength λ_f is only $0.03\lambda_f$, which means that majority of probe wavelengths are Bragg–mismatched thus the read–out efficiency of signal probe beam is very low. Therefore, multispectral performance should be seriously considered in our design in order to achieve a satisfactory performance.

To calculate the overall SNR enhancement of our VHF system, we need to calculate first the diffraction efficiency of both signal (satellite) and noise (daylight) probe beams. Here, without loss of generality, we assume that the detector has uniform sensitivity and is only sensitive along the visible spectrum. In terms of detectors with other sensitivity performance, the only modification we need is to multiply the sensitivity function during all the integrations below.

The multispectral performance of the VHF system, $q_{\mathrm{satellite}}(\lambda)$, can be centered at the working wavelength of 632.8 nm. The actual spectrum of satellite is similar to the spectrum of sunlight since satellite directly reflects the light from the sun. The sunlight spectrum is plotted in Fig. 2-6, which we denote as $p_{\mathrm{sun}}(\lambda)$. Daylight spectrum calculated by MODTRAN is also plotted as a comparison. It can be clearly seen that daylight has larger radiance around blue lights, confirming that the sky

appears blue. The overall diffraction efficiency for signal (satellite) is calculated as

$$\eta_s = \frac{\int_{\text{visible}} q_{\text{satellite}}(\lambda) \cdot p_{\text{sun}}(\lambda)\ \mathrm{d}\lambda}{\int_{\text{visible}} p_{\text{sun}}(\lambda)\ \mathrm{d}\lambda}. \tag{2.6}$$

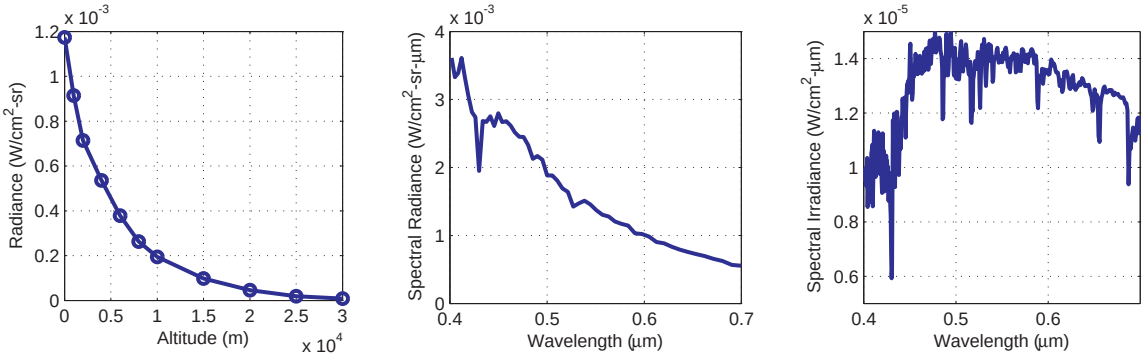

(a) (b) (c)

Figure 2-6: (a) Radiance of daylight scattering at different altitudes, (b) spectral radiance of the sky background at ground level, and (c) solar spectral irradiance. All figures are calculated using MODTRAN 4 [113] assuming 23 km ground visibility and rural extinction haze model. The angle was 10 degrees east of zenith at 3:00 PM local time on June 21 at 45 degrees latitude (mid–latitude summer atmospheric model).

Calculation of the efficiency of daylight noise is more complicated. First of all, because daylight is defocused longitudinally, the multispectral performance is different than un–defocused case. To illustrate this, we again have applied our three methods to the case with $\lambda = 632.8$ nm, $L = 1.0$ mm, $a = 1$ m, $\theta_s = 5^o$, $f_1 = 2.5$ m, $f_2 = -2.5$ mm, FFL = 780 km, and EFL = 780 m. It can be observed from Fig. 2-7 that the bandwidth is larger for larger longitudinal defocus. This figure also shows the multispectral performance of our Iridium satellite VHF system. Interestingly, since the longitudinal defocus for the daylight is so large, the daylight diffraction spectrum is almost flat (and low). Therefore, it makes sense to think that the multispectral issue of VH does not contribute to the daylight attenuation, leaving only longitudinal defocus to consider.

Another interesting phenomenon to be considered is the non-uniform daylight irradiance from scatterers at different altitudes, denoted as $r_{\text{daylight}}(z)$. As illustrated in Fig. 2-6(a), the irradiance decays exponentially for increasing scatterer altitudes,

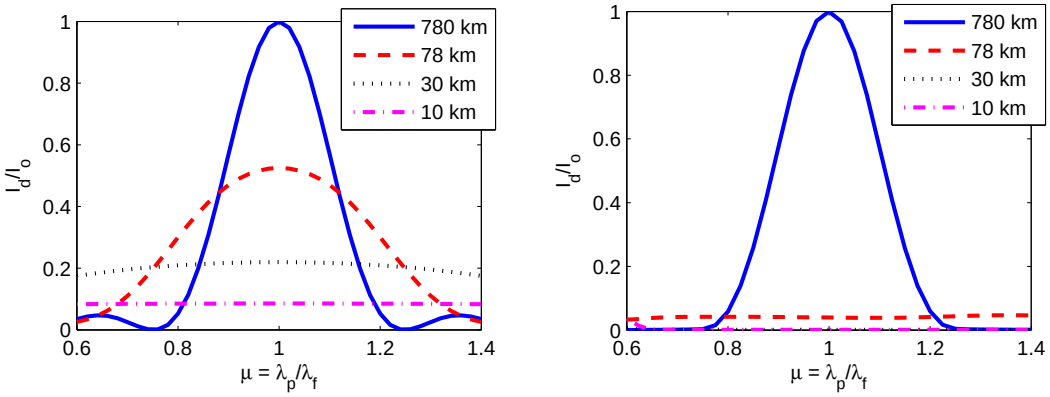

(a) Analytical (b) MATLAB+ZEMAX

Figure 2-7: Multispectral performance of the VHF system for probe source at different altitudes, calculated using (a) analytical method and (b) MATLAB+ZEMAX method.

where the contribution of scatterers higher than 30 km should be negligible. The overall diffraction efficiency for noise (daylight) is then calculated as

$$\eta_n = \frac{\int_0^{30\text{km}} q_{\text{daylight}}(z) \cdot r_{\text{daylight}}(z)\ \mathrm{d}z}{\int_0^{30\text{km}} r_{\text{daylight}}(z)\ \mathrm{d}z}. \tag{2.7}$$

To be more precise, we should remove the assumption of constant spectral performance for noise; and the overall diffraction efficiency becomes

$$\eta_n = \frac{\int_0^{30\text{km}} \int_{\text{visible}} q_{\text{daylight}}(\lambda, z) p_{\text{daylight}}(\lambda)\mathrm{d}\lambda \cdot r_{\text{daylight}}(z)\ \mathrm{d}z}{\int_0^{30\text{km}} \int_{\text{visible}} p_{\text{daylight}}(\lambda)\mathrm{d}\lambda \cdot r_{\text{daylight}}(z)\ \mathrm{d}z}. \tag{2.8}$$

2.6 The SNR and design parameters

As has been discussed above, the multispectral bandwidth problem is perfectly fine for daylight attenuation; however this also reduces the read–out efficiency of satellite probe signal.

The SNR enhancement is the metric we use to characterize the performance of the overall VHF system. Assuming that all other noises, such as electric noises, are

negligible comparing with the daylight, without the VHF system, the SNR is

$$\mathrm{SNR}(\lambda) = \sqrt{\frac{\lambda}{hc}} \frac{S_0^{\mathrm{satellite}}(\lambda)}{\sqrt{N_0^{\mathrm{daylight}}(\lambda)}}, \tag{2.9}$$

where h is the Planck constant and c is the light velocity. With the VHF system, the satellite probe signal and daylight noise have diffraction efficiency of η_s and η_n, respectively. The daylight noise hitting the detector is generally modeled by Poisson noise, whose standard deviations is a square–root of the expectation value. Therefore, although the amount of noise photons has been reduced to η_n of its original value, the noise level for detection purpose, after subtracting its expectation value, is only reduced to $\sqrt{\eta_n}$. That is to say, with the VHF system, the new SNR becomes

$$\mathrm{SNR}(\lambda) = \sqrt{\frac{\lambda}{hc}} \frac{\eta_s}{\sqrt{\eta_n}} \frac{S_0^{\mathrm{satellite}}(\lambda)}{\sqrt{N_0^{\mathrm{daylight}}(\lambda)}}. \tag{2.10}$$

Therefore, read–out efficiency of daylight noise η_n has to be larger than η_s^2 in order to make the VHF system perform at least better than the original system. In this sense, the efficiency reduction of probe signal due to multispectral behavior of hologram becomes unbearable. We thus need to design a VHF system with the largest bandwidth possible.

The key design parameters for our system have been listed in Table 2.1, together with their relationship to our two main performance considerations, daylight attenuation and multispectral bandwidth. This relationship was derived from the analytical equations shown above, and has also been verified with numerical calculations from MATLAB only and MATLAB+ZEMAX methods.

It can be seen from Table 2.1 that two parameters, aperture radius and EFL, are unrelated with the bandwidth. And the other four parameters have exactly opposite influence on daylight attenuation and bandwidth. Therefore we need to find a balance depending on our design requirements. Since for daylight attenuation we have two more parameters to play with, we here first optimize the bandwidth. As have been

Table 2.1: Requirements on design parameters for better system performance.

Design parameters	More daylight attenuation	Larger bandwidth
Aperture radius (a or r)	larger	unrelated
Hologram thickness (L)	larger	smaller
Recording angle (θ_s)	larger	smaller
Hologram refractive index (n)	smaller	larger
Wavelength (λ_f)	smaller	larger
Effective focal length (EFL)	smaller	unrelated

discussed previously, signal probe beam read–out should be as large as possible, thus we aim at a larger bandwidth.

(a) Wavelength and hologram refractive index

These two parameters are limited by the availability of laser sources and materials, and thus are actually not free to adjust. The sky background light in daytime is bluer than the solar spectrum reflected from satellites. In order to achieve better daylight mitigation, the VHF should be operated at longer wavelengths. Thus, we use red light with wavelength $\lambda = 632.8$ nm. As for the selection of hologram material, the hologram should not be erasable at readout wavelength so here we use phenanthrenquinone–doped poly(methylmethacrylate) (PQ–PMMA), a material that is particularly sensitive to wavelengths between 450 nm and 500 nm [97, 115]. A two–lambda approach can be used to record the hologram at 488 nm but actually designed for readout at 632.8 nm [10, 96, 97]. At readout wavelength, the refractive index of PQ–PMMA is 1.49.

(b) Aperture radius and EFL

These two parameters are unrelated to the multispectral performance to achieve better daylight attenuation. From Table 2.1, a larger aperture radius and smaller EFL are needed. Smaller EFL means a smaller r/a value since the FFL, i.e. altitude of satellites, is fixed. Thus, considering practical implementation, we chose the following parameters $a = 1.0$ m, $r = 1.0$ mm, $f_1 = 2.5$ m, $f_2 = -2.5$ mm, FFL = 780 km, EFL = 780 m, where the working distance has been increased 1000 times without deteriorating the depth selectivity.

(c) Hologram thickness and recording angle

These two parameters should be optimized to achieve a large system SNR. Using above equation derived, diffraction efficiency of signal and noise, as well as the overall system SNR enhancement have been calculated with respect to different hologram thickness and recording angle, illustrated in Fig. 2-8. Results show that θ_s should be small enough for large SNR. On the other hand, it should be large enough for easy system assembly. We here choose $\theta_s = 5^o$. At this recording angle, the largest overall SNR is realized when hologram thickness is $L = 0.5$ mm. For this optimized system architecture, $\eta_s = 0.74$, $\eta_n = 0.11$, and resulting overall system SNR enhancement is 2.2.

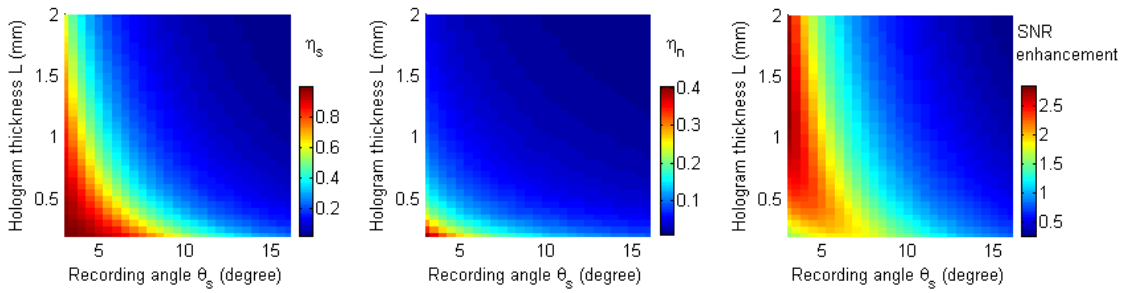

Figure 2-8: (a) Signal diffraction efficiency, (b) noise diffraction efficiency, and (c) total system SNR enhancement with respect to hologram thicknesses and recording angles.

The above SNR enhancement assumes that the detector is infinitely large. If we assume that the size of the detector is 1 mm–by–1 mm, using MATLAB+ZEMAX approach, we now have $\eta_s = 0.74$, $\eta_n = 0.0097$ and total SNR enhancement $\eta_s/\sqrt{\eta_n} = 7.5$. This value can be potentially increased by implementing multi–pixel cameras.

2.7 Discussion of multi–pixel cameras

All the above discussion assumes that the detector is a simple single–element power meter, where only the readout intensity or power (i.e. a number) is measured. How-

ever, an area detector with multiple pixels, such as a CCD, could be used to better facilitate our judgment of whether a true signal or a false alarm has been detected, and to estimate the distance to the satellite. The number of pixels used per detector is based on many practical issues, such as size of CCD, average power hitting each pixel, detector noise, etc. In this section, we discuss two advantages of using multi–pixel cameras.

(a) Increased SNR

When the volume hologram is probed by a signal beam from a satellite, the majority of the irradiance covers several adjacent pixels (see bottom right plot of Fig. 2-9(b)) of the multi–pixel camera; when probed by daylight, the diffracted intensity is more uniformly distributed on all the pixels. From fundamental statistics, the variance of a sum of independent random variables is the sum of their individual variances. Therefore, the noise variance of a measurement over a group of pixels increases approximately linearly with the number of pixels, and for each pixel, the individual noise level should be divided by the number of pixels. In this application the signal levels are high enough that CCD readout noise should always be negligible. Therefore, for the measurement of small signal and background levels the SNR is assumed to increase by the square root of the number of pixels. Thus the actual noise is much reduced compared with a single power meter detector. In this way better SNR is achieved.

(b) Estimating the distance to the target satellite

The VHF system is designed, without loss of generality, for detection of Iridium satellites located in orbit with altitude of 780 km. The exact same system architecture can also be used for detecting other satellites at other altitudes. The diffraction efficiency with respect to satellites at different orbit heights has been plotted in Fig 2-9(a). It can be observed that for satellites higher than Iridium, especially those in medium earth orbit (MEO) and high earth orbit (HEO), the readout efficiency can be more than 98%. However, for low earth orbit (LEO) satellites, the readout efficiency is not satisfactory. But in these cases, multi–pixel cameras can help. Multi–pixel

cameras produce an image of the defocused VHF readout rather than just a simple readout intensity. Satellites from different orbits produce patterns with different sizes and shapes. In Fig. 2-9(b), we have plotted the diffraction patterns for four different satellite distances. From the different defocus images, the distance to the satellite can be estimated, by template–matching, for example.

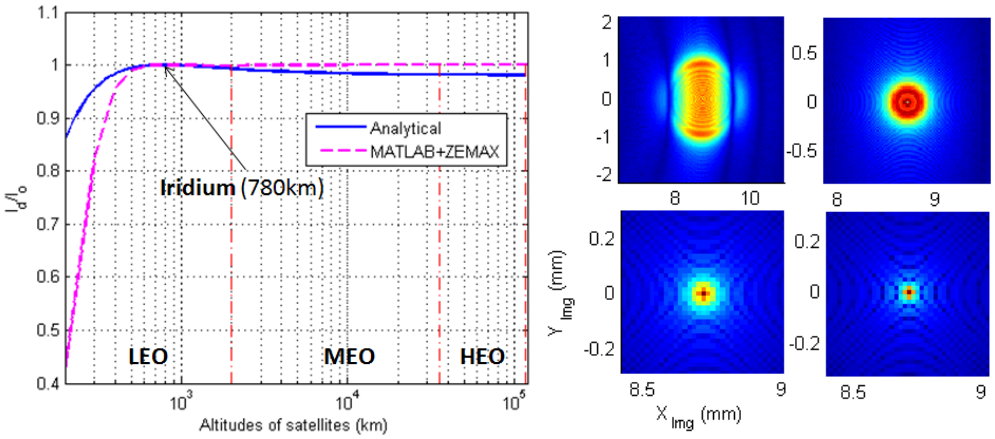

(a) (b)

Figure 2-9: (a) Diffraction efficiency for satellites at different altitudes, when the system is solely designed for detection of Iridium satellites. Diffraction efficiency (I_d/I_0) is normalized to the readout intensity when the hologram is probed by Iridium satellites. (b) Turbulence–free point spread functions at multi–pixel cameras for satellites at different orbit heights. From left to right, top to bottom: Sputnik-1 (215 km), International Space Station (340 km), Hubble Space Telescope (595 km), and Iridium (780 km). Color shading denotes the normalized intensity. Note that different axes are used for these four pattern plots.

2.8 Field of view (FOV)

To detect artificial satellites over the entire sky, scanning is required. In this way, concept of FOV is crucial. In this session FOV is discussed along two directions, x and y. The VH is invariant along y direction thus degenerated [124]. That is to say, no matter what the angle is for the probe beam, VH is always Bragg–matched. Therefore the FOV is determined by the actual system architecture shown in Fig. 2-10(a). This system will no longer work when the probe plane wave fails to hit either

the second lens of telephoto or the VH. That is to say

$$\alpha_y \cong \frac{\min(r_2, r_{\mathrm{VH}})}{s}. \tag{2.11}$$

Along x direction, another effect should be considered: angle detuning [124]. Angle detuning is similar to longitudinal defocus, where a probe beam illuminating the VH at different angles will no longer be Bragg–matched. For our VHF system architecture, the diffraction efficiency for different probe angles with respect to the original signal recording beam is illustrated in Fig. 2-10(b), where we observe a FWHM of 0.63 degrees. Therefore, along x direction, the FOV is determined by the smaller value between FWHM/2 of the angle detuning and α_x.

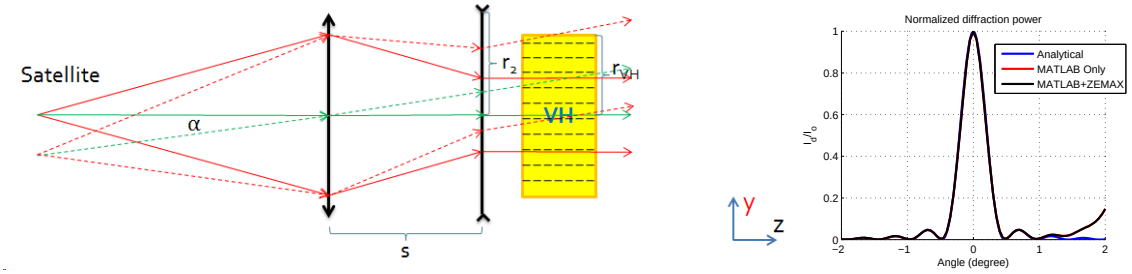

(a) (b)

Figure 2-10: (a) Illustration of FOV along y direction; (b) Angle detuning along x direction.

2.9 Aberrations

There are five main types of optical aberrations: spherical, astigmatism, curvature of field, distortion, and comma [15]. These aberrations are referred to as "Seidel" or (synonymously) "3rd order." There are other higher order aberrations which are not important for the small numerical apertures we are dealing with here. The optical phase profiles introduced by these different types of aberrations are shown in Fig. 2-11. We could observe that spherical, astigmatism and curvature of field provide "quadratic–like" phase changes, though not exact. Among them, both spherical and curvature of field give circular phase profile while astigmatism gives phase changes

only along one particular direction. On the other hand, distortion and coma introduce "linear–like" phase changes.

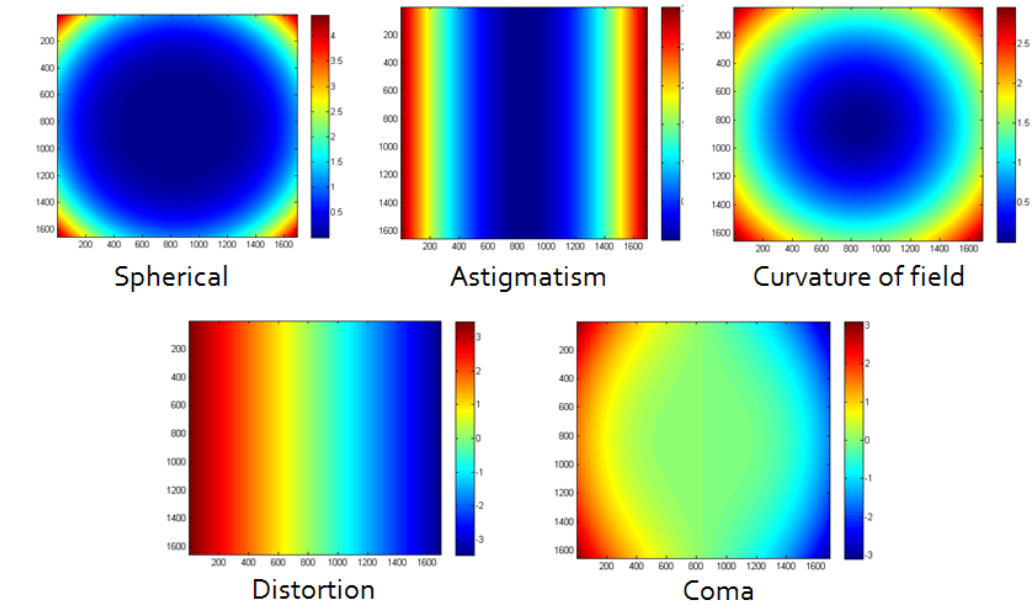

Figure 2-11: Profiles of phase introduced by five main types of aberrations.

In order to demonstrate how each type of aberration affects the final system performance, we first apply them to a simple VHF system architecture with a single lens as objective, which is similar to Fig. 17 of [124]. The parameters are set as follows: $\lambda = 632$ nm, $L = 1.0$ mm, $a = 1.5$ mm, $f = 5.0$ mm, $n = 1.50$, $\theta_s = 5^o$. Diffraction efficiency at different longitudinal defocus for each type of aberration is show in Fig. 2-12. It can be observed that for the first three aberrations the peak of curve shifts to a different longitudinal position. This is because these three aberrations, as have been mentioned above, introduce "quadratic–like" phase profiles which are similar to a spherical wave. These phase profiles are able to partially "cancel out" the phase profile of a spherical wave introduced by longitudinal defocus. Thus the peak shifts. Also, this additional phase change cannot exactly match that of the spherical wave, meaning that the introduction of aberration will not allow for the volume hologram to be probed under a Bragg matched condition; thus the peak value of diffraction efficient is lowered in all three cases. As for distortion and coma, the introduction of "linear–like" phase profiles have no impact on the longitudinal defocus, except an

introduction of Bragg mismatch especially when defocus is zero. So the peak does not move along different defocus positions, but the value of it decreases.

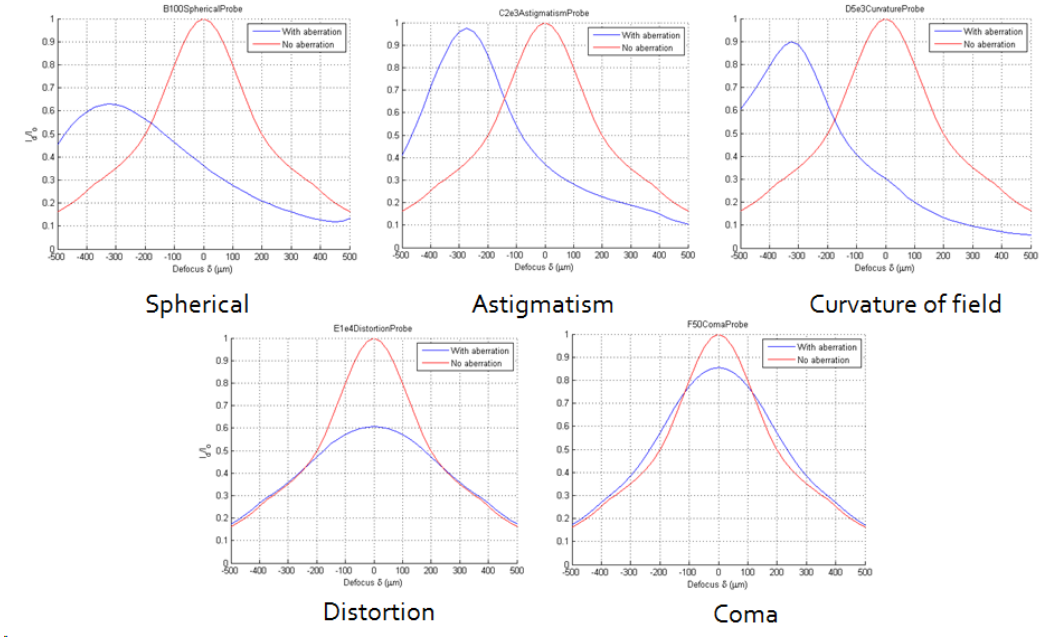

Figure 2-12: Diffraction efficiency at different longitudinal defocus for each type of aberration. Red curves are cases without aberration and blue curves are with aberration. The following values are used for the coefficient of each aberration: spherical aberration $B = 100$, astigmatism $C = 2 \times 10^3$, curvature of field $D = 5 \times 10^3$, distortion $E = 1 \times 10^4$, and comma $F = 50$.

Now we proceed to our VHF system. Again we assume that we are aiming at the detection of Iridium satellites. The parameters used are the same as those in Fig. 2-7. Two types of aberration are taken as examples here and the total system performance is plotted Fig. 2-13. It can be observed that the diffraction efficiency of the noise is mostly invariant with and without aberration; this matches our discussions above. And the signal efficiency, i.e. Iridium satellites at 780 km for this case, is lowered. Therefore, the overall SNR enhancement is reduced with the existence of aberration. Note that for positive aberration coefficient, the peak value is not at 780 km but near 230 km. This is because the phase profile of the aberration partially cancels out the phase introduced by the longitudinal defocus, as been illustrated in Fig. 2-12.

Overall, for our VHF system, aberration has a negative impact on the overall system performance. The amount of reduction relies on the amount of aberration

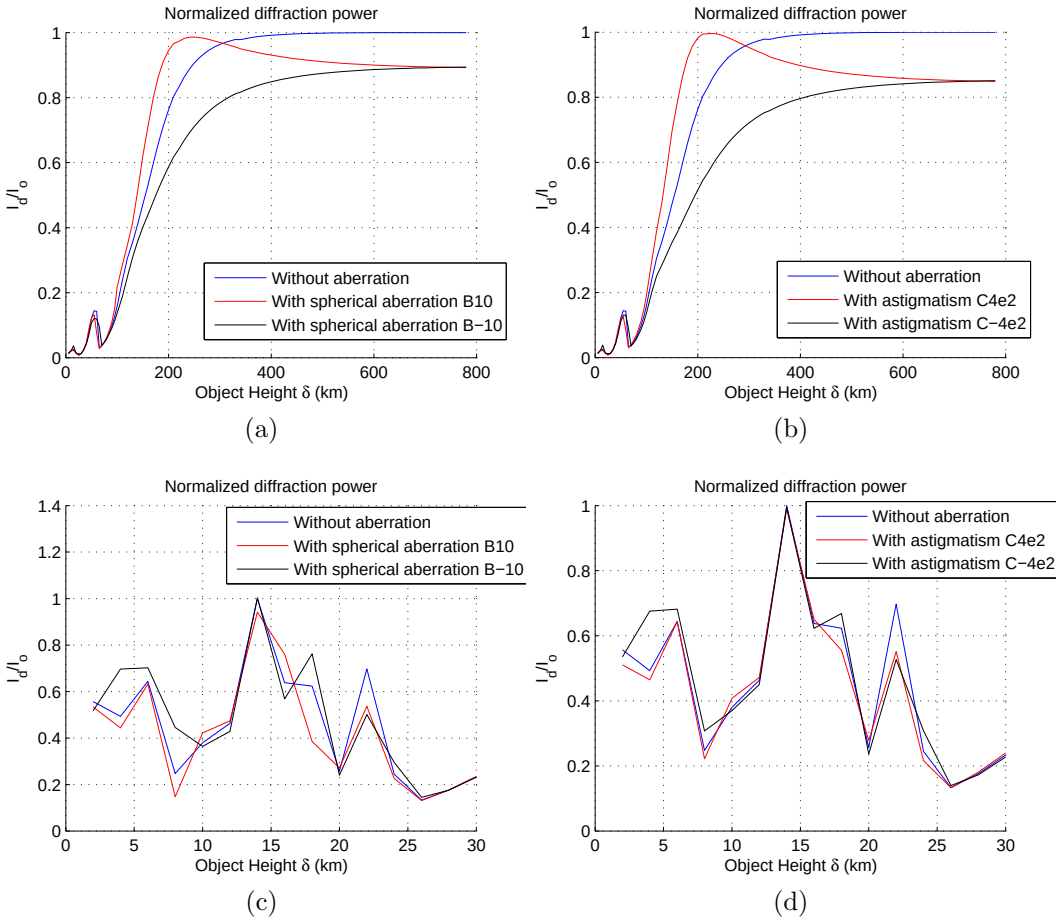

Figure 2-13: (Top) Diffraction efficiency of objects at various altitudes for our VHF system considering spherical aberration (left) and astigmatism (right). Blue curves are without aberration, red and black curves are with aberration of different signs. (Bottom) Zoomed–in view of top row for objects with height below 30 km. Spherical aberration coefficients are chosen as $B = 10$ and $B = -10$, and astigmatism coefficients are chosen as $C = 4 \times 10^2$ and $C = -4 \times 10^2$.

and its contribution to the signal's diffraction efficiency. Aberration has little effect on the diffraction efficiency of the daylight noise.

2.10 Atmospheric turbulence

Now we proceed to discuss a key factor in astronomy imaging–atmospheric turbulence, and how it affects the overall performance of our VHF system for the detection of artificial satellites. First, we need to model the atmospheric turbulence, which is in fact a stochastic process of phase shift (phase mask).

Optical beams wander randomly due to atmospheric turbulence, causing fluctuations in light intensity, resulting in a reduction of imaging quality. In principle, atmospheric turbulence can be modeled with a constantly changing phase mask. And like aberration, this phase change has some impact on the final system performance. According to [19], the phase of atmospheric turbulence can be written in terms of Zernike polynomials:

$$\phi(\rho,\theta) = \sum_{n=0}^{\infty}\sum_{m=0}^{n} A_{nm}\sqrt{2(n+1)}R_n^m(\rho)\cos(m\theta), \tag{2.12}$$

where $R_n^m(\rho)$ is radial polynomial and A_{nm} is certain coefficient. The polynomial coefficients are random numbers which follow a normal distribution governed by Kolmogorov model. Different choices of coefficients result into different phase profiles. An example is show in Fig. 2-14.

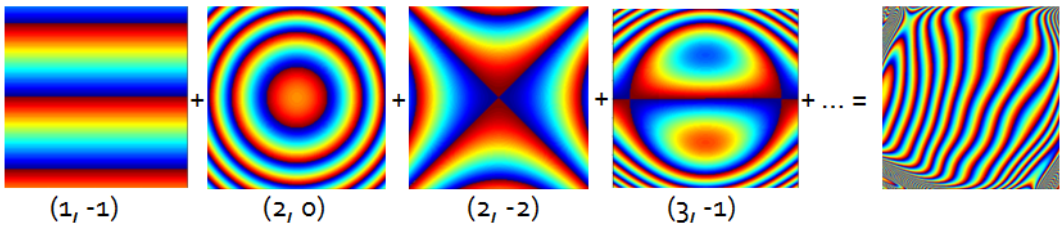

Figure 2-14: Typical Zernike polynomials. When they are weighted by certain coefficients for each polynomial term, their summation gives the phase profile of atmospheric turbulence.

One key parameter for modeling atmospheric turbulence is the turbulence co-

herence length r_0, or Fried's scale parameter. Physically, it represents the effective aperture diameter governed by the atmospheric turbulence. r_0 can be expressed as

$$r_0 = 1.68(C_n^2 L k)^{-3/5}, \tag{2.13}$$

where L is the path length through the atmosphere turbulence, C_n is atmospheric structure constant and k is wave vector. A physical imaging system has an aperture size, or diameter of aperture D, governed by the physical architecture of the system. In our system, the diameter of the aperture $D = 2$ mm, which is determined by the physical size of the second lens of the telephoto. Note that here we assume the lateral size of the volume hologram is larger than 2 mm. If not, the aperture size is governed by the size of the volume hologram. If the physical diameter of aperture D is smaller than the turbulence coherence length r_0, the system's resolution is determined by D; otherwise, the resolution is determined by r_0. By some calculation, the FWHM of long exposure averaging atmospheric point spread function (PSF), or "seeing", is

$$\text{FWHM} = \frac{0.98\lambda}{r_0}. \tag{2.14}$$

In radians (arc seconds), FWHM can be expressed as

$$\text{FWHM} = \frac{202140\lambda}{r_0}(\text{arc seconds}). \tag{2.15}$$

Normally, at high altitudes with clear sky, FWHM of seeing is on the order of 1 arc second, which corresponds to $r_0 = 0.1268$ m. This is much larger than our aperture diameter of $D = 2$ mm. Therefore, the resolution of our system is mainly determined by the diameter of aperture. To put it in another way, when $D/r_0 = 1$, FWHM of seeing is 63.5 arc seconds; this corresponds to a very large atmospheric turbulence for astronomy.

As examples, phase profiles and point spread functions (PSFs) at various astronomical seeings are plotted in Fig. 2-15 and Fig. 2-16. We notice that even when $D/r_0 = 1$, the PSF is still a good dot; and the PSF only spreads out and becomes

irregular when $D > r_0$. This again confirms that in normal seeing condition, atmospheric turbulence has negligible effect on the VHF system.

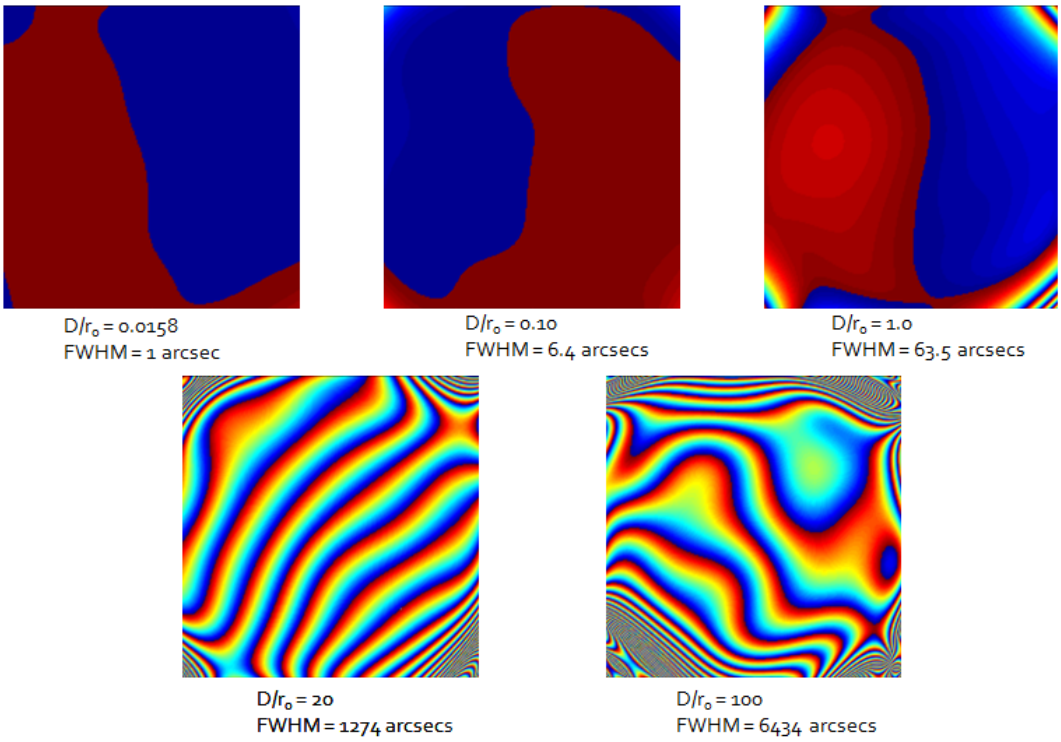

Figure 2-15: Examples of phase profiles for atmospheric turbulence at different values of FWHM of astronomical seeings.

We again incorporate the phase profile of atmospheric turbulence into our VHF system, and the diffraction efficiency for objects at different altitudes is plotted in Fig. 2-17. The parameters used for our VHF system are the same as those in Fig. 2-13. We notice that the diffraction efficiency of Iridium satellites keeps constant when $D/r_0 \leq 1$. The efficiency only decreases when the turbulence is very large. As for daylight scatterers, atmospheric turbulence has no significant influence, no matter how large the turbulence is. This makes sense and can be compared with the cases discussed in the above session regarding aberrations. For daylight scatterers, the Bragg mismatch is so large that adding additional phase change does not contribute. From all discussions above, we can conclude that in our current design, we do not need to consider the influence of atmospheric turbulence; however, if the physical aperture increases, turbulence should be taken into account.

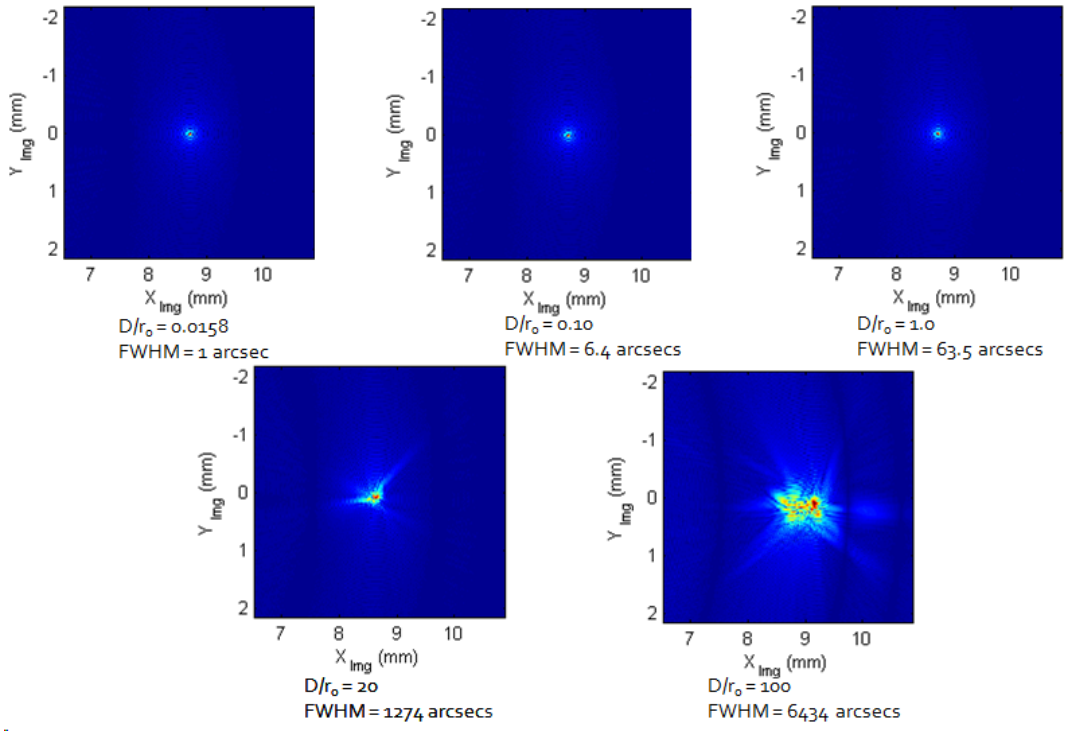

Figure 2-16: Examples of point spread functions at the detector when probed by signal beams without defocus, for atmospheric turbulence at different values of FWHM of astronomical seeings.

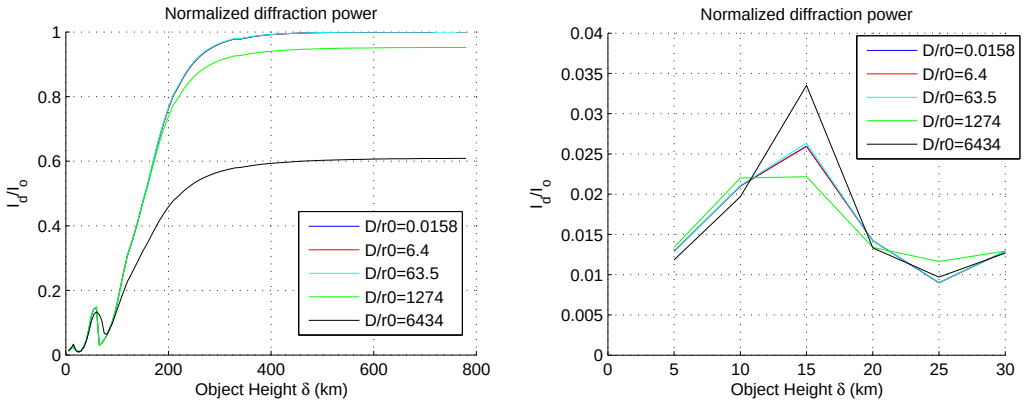

(a) (b)

Figure 2-17: Diffraction efficiency of objects at various altitudes for our VHF system considering atmospheric turbulence at different values of astronomical seeings. Left figure shows the entire range from 0 to 780 km, right figure is a zoomed–in at the altitudes of atmospheric scatterers from 0 to 30 km.

2.11 Experiment

To verify that our VHF system design is able to eliminate the daylight scattering and enhance the SNR in the detection of artificial satellites, we aim at designing a model system in the lab. Note that since our actual target (satellites) and scattering noises (atmosphere scatterers) are far away from the VHF, this system has to be "scaled down" in order to fit in the size limitation of our lab. In this way, a new design to mimic our previous design is necessary.

2.11.1 Experimental geometry

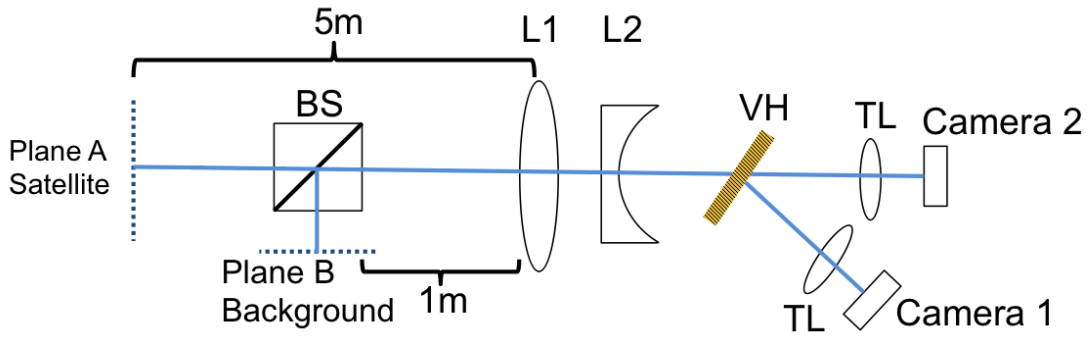

Figure 2-18: Scale down experimental geometry. BS: Beamsplitter, L1: Positive lens, L2: Negative lens, VH: volume hologram, TL: Tube lens.

A scale down design used for lab experiment is shown in Fig. 2-18. We use an object illuminated by either a laser (single wavelength) or an LED (broad band) to model the artificial satellite. The distance between the object and the first lens of our imaging system is 5 meters, reduced from hundreds of kilometers for a satellite, to fit in our lab; but 5 meters is still assumed to be a large enough distance for a good model. Besides, background source illuminates from 1 meter away and combines with the signal light using a beam splitter. Since the distance ratio between the object and scatterers has been decreased during the down scaling, the telephoto design can be loosened in order to use simple lab optical lenses. We have scaled the ratio of the focal lengths of the first and second lenses from the original 1000, which is impossible to achieve in the lab, to 10. Nevertheless, larger ratio is always desired. Therefore, we

chose the focal length of the second lens to be as small as possible, -25 mm. And the focal length of the first lens should be long enough, but still commercially available. We chose 250 mm. As for the aperture sizes of these two lenses, the first lens sets the limit. For a positive lens with focal length of 250 mm, commercially available diameters are mostly 2 inches, with a possibility to 3 inches. We chose 2 inches to be safe. The diameter of the second lens is not a problem as long as it is larger than 1/10 of 2 inches, i.e. 0.2 inches, which is easy to satisfy. The distance between two lenses is 238 mm.

The hologram we use here is made of PQ–PMMA, and pre–recorded by two plane waves at an angle of 34°. The imaging part after the telephoto is a standard VH imaging experimental geometry with a volume hologram, a tube lens, and a camera (Camera 1). In order to compare with the conventional imaging system case without the VHF, we integrated another optical path in this experimental geometry. When the hologram is removed, the undiffracted light enters directly through the tube lens into Camera 2. This part is our "control group".

2.11.2 Result: Case I

From now on, for easy discussion, we refer the optical source used to mimic the satellite as "satellite", and the one used to mimic atmospheric scatterers as "daylight".

In our first experimental case, we use both lasers as point sources for satellite and daylight, operating at wavelength $\lambda = 488$ nm. They are of equal output power. For the conventional system, we measured the power at the detector from each source independently; and this procedure is repeated for the VHF system. We then calculated the ratio of satellite power over daylight power for both systems. For conventional system, is ratio is merely 0.0836, because satellite is located 5 times further away then the daylight; given the same source power, light from satellite travels longer and spreads wider. However, for our VHF system, the power ratio is 139, significantly larger than 0.0836. It is clear that daylight has been attenuated to minimal value as a result of Bragg–mismatch.

2.11.3 Result: Case II

For the second experiment, we changed the daylight from a laser into a diffuser illuminated with an LED source (Thorlab LED4D201), which is broad band ranging from 430 nm to 650 nm. Under the illumination from both satellite and daylight, images were taken and shown in Fig. 2-19.

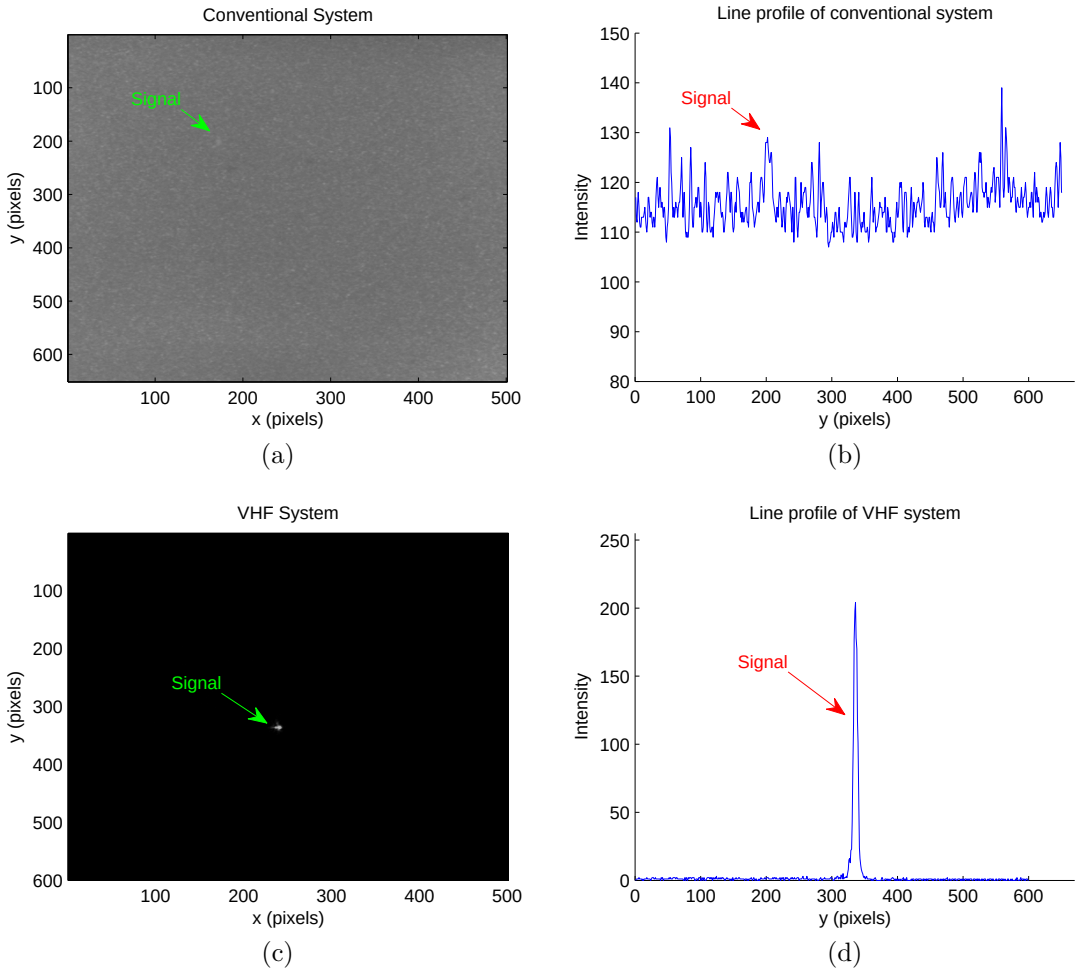

Figure 2-19: (Left) Images from the conventional system (top, Camera 1) and the VHF system (bottom, Camera 2), with illumination from both satellite (monochromatic) and daylight (broadband). (Right) Line profile across the signal spot for both images.

It is clearly observed that for conventional system, the daylight is so high that the signal has been washed out and buried. It is impossible to tell from Fig. 2-19(a) whether a signal exists or where it is. However, for our VHF system, daylight noises

have been significantly attenuated, leaving only the clear signal spot.

2.11.4 Result: Case III

In practice, both satellites and daylight are broadband. Therefore, in our third case, we used a USAF resolution target illuminated by a green LED (Thorlab LED4D201) as our satellite source, and a diffuser illuminated with a lamp as our daylight noise. We took images at the detector, and calculated the contrast ratio of targets of different feature sizes. Results are illustrated in Fig. 2-20. The added daylight deteriorates the imaging quality of the conventional system, making the patterns indecipherable. For our VHF system, the contrast ratio also decreases, but definitely less severely as the conventional system. It is clear from this experiment that the VHF system attenuates the daylight and enhances the overall SNR (see Fig. 2-20(c), where the rate of contrast decrease is plotted). This is also confirmed by camera images shown as examples in Fig. 2-20(d). The line width of the target pattern shown is 500 μm.

2.12 Conclusion

In this Chapter, we present volume hologram filter designs to mitigate the daytime sky background noise in artificial satellites' detection and imaging, by utilizing the longitudinal depth selectivity of volume holograms. We use a telephoto objective to enhance the working distance, adapting this system for observing objects at distances on the order of hundreds of kilometers. Key design parameters have been optimized, with larger daylight attenuation and wider spectral bandwidth. A scale down lab experiment is also implemented as a proof of this design.

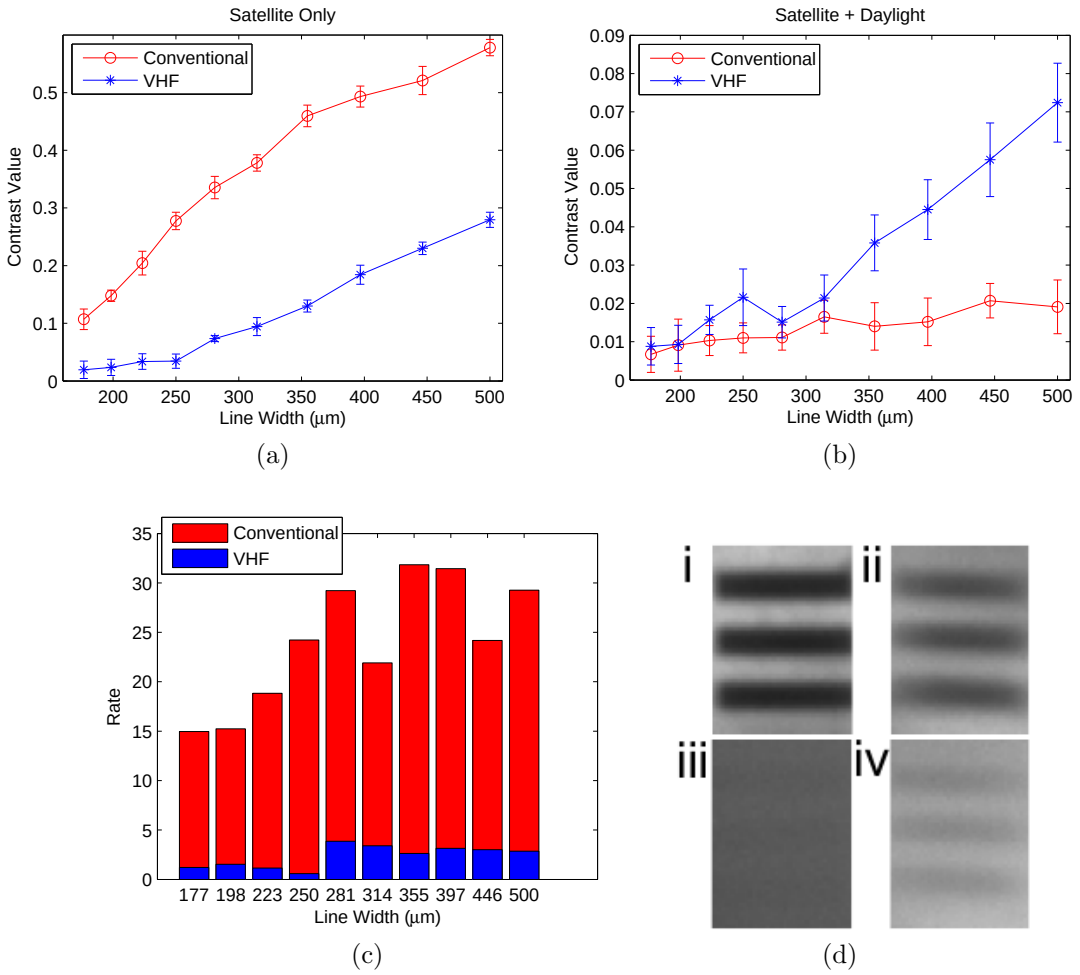

Figure 2-20: (a) Contrast ratio comparison of the conventional and VHF systems with only satellite. (b) Contrast ratio comparison of the conventional and VHF system with both satellite and daylight. (c) Rate of contrast decrease after introducing daylight. (d) Images at detectors for the conventional (i) and VHF (ii) system with only satellite, as well as the conventional (iii) and VHF (iv) system with both satellite and daylight.

Chapter 3

Design of volume holographic point spread functions using point deformations

Depth selectivity of 3D volume holographic pupils has been widely used in many applications. Besides this, volume holograms are also good candidates for implementing various point spread functions (PSFs) for different imaging purposes, due to their three–dimensional nature. The design of PSFs, often referred to as "PSF engineering" or pupil engineering, is one of the cornerstones of optical engineering. However, in most optical systems the pupil functions are limited in two dimensions; the designs are either deliberately shift–invariant or any desired shift invariance is limited by the available pupil functions. Volume holograms, on the other hand, are thick holograms where the thickness along optical axis is important and non–negligible. VHs are inherently strongly shift variant [8, 102, 129] and, thus, afford richer opportunities; we refer to it as "3D pupil engineering" because of the volumetric nature of the holographic pupils.

However, for most volume holograms, their structure, i.e. refractive index distribution, is still quite regular and its 3D nature is not well exploited. In this chapter, we discuss the particular case of adding one more degree of freedom in 3D pupil engineering by mechanically deforming a volume holographic pupil. This can be accomplished,

for example, by a superposition of point indenters at the hologram exterior. Simple forward analysis of such a problem has been discussed for the first time in [134] as a means to characterize the 3D deformation in the optical material's interior as result of the indentation. Here, we first extend this forward problem with multiple point indenters [44]; this offers more flexibility to the design of PSFs. Then we focus on the "inverse problem", where multiple point deformations, or even continuous forces are designed to achieve the desired shift–variant PSF [46].

3.1 From single to multiple point deformations

A single point load on one side of the hologram is able to change the resulting PSF. This has been discussed in [134] using a perturbation approach. Here we start from this single indenter case and propose a general approach to analyze this system and calculate the PSF given a combination of point indenters. This is the "forward problem".

Without loss of generality, we choose a Fourier geometry volume holographic imaging (VHI) setup shown in Fig. 3-1(a). The volume hologram is recorded by two plane waves (signal and reference beams), resulting in a dielectric modulation of $\Delta\epsilon(\mathbf{r}) = \epsilon_1 \exp(i\mathbf{K}_g \cdot \mathbf{r})$, where ϵ_1 is the amplitude of the spatial modulation, and $\mathbf{K}_g = \mathbf{k}_s - \mathbf{k}_f$ is the Bragg wave vector of the grating. The hologram is then illuminated by a probe beam $E_p(\mathbf{r})$. The diffracted field at the detector plane becomes [134]

$$\begin{aligned} E_d(\mathbf{r}'') &= \iiint E_p(\mathbf{r})\Delta\epsilon(\mathbf{r})V(\mathbf{r}) \exp\left(-i\frac{2\pi}{\lambda}\frac{xx''+yy''}{f}\right) \\ &\quad \cdot \exp\left[-i\frac{2\pi}{\lambda}\left(1-\frac{x''^2+y''^2}{2f^2}\right)z\right] d^3\mathbf{r}, \end{aligned} \tag{3.1}$$

where $V(\mathbf{r})$ is the hologram shape function which has value 1 inside the lens and 0 outside, and f is the focal length of the Fourier lens. For coordinate systems, we use x, y, and z to denote the axes at the hologram, and x'', y'', and z'' to denote the axes at the detector. Eq. 3.1 is the 3D Fourier transform of $E_p(\mathbf{r})\Delta\epsilon(\mathbf{r})V(\mathbf{r})$ at spatial

frequency

$$\frac{x''}{\lambda f}, \frac{y''}{\lambda f}, \frac{1}{\lambda}\left[1 - \frac{x''^2 + y''^2}{2f^2}\right]. \tag{3.2}$$

From Eq. 3.1 it is obvious that this imaging system is not shift–invariant. This property provides an extra way of controlling the impulse response [124]. However, this 3D VHI system does not provide fully three degrees of design freedom because the PSF is a 2D manifold in the 3D Fourier space of the volume hologram [6].

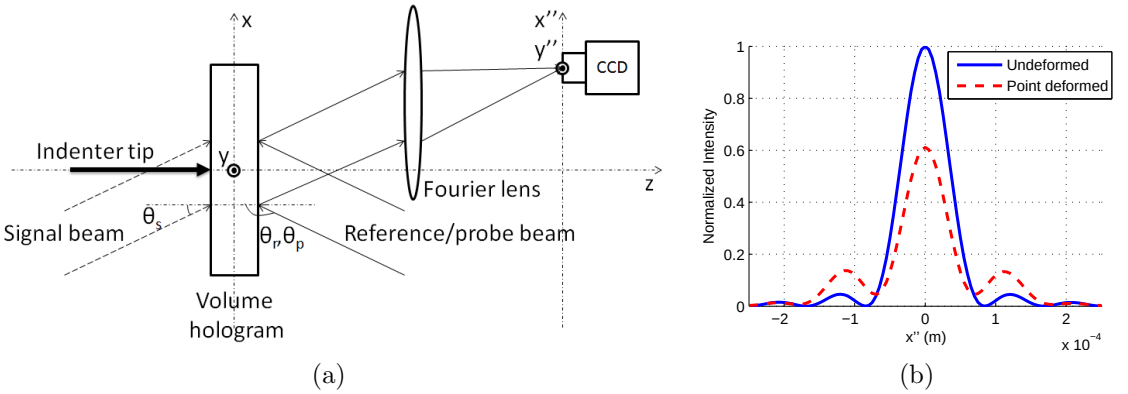

(a) (b)

Figure 3-1: (a) Fourier geometry of reflection volume hologram. (b) PSF of geometry (a) with and without the point load.

It has been demonstrated [134] that a single point indenter, as a perturbation, can change the spatial material distribution $\Delta\epsilon(\mathbf{r})$. When a point load of force F is exerted along the z direction vertically to the hologram surface, the elastic displacement inside the volume hologram is given by [79]

$$u_x = \frac{F}{4\pi G}\left[\frac{xz}{\rho^3} - (1-2\nu)\frac{x}{\rho(\rho+z)}\right], \tag{3.3}$$

$$u_y = \frac{F}{4\pi G}\left[\frac{yz}{\rho^3} - (1-2\nu)\frac{y}{\rho(\rho+z)}\right], \tag{3.4}$$

$$u_z = \frac{F}{4\pi G}\left[\frac{z^2}{\rho^3} + \frac{2(1-\nu)}{\rho}\right], \tag{3.5}$$

where $\rho = \sqrt{x^2+y^2+z^2}$ is the distance to the loading position, G is the shear modulus and ν is the Poisson ratio. From the equation above it can be seen that instead of a constant $\mathbf{K}_g$ throughout the hologram, the grating wave vector now

becomes a function of position in the volume hologram axis $\mathbf{K}_g = \mathbf{K}_g(\mathbf{r})$, modifying the PSF at the image plane. The position dependence of grating wave vector offers rich opportunities to achieve a wealth of different PSFs.

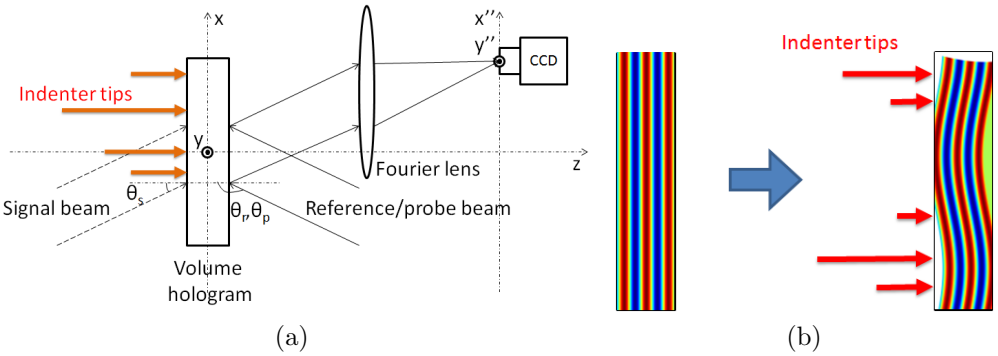

Figure 3-2: (a) Imaging system geometry utilizing a reflection volume hologram. (b) Illustration of VH deformations with multiple point indenters.

Generalizing from the single point load case, it is straightforward to use multiple point indenters at different positions, each exerting a different force, to obtain more variety on $\mathbf{K}_g(\mathbf{r})$. Fig. 3-2 shows how these point indenters are exerted on the hologram and how this hologram is deformed accordingly. If one indenter tip is mounted at position x_i, the correspondent material displacement is $\mathbf{u}_i[\delta(x - x_i), F_i]$, where $\mathbf{u}$ is the elastic shift $\{u_x, u_y, u_z\}$ specified in Eq. 3.5, F is the force, and δ denotes the point indenter. For N such point loads at different positions, the total displacement can be written as

$$\sum_{i=1}^{N} \mathbf{u}_i[\delta(x - x_i), F_i]. \tag{3.6}$$

Here we assume that every point deformation is small enough that it can be thought as an independent perturbation and the superposition principle applies. Therefore, the relationship between point deformations and the resulting PSF becomes

$$\begin{aligned} E_d(\mathbf{r}'') \;=\; & \iiint E_p(\mathbf{r})\Delta\epsilon\left(\mathbf{r} - \sum_{i=1}^{N} \mathbf{u}_i[\delta(x - x_i), F_i]\right) V(\mathbf{r}) \\ & \cdot \exp\left(-i\frac{2\pi}{\lambda}\frac{xx'' + yy''}{f}\right) \exp\left[-i\frac{2\pi}{\lambda}\left(1 - \frac{x''^2 + y''^2}{2f^2}\right) z\right] d^3\mathbf{r}. \end{aligned} \tag{3.7}$$

The advantage of using multiple point indenters is that now the pattern (or dielectric distribution) of the volume hologram can be much more irregular than the undeformed case, providing more flexibility for designing PSFs. More specifically, we now have three design freedoms: number of point indenters N, force of each indenter F_i, and the position of each indenter x_i. For a specific desired PSF, the expression above allows us to determine the corresponding N, F_i, and x_i. This can be done, for example, by decomposing the desired PSF into fundamental modes, each created by a single point indenter. It is also beneficial to first create a PSF look–up table for all the possible single point indenter, i.e. F_i and x_i, then determine which ones to select in order to create a certain PSF. In this way we are also able to judge whether a certain PSF is achievable or not by multiple point deformations. An optimization method for this "inverse problem" will be discussed later.

3.2 Continuous force

The way we analyze multiple point deformations also potentially applies to continuous forces exerted on the hologram. A continuous force $F(x)$ can be approximated in terms of multiple point indenters as $F(x) = \sum_{i=1}^{N} F(x_i)\delta(x - x_i)$, provided that these discrete loads are close enough to each other. As illustrated in Fig. 3-3, for close–enough point loads (blue spikes), they could be approximated by a continuous force (red curve). Alternatively, a continuous force can be mimicked by discrete point loads as well. Therefore we are able to analyze or determine continuous forces with the same procedure.

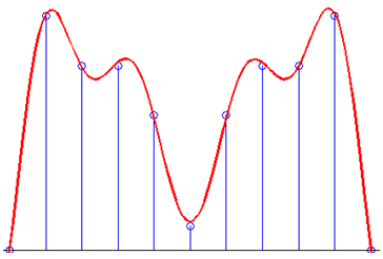

Figure 3-3: Approximation of a continuous force using discrete point indenters, or vice versa.

3.3 Multiple point deformations: examples

To illustrate this forward analysis problem, we designed several PSFs using multiple point indenters. Our setup is the same as Fig. 3-1(a). This is a reflective volume hologram Fourier geometry with indenter tips at the left surface of the hologram. We choose a rectangular volume hologram of size 6.0mm $\times$ 6.0mm $\times$ 1.5mm, recorded by two plane waves with angles $\theta_s = 8^\circ$ and $\theta_f = 172^\circ$ for signal and reference beams, respectively. The free space wavelength is 632 nm. Shear modulus and Poisson ratio are chosen as $G = 44$ GPa and $\nu = 0.22$ which are for the Ondax material as used in [134].

Fig. 3-4 illustrates three designed VHI PSFs: (a) a single peak, shifted with respect to the undeformed position; (b) a double peak response; (c) a five peak response. The determined point loads exerted on the volume hologram to realize these PSFs are also shown. It is observed that different PSFs are related to different grating wave vector $\mathbf{K}_g(\mathbf{r})$ distributions and different amounts of shift variance, while combinations of point loads result into the desired $\mathbf{K}_g(\mathbf{r})$. For example, two asymmetric point loads in Fig. 3-4(d) create a tilted fringe pattern which changes the undeformed $\mathbf{K}_g$ into a tilted $\mathbf{K}'_g$. As a result, the main lobe is shifted to a new Bragg matched position in the detector plane. The third row of Fig. 3-4 illustrates the angle detuning Bragg mismatched PSFs. It can be clearly seen that for different probe beam angles (horizontal axis), the PSFs (vertical slices) are different. This confirms that VHI system is indeed shift–variant. Note that Fig. 3-4(f) contains equally– and closely–spaced point indenters, which can also be approximated as a continuous point load $F(x)$.

3.4 Inverse problem: optimization

Above we discussed the "forward problem", i.e. given the combination of point indenters, how to analyze and calculate the resulting PSF. In this section we aim to find a combination of point deformations or continuous force which result into a de-

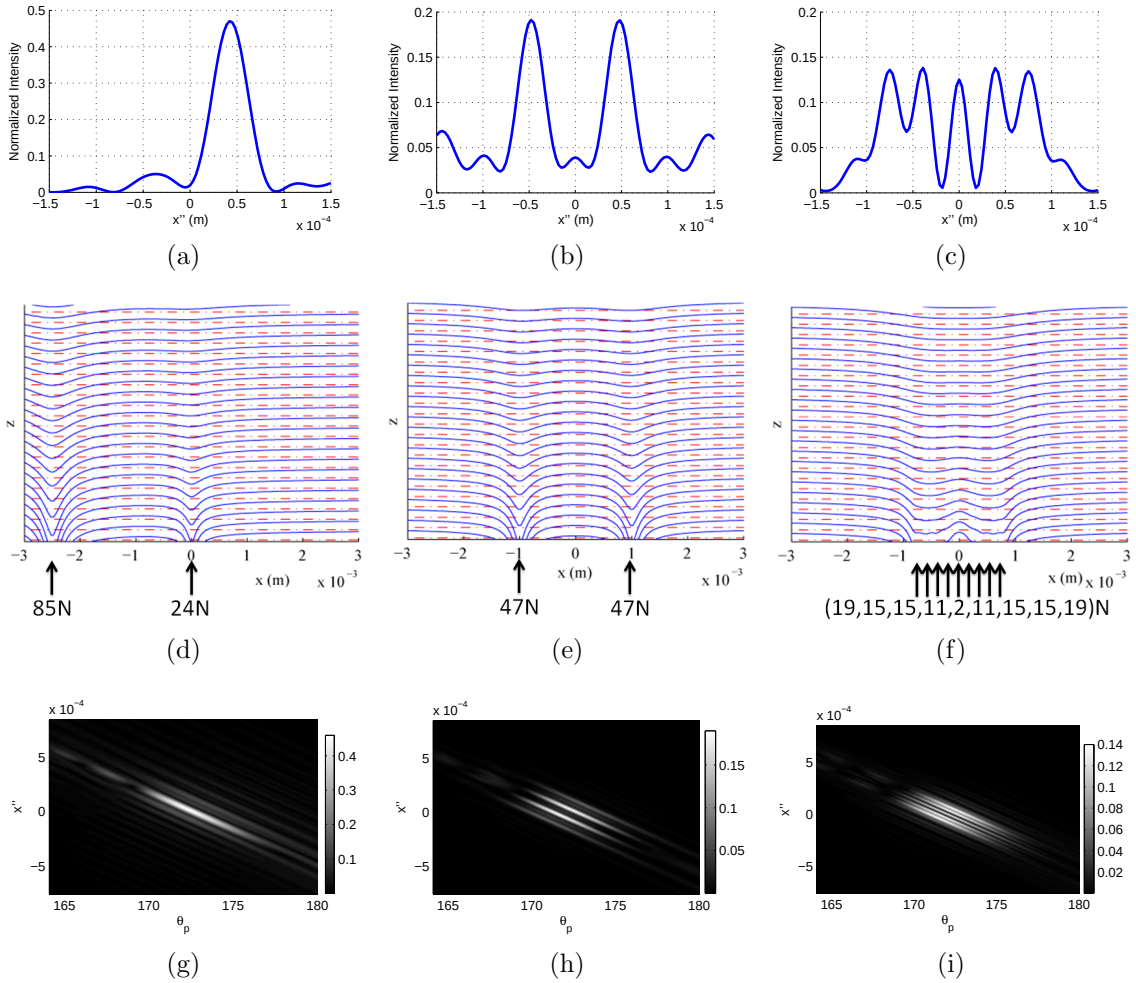

Figure 3-4: (a)(b)(c) Three different kinds of desired PSFs normalized to the peak intensity of the PSF without deformation at Bragg matched probe beam $\theta_p = 172°$. (d)(e)(f) Combination of point loads to achieve the above PSFs, and the corresponding fringe patterns. Red dashed lines and blue solid lines denote the pattern before and after the deformation, respectively. (g)(h)(i) Angle detuning Bragg mismatched PSFs. The brightness plotted is the normalized intensity.

sired PSF. More generally, for a forward problem, we are given the illumination on a certain optical system and are required to calculate the output of the system. For an inverse problem, the illumination and the output field or intensity are provided and we are required to design the optical system. With respect to optical imaging, the design of PSFs requires the design of an optical system (here it is a combination of point indenters to deform the volume holographic pupil) given a point source as input and a desired output.

We use the same Fourier geometry volume holographic imaging setup as illustrated in Fig. 3-1(a). The diffracted field at the detector has been expressed in Eq. 3.7. It is not straight–forward to solve for F_i to realize the desired PSF. Here we propose to use nonlinear least squares method to locate the best point indenter combination, by minimizing the error between our desired PSF and the PSF achieved by F_i, i.e.

$$\left| |E_{\text{desired}}(\mathbf{r}'')|^2 - |E_d(\mathbf{r}'')|^2 \right|. \tag{3.8}$$

If we only consider a two–dimensional system along x–z plane, the error function to minimize can be expressed as:

$$\sum_{j=1}^{M} \left| |E_{\text{desired}}(x_j'')|^2 - |E_d(x_j'')|^2 \right|. \tag{3.9}$$

where the CCD plane has been discretized into M points: x_j''. This problem can be easily generalized to three–dimensional.

Note that the method of nonlinear least squares only finds local minima and is very sensitive to the initial condition. Certain global search methods can be used to find a global minimum. In order to quickly find the desired solution, we could utilize the PSF look–up table for different single point indenters, i.e. F_i and $\delta(x - x_i)$, mentioned in Section 3.1, to first roughly select a reasonable initial combination of indenters. Nonlinear least squares can then be applied to realize the PSF in need.

3.5 Inverse problem: examples

In this section we discuss some optimization examples for the design of various PSFs. Without loss of generality, the same set of system parameters as the one in Section 3.3, including hologram size and material, is considered here.

Fig. 3-5 illustrates the optimized design to achieve a shifted PSF. This example should be compared with the case of first column of Fig. 3-4. A similar set of forces has been calculated.

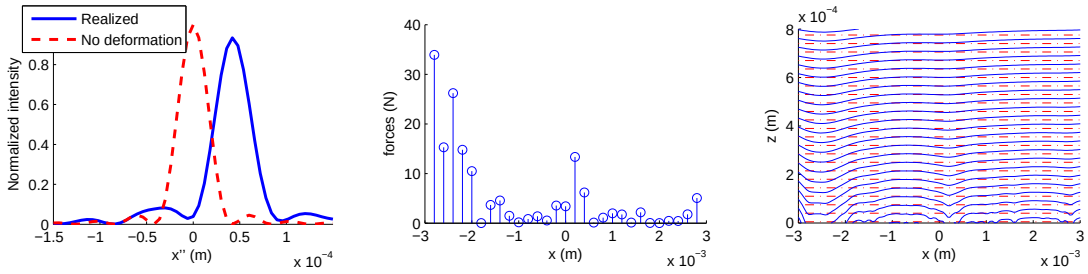

Figure 3-5: (Left) Designed PSFs, (middle) combinations of point loads, and (right) the corresponding fringe patterns for a shifted PSF. For fringe pattern plots, red dashed lines and blue solid lines denote the pattern before and after the deformation, respectively.

Fig. 3-6 demonstrates the optimized results for realizing "box"–shaped PSFs with different widths. We notice that "Gibbs phenomenon" appears in the optimized rectangular PSFs, because a perfect "box" PSF is not achievable. Starting from different initial guesses, different PSFs can be realized (see the top two rows of Fig. 3-6). The target PSF–the red dashed "box"–is the same but the optimized results are quite different. The top result has more oscillations in the passband, but has a narrower "roll–off" zone; on the contrary, the middle result has almost flat passband but definitely a wider "roll–off". This shows that there is always a balance between these two factors. The choice of which depends on the the requirements of certain optical systems.

Fig. 3-7 shows two optimized results for realizing narrower mainlobe and suppressed sidelobes, respectively. From the first row, narrowing the mainlobe boosts up the sidelobes; and from the second row, the suppression of sidelobes has to widen the mainlobe. This is another trade–off: between mainlobe width and sidelobe strengths.

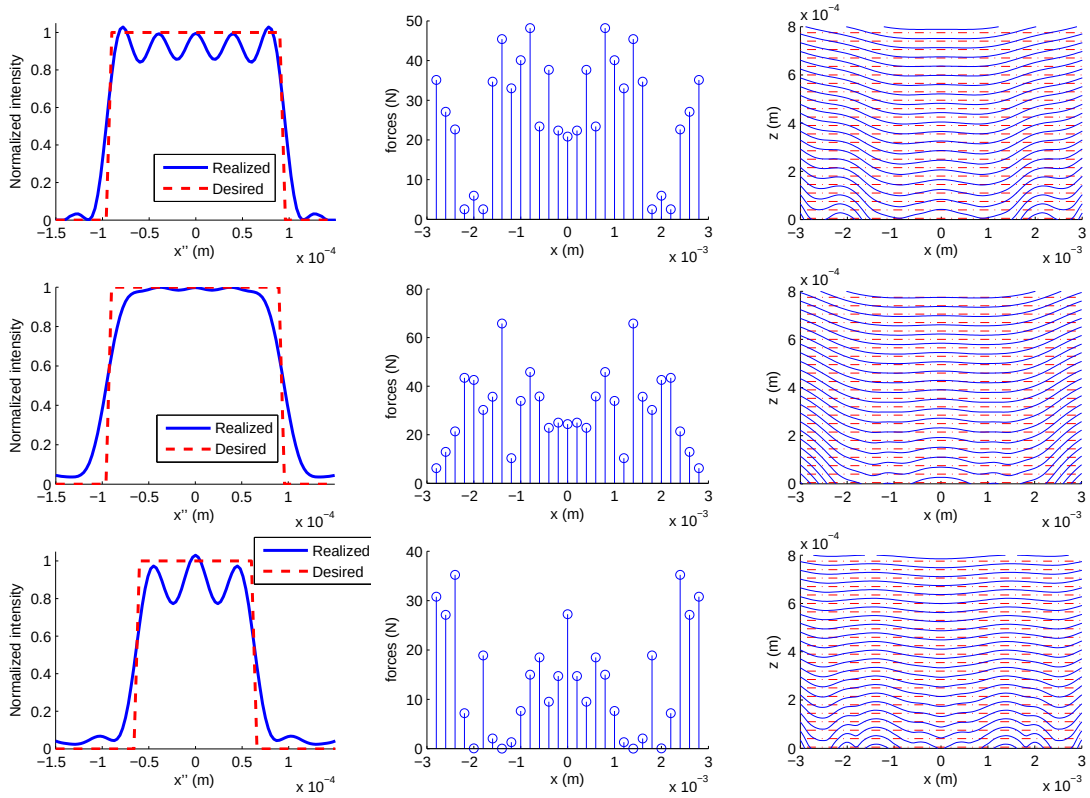

Figure 3-6: (Left) Designed PSFs, (middle) combinations of point loads, and (right) the corresponding fringe patterns for: (from top to bottom) wide rectangular PSF (Case I), wide rectangular PSF (Case II), narrow rectangular PSF. For fringe pattern plots, red dashed lines and blue solid lines denote the pattern before and after the deformation, respectively.

Suppression of both of them is not possible, and the choice of which depends on the system requirements. These PSFs can be potentially applied to various imaging applications which require, for example, super–resolution or reduced crosstalk. Note that these closely–spaced point indenters can also be approximated as a continuous point load $F(x)$.

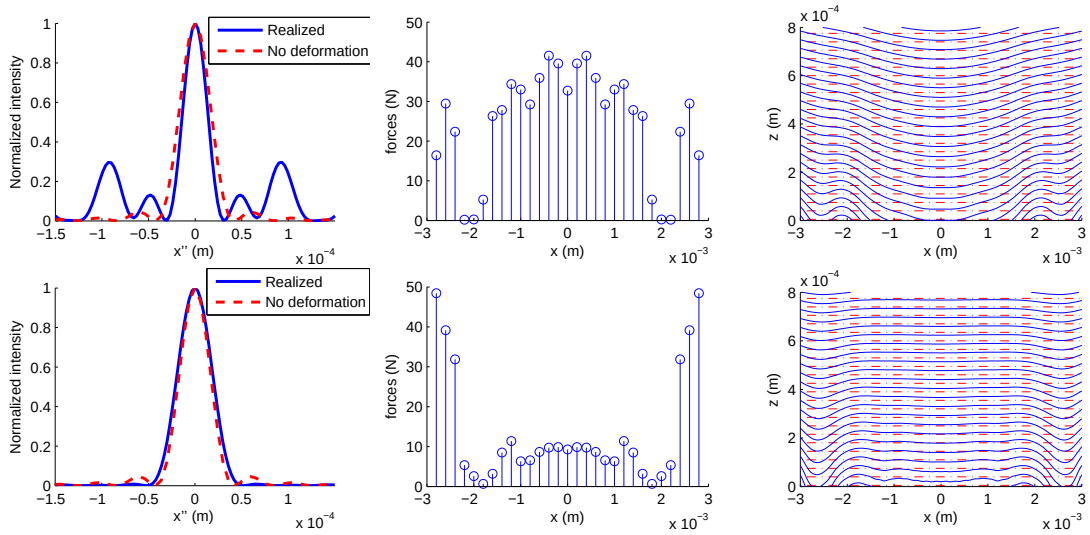

Figure 3-7: (Left) Designed PSFs, (middle) combinations of point loads, and (right) the corresponding fringe patterns for (top) PSF with narrowed main lobe, and (bottom) PSF with suppressed side lobes. For fringe pattern plots, red dashed lines and blue solid lines denote the pattern before and after the deformation, respectively.

3.6 Conclusion

We have demonstrated how to design VHI PSFs using multiple point indenters. Both forward and inverse problems have been explored. The best combination of point indenters could be located using optimization. It should be noted that not all PSFs are achievable by multiple point deformations. Nevertheless, there are also more mechanical deformations besides point load. A more general and sophisticated VHI inverse problem might involve a combination of multiple point deformations, linear deformations, shearing, bending, twisting, etc. These bulk transformations will be discussed in the following chapter.

THIS PAGE INTENTIONALLY LEFT BLANK

Chapter 4

Transformational volume holography

In the previous chapter we have investigated the exterior deformations of the VH pupils using a superposition of point indenters. However, not all PSFs are achievable by multiple point indenters. Here we propose bulk mechanical deformations besides point load, including compression, shearing, bending, twisting, etc. These deformations offer more general and sophisticated PSF designs for various microscopic imaging applications. Through transformation, the system performance can be tuned to fit more design criteria such as spectral composition of the PSF, anisotropic behavior, etc. This general approach is called transformational volume holography. It allows for *in vivo* adjustment of an optical system, e.g. a microscope, for different imaging purposes. One can simply change the mechanical deformations applied on the VHs to achieve various PSFs, without having to replace the pupils.

Numerically, it is straightforward to compute the final PSF given a certain type of transformation. However, these computations require 3D integrations; and normally the corresponding integrands are highly oscillatory and, hence, excessive sampling is required, especially in 3D. This poses unattainable demands on extensive CPU and memory cost. Furthermore, a physically intuitive relationship between the transformation of the VH pupils and the resulting PSFs is lost. In this chapter, we focus on finding quasi–analytical expressions for calculating the PSFs, since analytical equa-

tions are always much easier to compute, and give better physical intuitions.

4.1 Volume holographic imaging systems

In this chapter, without loss of generality, we use a transmissive geometry of volume holographic imaging system discussed in Chapter 1. The hologram is recorded by two plane waves at opposite angles. After recording, it is probed by another plane wave which is exactly the same as the reference beam used for recording. In this case the hologram is perfectly Bragg–matched and the final optical field collected by the detector can be calculated as (see also Eq. 1.7)

$$\begin{aligned} q(x') &= \iint E_p(x'',z'')\epsilon(x'',z'')s(x'',z'')\exp\left(-i2\pi\frac{x'x''}{\lambda f_2}\right) \\ &\quad \cdot\exp\left[-i2\pi\left(1-\frac{x'^2}{2f_2^2}\right)\frac{z''}{\lambda}\right]\mathrm{d}x''\mathrm{d}z''. \end{aligned} \tag{4.1}$$

We are able to analytically perform the integral and the final result is

$$q(x') = L_x\cdot L\cdot\mathrm{sinc}\left[\frac{L_x}{\lambda}\left(\frac{x_s}{f_1}+\frac{x'}{f_2}\right)\right]\mathrm{sinc}\left[\frac{L}{2\lambda}\left(\frac{x_s^2}{f_1^2}-\frac{x'^2}{f_2^2}\right)\right]. \tag{4.2}$$

It is composed of two "sinc" terms. Physically, the first sinc term corresponds to the finite lateral aperture of the hologram, and the second sinc term is a result of the non–negligible thickness of the hologram. The second term only appears when the pupil's thickness should be considered.

More generally, Eq. 4.1 can be written as

$$q(x',y') = \iiint E_p(\mathbf{x}'')\epsilon(\mathbf{x}'')s(\mathbf{x}'')\exp\left[-i2\pi\left(\frac{x'}{f_2},\frac{y'}{f_2},1-\frac{x'^2+y'^2}{2f_2^2}\right)\cdot\mathbf{x}''\right]\mathrm{d}\mathbf{x}'', \tag{4.3}$$

where we denote (x'',y'',z'') as a vector $\mathbf{x}''$, including the previously neglected y component. It is actually a 3D Fourier transform [8].

4.2 Transformation analysis

Bulk mechanical deformations apply transformations on the VH, and the coordinates are changed accordingly [86, 108]. Originally the coordinates centered at the hologram are (x'', y'', z''). After the deformations, the axes become

$$\begin{aligned} x''_{(2)} &= f_{x''_{(2)}}(x'', y'', z''), \\ y''_{(2)} &= f_{y''_{(2)}}(x'', y'', z''), \\ z''_{(2)} &= f_{z''_{(2)}}(x'', y'', z''). \end{aligned} \tag{4.4}$$

This corresponds to a transformation matrix of

$$\mathbf{T} = \begin{pmatrix} \frac{\partial f_{x_{(2)}}}{\partial x} & \frac{\partial f_{x_{(2)}}}{\partial y} & \frac{\partial f_{x_{(2)}}}{\partial z} \\ \frac{\partial f_{y_{(2)}}}{\partial x} & \frac{\partial f_{y_{(2)}}}{\partial y} & \frac{\partial f_{y_{(2)}}}{\partial z} \\ \frac{\partial f_{z_{(2)}}}{\partial x} & \frac{\partial f_{z_{(2)}}}{\partial y} & \frac{\partial f_{z_{(2)}}}{\partial z} \end{pmatrix}. \tag{4.5}$$

There are two approaches to include this coordinate transformation in the VH analysis. The first method, as shown in Fig. 4-1(a), uses the coordinates after the transformation for integration. That is to say, the coordinates used for probe beam and the Fourier transform should be transformed. In addition, the area (or volume) of each integration grid changes (see Fig. 4-1(a)). Therefore, as a compensation, the Jacobian of the transformation matrix should be applied on $\mathrm{d}\mathbf{x}''$, since mathematically, the Jacobian denotes the scaling of grid area (or volume). Using $\mathbf{x}''_{(\mathbf{2})} = \mathbf{T} \cdot \mathrm{x}''$, this approach yields

$$\begin{aligned} q(x', y') &= \iiint E_p(\mathbf{T} \cdot \mathrm{x}'')\epsilon(\mathbf{x}'')s(\mathbf{x}'') \\ &\quad \cdot \exp\left[-i2\pi \left(\frac{x'}{f_2}, \frac{y'}{f_2}, 1 - \frac{x'^2 + y'^2}{2f_2^2} \right) \cdot (\mathbf{T} \cdot \mathrm{x}'') \right] |\mathbf{T}| \mathrm{d}\mathbf{x}''. \end{aligned} \tag{4.6}$$

The second method is the opposite of the first one. It utilizes the same coordinates without transformation for integration (see Fig. 4-1(b)). The coordinates of permittivity distributions and hologram shape functions should be mapped back to the

original coordinates (x'', y'', z'') through

$$\begin{aligned} x'' &= f_{x''}^{-1}(x''_{(2)}, y''_{(2)}, z''_{(2)}), \\ y'' &= f_{y''}^{-1}(x''_{(2)}, y''_{(2)}, z''_{(2)}), \\ z'' &= f_{z''}^{-1}(x''_{(2)}, y''_{(2)}, z''_{(2)}). \end{aligned} \tag{4.7}$$

And due to the change of hologram shape function, the integration boundaries should be modified accordingly. In total, the integral now becomes

$$\begin{aligned} q(x', y') = & \int_{x''_{(2)}} \int_{y''_{(2)}} \int_{z''_{(2)}} E_p(\mathbf{x''_{(2)}}) \epsilon(\mathbf{x''}) s(\mathbf{x''}) \\ & \cdot \exp\left[-i2\pi \left(\frac{x'}{f_2}, \frac{y'}{f_2}, 1 - \frac{x'^2 + y'^2}{2f_2^2} \right) \cdot (\mathbf{x''_{(2)}}) \right] \mathrm{d}\mathbf{x''_{(2)}}. \end{aligned} \tag{4.8}$$

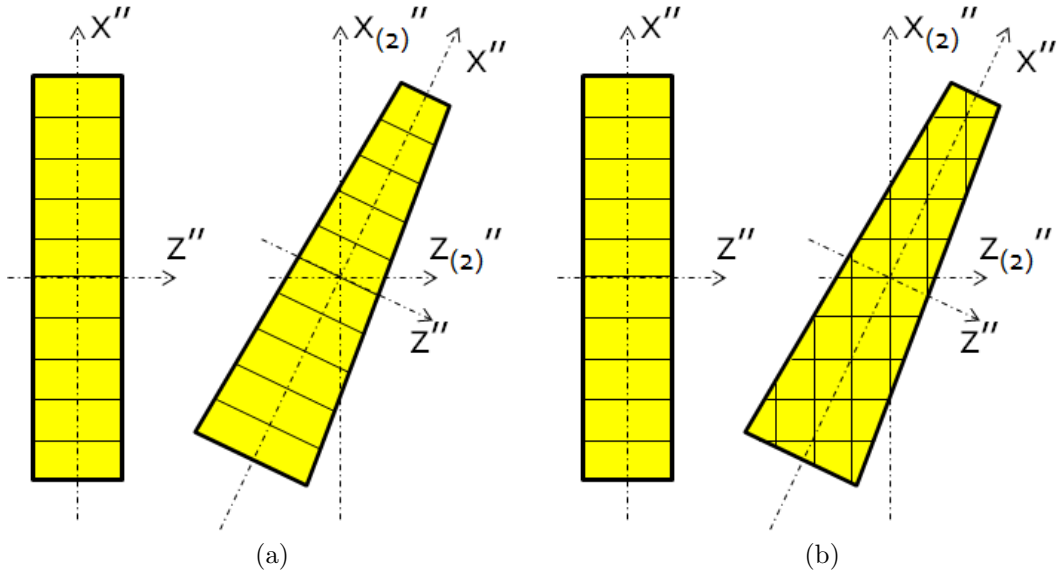

(a) (b)

Figure 4-1: Two analysis approaches for including bulk transformations in volume holographic imaging systems. For each case, left and right figures show coordinates used for calculating the integrals without and with the transformation, respectively.

Numerically these two methods do not make much difference. However, since in this chapter we aim at locating analytical solutions, we prefer the first approach because the complication of integral limits in the second method makes it a difficult

job to find an analytical solution.

Note that we assume all transformations are small enough so that only material (permittivity or refractive index) re–distribution is considered. For large transformations, anisotropy [108] becomes non–negligible and should be included. However, in transformational volume holography, small transformation assumption suffices because most large transformations result into significant Bragg–mismatch with the incoming probe beam so that the diffracted field becomes minimal; this is not suitable for imaging applications.

4.3 Affine transformations

We first discuss some common affine transformations where exact analytical solutions are possible. Note that in this section, all transformations, as well as the VH itself, are assumed to be invariant along y'' axis thus we only calculate along x''–z'' plane. Without loss of generality, for all the examples and discussions below, the following parameters are used for the volume holographic imaging system: wavelength $\lambda = 632$ nm, angle of signal beam $\theta_s = -8^{\circ}$, angle of reference beam $\theta_f = 8^{\circ}$ and size of hologram $L_x = 3$ mm, $L = 0.3$ mm.

4.3.1 Hologram shrinkage

First we consider uniform hologram shrinkage [9, 43, 70, 139], and assume that the shrinkage occurs only along z'' axis (see Fig. 4-2(a)). The transformation can be expressed as

$$\begin{aligned} x''_{(2)} &= x'', \\ z''_{(2)} &= (1-\delta)z'', \end{aligned} \tag{4.9}$$

where δ is the compression ratio. The corresponding transformation matrix is

$$\mathbf{T} = \begin{pmatrix} 1 & 0 \\ 0 & 1-\delta \end{pmatrix}, \tag{4.10}$$

with $|\mathbf{T}| = 1 - \delta$. Substitute Eq. 4.10 into Eq. 4.6 and we can derive an analytical equation for the final field to be

$$q(x') = L_x \cdot (1-\delta)L \cdot \mathrm{sinc}\left[\frac{L_x}{\lambda}\left(\frac{x_s}{f_1} + \frac{x'}{f_2}\right)\right]\mathrm{sinc}\left[\frac{L}{2\lambda}\left(\frac{x_s^2}{f_1^2} - \frac{x'^2}{f_2^2}\right)\right]. \tag{4.11}$$

This result matches with the results presented in [134] using a perturbation theory approach. Note that interestingly the resulting PSF is simply a reduction of intensity comparing with the undeformed case. This makes sense since shrinkage along z'' does not change the grating vector of the hologram, which is along x'' direction. The hologram is still perfectly Bragg–matched. The lowered intensity is due to the reduced hologram area as a result of shrinkage. An example of final PSF is demonstrated in Fig. 4-2(b), which is a scaled sinc function. Note that we are plotting the intensity, which is proportional to $|q(x')|^2$.

We then consider hologram shrinkage only along x'' axis (see Fig. 4-2(c)). Similar to the previous case, now the transformation matrix becomes

$$\mathbf{T} = \begin{pmatrix} 1-\delta & 0 \\ 0 & 1 \end{pmatrix}, \tag{4.12}$$

with $|\mathbf{T}| = 1 - \delta$. The final analytical equation of the output field is

$$q(x') = (1-\delta)L_x \cdot L \cdot \mathrm{sinc}\left[\frac{L_x}{\lambda}\left(\frac{(1+\delta)x_s}{f_1} + \frac{(1-\delta)x'}{f_2}\right)\right]\mathrm{sinc}\left[\frac{L}{2\lambda}\left(\frac{x_s^2}{f_1^2} - \frac{x'^2}{f_2^2}\right)\right] \tag{4.13}$$

In this case the hologram is no longer Bragg–matched. The shrinkage does not contribution to the second "sinc" term because hologram thickness is unchanged. Shrinkage along x'' changes the lateral size as well as the grating vector of the hologram, thus δ shows up in the first "sinc" term. An example of the resulting PSF is shown in Fig. 4-

2(d). The mainlobe is shifted, because the shrinkage increases the grating vector of the hologram along x'' so that in order to make the best Bragg match, the diffracted beam should be at a different angle.

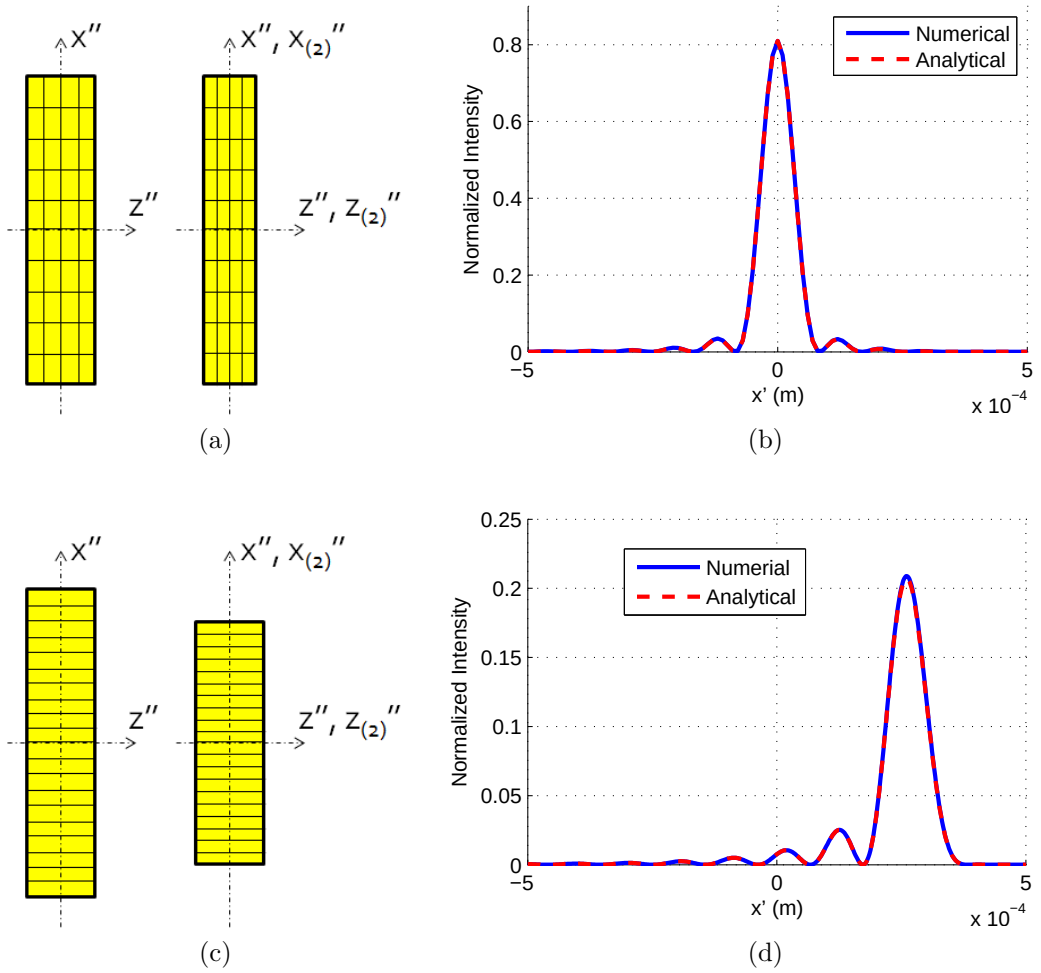

Figure 4-2: (Left) Shrinkage of the VH along (a) z'' and (c) x'' directions. (Right) The resulting PSFs when the compression ratio (b) $\delta = 0.1$ & (d) $\delta = 0.02$, respectively.

4.3.2 Compression

We consider compression along z'' axis, which tends to extend the hologram along x'' axis. The transformation matrix is

$$\mathbf{T} = \begin{pmatrix} 1+\nu\delta & 0 \\ 0 & 1-\delta \end{pmatrix}, \tag{4.14}$$

with $|\mathbf{T}| = (1-\delta)(1+\nu\delta)$, where ν is the Poisson's ratio. The calculated analytical equation of the resulting field is

$$\begin{aligned} q(x') &= (1+\nu\delta)L_x \cdot (1-\delta)L \\ &\quad \cdot \text{sinc}\left[\frac{L_x}{\lambda}\left(\frac{(1-\nu\delta)x_s}{f_1} + \frac{(1+\nu\delta)x'}{f_2}\right)\right] \text{sinc}\left[\frac{L}{2\lambda}\left(\frac{x_s^2}{f_1^2} - \frac{x'^2}{f_2^2}\right)\right]. \end{aligned} \quad (4.15)$$

This clearly confirms that compression is a combined case of hologram shrinkages discussed above.

4.3.3 Rotation

Rotation is another type of affine transformation. Assuming that the hologram has been rotated counter–clockwise by θ (see Fig. 4-3(a)), the coordinate transformation can be written as

$$\begin{aligned} x''_{(2)} &= x''\cos\theta + z''\sin\theta, \\ z''_{(2)} &= -x''\sin\theta + z''\cos\theta. \end{aligned} \quad (4.16)$$

This corresponds to a transformation matrix of

$$\mathbf{T} = \begin{pmatrix} \cos\theta & \sin\theta \\ -\sin\theta & \cos\theta \end{pmatrix}, \quad (4.17)$$

with $|\mathbf{T}| = 1$. This result makes sense because rotation does not induce any area change. Substitute into Eq. 4.6 and we will have the resulting PSF to be

$$\begin{aligned} q(x') &= L_x \cdot L \cdot \text{sinc}\left[\frac{L_x}{\lambda}\left(\frac{2x_s}{f_1} + \cos\theta\left(\frac{x'}{f_2} - \frac{x_s}{f_1}\right) - \sin\theta\left(\frac{x_s^2}{2f_1^2} - \frac{x'^2}{2f_2^2}\right)\right)\right] \\ &\quad \cdot \text{sinc}\left[\frac{L}{\lambda}\left(\sin\theta\left(\frac{x'}{f_2} - \frac{x_s}{f_1}\right) + \cos\theta\left(\frac{x_s^2}{2f_1^2} - \frac{x'^2}{2f_2^2}\right)\right)\right]. \end{aligned} \quad (4.18)$$

It is straightforward to see that rotation mixes the lateral and axial "sinc" terms discussed above, just like what rotation does to the VH system. It partially changes lateral structures into axial direction, and vice versa. Investigating rotation's influence

on the resulting PSF can be clearly done by looking into $\cos\theta$ and $\sin\theta$ that appear in Eq. 4.18. A PSF example is illustrated in Fig. 4-3(b).

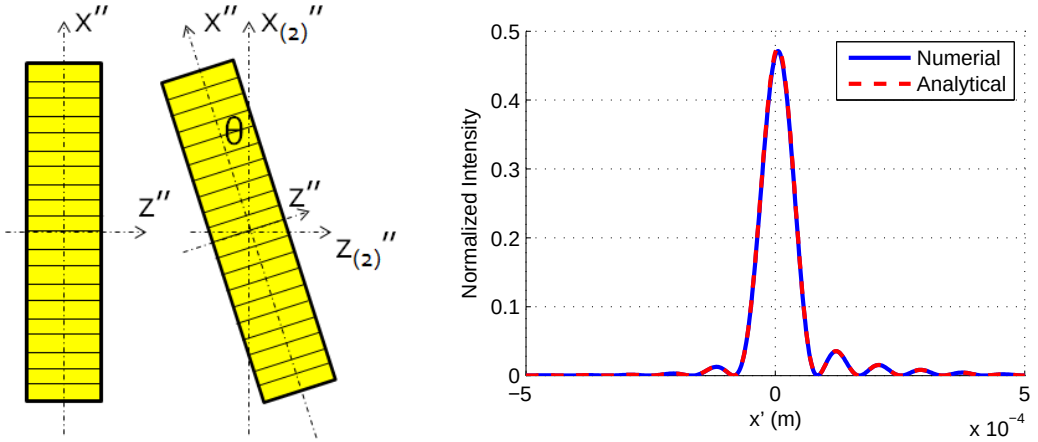

(a) (b)

Figure 4-3: (a) Rotation of the VH and (b) the resulting PSF when the rotation angle $\theta = 2^{o}$ calculated using both derived analytical equations and direct full numerical solution.

4.3.4 Shearing

We first analyze a shearing of hologram along x'' direction (Fig. 4-4(a)). Coordinate transform is

$$\begin{aligned} x''_{(2)} &= x'' + \alpha z'', \\ z''_{(2)} &= z'', \end{aligned} \tag{4.19}$$

where α is defined as the shearing ratio. The resulting transformation matrix is

$$\mathbf{T} = \begin{pmatrix} 1 & \alpha \\ 0 & 1 \end{pmatrix}. \tag{4.20}$$

Again we have $|\mathbf{T}| = 1$ because shearing, like rotation, does not change the grid area. Final PSF after this shearing is

$$\begin{aligned} q(x') &= L_x \cdot L \cdot \mathrm{sinc}\left[\frac{L_x}{\lambda}\left(\frac{x'}{f_2} + \frac{x_s}{f_1}\right)\right] \\ &\quad \cdot \mathrm{sinc}\left[\frac{L}{\lambda}\left(\left(\frac{x_s^2}{2f_1^2} - \frac{x'^2}{2f_2^2}\right) - \alpha\left(\frac{x_s}{f_1} - \frac{x'}{f_2}\right)\right)\right]. \end{aligned} \tag{4.21}$$

It is observed that the expression inside the first "sinc" term also appears in the second term with a coefficient of α. This is because shearing mixes part of the contributions from x'' axis into z'' direction. An example of the resulting PSF is shown in Fig. 4-4(b).

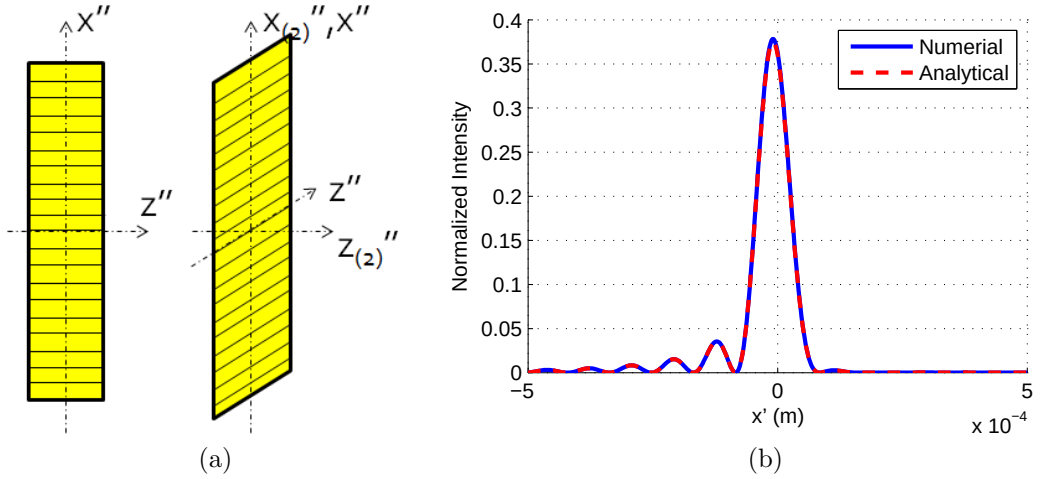

Figure 4-4: (a) Shearing of the VH along x'' direction and (b) the resulting PSF when the shearing ratio $\alpha = -0.04$.

The same analysis applies to a shearing along z'' axis; and the results show mixture of the quadratic term from axial thickness into the lateral "sinc" term. Detailed calculations are straightforward and not duplicated here.

It is clear from the above affine deformation examples that analytical solutions provide detailed physical intuitions and explanations on how the deformations influence the system and shape the final PSF. This information is not possible using numerical approaches. The analysis approach mentioned in this section potentially applies to all types of affine deformations.

4.4 Non–affine transformations

While for affine transformations it is possible to derive an elegant analytical solution for the resulting PSF on the detector, it is usually not possible to directly solve the integral and arrive at a straightforward equation for the PSF in the non–affine transformation case. In this section we will present this problem and propose that the approximation of stationary phase method can be used to find an analytical solution.

4.4.1 Bending

As a first example of non–affine deformation, we consider bending as shown in Fig. 4-5(a). Bending creates a curve along the hologram [62], and the radius of this curve is defined here as the bending radius R. Note that by the convention used in the thesis, a bending curved to the left (see Fig. 4-5(a)) results into a negative R since the radius extends to the left of the hologram. Radius R is positive when the bending curves to the right. We define "bending ratio" $\gamma = L/(2R)$ as a convenient measure of the amount of bending exerted on the hologram.

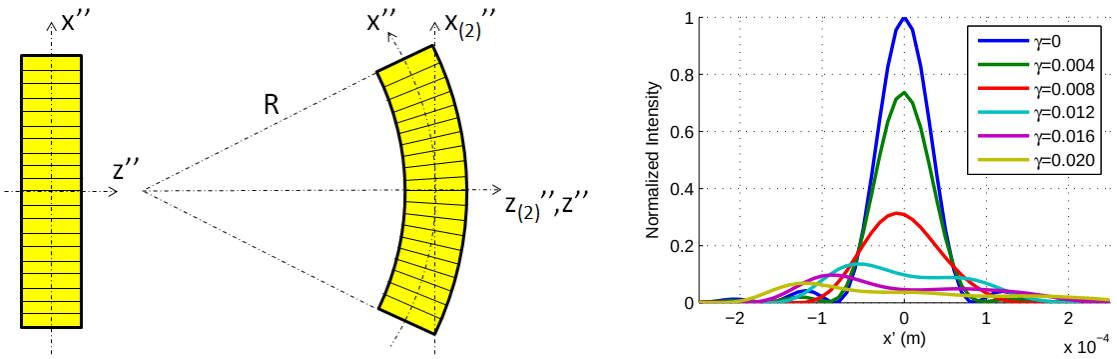

(a) (b)

Figure 4-5: (a) Bending of the VH. (b) Resulting PSFs at different bending ratios.

The transformation matrix of bending deformation can be expressed as

$$|\mathrm{T}| = \begin{pmatrix} \frac{R-z''}{R}\cos\frac{x''}{|R|} & -\frac{|R|}{R}\sin\frac{x''}{|R|} \\ \frac{R-z''}{|R|}\sin\frac{x''}{|R|} & \cos\frac{x''}{|R|} \end{pmatrix}, \tag{4.22}$$

where $|\mathbf{T}| = -\frac{z''-R}{R}$. The PSF at the detector is the result of the following double integral

$$\begin{aligned} q(x') &= \iint \mathrm{d}x''\mathrm{d}z''\mathrm{rect}(\frac{x''}{L_x})\mathrm{rect}(\frac{z''}{L})\left(\frac{z''-R}{-R}\right)\exp\left(-i\frac{2\pi}{\lambda}\frac{2x_s x''}{f_1}\right) \\ &\quad \cdot\exp\left[-i\frac{2\pi}{\lambda}\left(\frac{x'}{f_2}-\frac{x_s}{f_1}\right)\left(|R|\frac{R-z''}{R}\sin\frac{x''}{|R|}\right)\right] \\ &\quad \cdot\exp\left[-i\frac{2\pi}{\lambda}\left(\frac{x_s^2}{2f_1^2}-\frac{x'^2}{2f_2^2}\right)\left(R+(z''-R)\cos\frac{x''}{R}\right)\right]. \end{aligned} \tag{4.23}$$

It can be observed that both integration variables x'' and z'' appear in the same exponential terms, making a direct integral solution impossible to obtain. Examples of resulting PSFs are illustrated in Fig. 4-5(b). It can be seen that for larger bending ratios, the PSF widens and flattens, and its peak also decreases.

Fortunately, the integral along z'' can be analytically performed without any approximation and this reduces Eq. 4.23 into a single integral along x''

$$\begin{aligned} q(x') &= \int \mathrm{d}x''\mathrm{rect}(\frac{x''}{L_x})\left[\frac{\sin(\pi LA)}{\pi A}+\frac{L\cos(\pi LA)}{i\pi RA}+\frac{i\sin(\pi LA)}{2\pi^2 RA^2}\right]\exp\left(-i\frac{2\pi}{\lambda}\frac{2x_s x''}{f_1}\right) \\ &\quad \cdot\exp\left[-i\frac{2\pi}{\lambda}\left(\frac{x'}{f_2}-\frac{x_s}{f_1}\right)|R|\sin\frac{x''}{|R|}\right] \\ &\quad \cdot\exp\left[-i\frac{2\pi}{\lambda}\left(\frac{x_s^2}{2f_1^2}-\frac{x'^2}{2f_2^2}\right)R\left(1-\cos\frac{x''}{R}\right)\right], \end{aligned} \tag{4.24}$$

where

$$A = -\frac{1}{\lambda}\left(\frac{x'}{f_2}-\frac{x_s}{f_1}\right)\frac{|R|}{R}\sin\frac{x''}{|R|}+\frac{1}{\lambda}\left(\frac{x_s^2}{2f_1^2}-\frac{x'^2}{2f_2^2}\right)\cos\frac{x''}{R}. \tag{4.25}$$

Eq. 4.24 can no longer be reduced analytically. Stationary phase method should be used as an approximation to find an analytical solution.

4.4.2 Stationary phase method

The stationary phase method [16, 25, 30] in the one–dimensional case is an approximation procedure for evaluating the following integrals

$$I = \int_C f(x) \exp(i\Lambda\phi(x))\mathrm{d}x, \tag{4.26}$$

where Λ is a large constant parameter ($\Lambda \gg 1$), C is certain domain of integration, $\phi(x)$ is a fast–varying function over most of range C, and $f(x)$ is a slowly–varying function comparing with $f(x)$. For most of the integral regions, $\phi(x)$ is rapid–varying therefore the integral result I is approximated zero over these ranges. Main contributions are from some critical points where this assumption fails. One significant contribution is from the point of stationary phase x_0, where $\phi'(x_0) = 0$. At $x = x_0$, $\phi(x)$ is no longer fast–oscillating and the contribution can be calculated by expanding $\phi(x)$ in a Taylor series asymptotically to the second order derivative and substituting back into Eq. 4.26 [16, 25]

$$I = \exp(i\Lambda\phi(x_0))\frac{1}{\sqrt{\Lambda}}\sqrt{\frac{2\pi}{|\phi''(x_0)|}}\exp\left(i\frac{\mathrm{sign}(\phi''(x_0))\cdot\pi}{4}\right)f(x_0). \tag{4.27}$$

Many other types of critical points will be discussed later. Final I is a sum of contributions from all critical points along the integral domain.

This stationary phase method has been widely used in electromagnetic scattering, diffraction and radiation problems as a standard approach to solve the diffraction integrals [17, 29, 76]. In this section, we propose that similar approximation can be used to facilitate the integral of calculating PSFs of VH imaging systems under non–affine deformations, and help reach a quasi–analytical solution.

Integration boundaries and poles

We first note that for integral of Eq. 4.24, the corresponding $f(x)$ is a summation of three terms

$$\frac{\sin(\pi LA)}{\pi A} + \frac{L\cos(\pi LA)}{i\pi RA} + \frac{i\sin(\pi LA)}{2\pi^2 RA^2}. \tag{4.28}$$

It is beneficial to separate them and write Eq. 4.24 as a sum of three integrals. We refer to these three integrals as Part 1, Part 2, and Part 3. The following discussion focuses on Part 1, while Part 2 & 3 can be analyzed similarly. The comparison of contributions from all three components will also be illustrated later. Furthermore, the term $\sin(\pi LA)$ is not slowly–varying but it can be written as

$$\frac{\exp(i\pi LA) - \exp(-i\pi LA)}{2i}. \tag{4.29}$$

Comparing with the standard expression of stationary phase method shown in Eq. 4.26, Part 1 can be re–written as

$$f(x) = \frac{1}{2i\pi A}, \tag{4.30}$$

$$\begin{aligned}\exp(i\Lambda\phi(x'')) &= [\exp(i\pi LA) - \exp(-i\pi LA)]\exp\left(-i\frac{2\pi}{\lambda}\frac{2x_s x''}{f_1}\right) \\ &\cdot \exp\left[-i\frac{2\pi}{\lambda}\left(\frac{x'}{f_2} - \frac{x_s}{f_1}\right)|R|\sin\frac{x''}{|R|}\right] \\ &\cdot \exp\left[-i\frac{2\pi}{\lambda}\left(\frac{x_s^2}{2f_1^2} - \frac{x'^2}{2f_2^2}\right)R\left(1-\cos\frac{x''}{R}\right)\right],\end{aligned} \tag{4.31}$$

where Λ is defined here as $2\pi/\lambda$, which satisfies $\Lambda \gg 1$.

Now we are able to solve Part 1. We first realized that the term A expressed in Eq. 4.25 can be zero within the integral range, resulting in a pole (one type of critical points), denoted as x_p. Beside, $\mathrm{rect}(\frac{x''}{L_x})$ introduces two integration boundaries at $a = -L_x/2$ and $b = L_x/2$. At these boundaries, oscillations from exponential terms stop abruptly; thus the contributions from these points should be considered since fast–varying expression does not cancel out with these sharp changes. An example

is illustrated in Fig. 4-7(a)–(c). Considering these two types of critical points (poles and integration boundaries) together, final result is [16]

$$I = \frac{e^{j\Lambda\phi(a)}}{\phi'(a)}\frac{j}{\Lambda}f(a) - \frac{e^{j\Lambda\phi(b)}}{\phi'(b)}\frac{j}{\Lambda}f(b) \begin{cases} +ic\pi\exp(i\Lambda\phi(x_p)) & \text{if} \quad \phi'(x_p) > 0 \\ -ic\pi\exp(i\Lambda\phi(x_p)) & \text{if} \quad \phi'(x_p) < 0 \end{cases}, \quad (4.32)$$

where $c = 1/\{[1/f(x)]'|_{x_p}\}$. As an example, we choose bending ratio $\gamma = 0.030$, and results are shown in Fig. 4-6. It is interesting to see that the contributions from the poles outline the envelope of the PSF; and the boundaries add oscillations. Note that kinks are observed in both roll–off areas near $x' = -3.2 \times 10^{-4}$ m and $x' = 3.5 \times 10^{-4}$ m. It is obvious that in these regions contributions from other factors should be included.

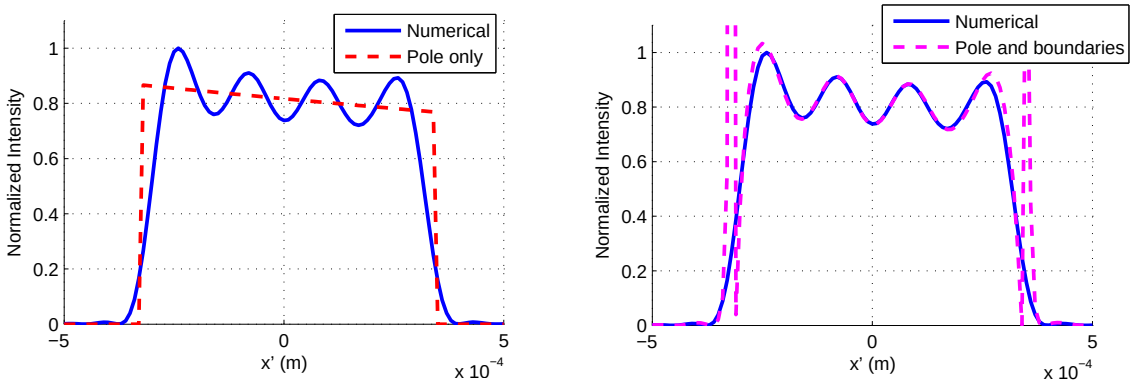

Figure 4-6: PSFs calculated using Eq. 4.32 by including the contributions (a) only poles and (b) both poles & boundaries, compared with full numerical solution.

Close stationary points

We plotted $f(x)$ and $\exp(i\Lambda\phi(x))$ for integral at different detector positions in Fig. 4-7. At roll–off region, e.g. $x' = -3.2\times10^{-4}$ m (Fig. 4-7(d)–(f)), it can be observed that two stationary points appear within the integral range where $\phi'(x) = 0$. Furthermore, these two stationary points are close to each other (within a few cycles of exponential oscillations), and they are also both close enough to the pole of $f(x)$. That is to say, the contribution from each critical point should not be added independently, instead,

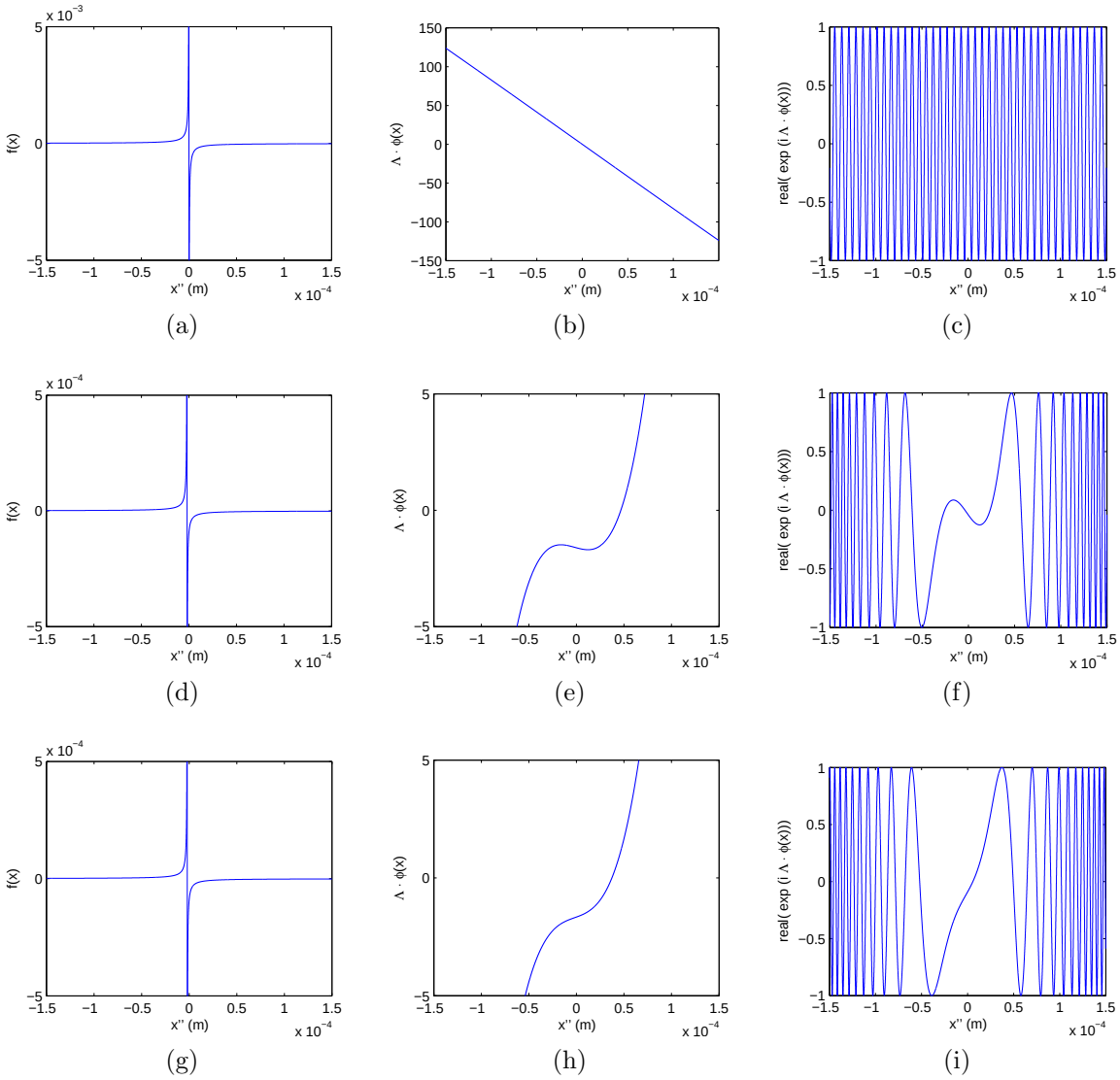

Figure 4-7: Expressions of $f(x)$ (left), $\Lambda\phi(x)$ (middle) and real(exp($i\Lambda\phi(x)$))(right) for one dimensional integral of Eq. 4.24 at detector positions of $x' = 0$ (top), $x' = -3.2 \times 10^{-4}$ m (middle), and $x' = -3.1 \times 10^{-4}$ m (bottom) (see Fig. 4-6). Note that only part of the integral range is shown.

all critical points need to be combined in order to find the total contribution. For detailed quantitative analysis on how close two critical points should be so that their individual contributions are not independent any more, see [29].

Now we have in total five critical points, including one pole, two stationary points, and two integration boundaries. The following identical relationship can be used here to get rid of one integration boundary

$$\begin{aligned}\int_a^b f(x)\exp\left(i\Lambda\phi(x)\right)\mathrm{d}x &= \int_a^{+\infty} f(x)\exp\left(i\Lambda\phi(x)\right)\mathrm{d}x \\ &\quad -\int_b^{+\infty} f(x)\exp\left(i\Lambda\phi(x)\right)\mathrm{d}x, \end{aligned} \tag{4.33}$$

resulting into four critical points.

According to [16], the combined contributions from these four critical points can be expressed as

$$\begin{aligned} I &= \exp\left(i\Lambda\phi_0\right)\{-2\pi i f(x_p)\mathrm{Af}_{\mathrm{in}}(-\Lambda^{2/3}\xi,\Lambda^{1/3}\beta,\Lambda^{1/3}q) \\ &\quad +\pi A_0\Lambda^{-1/3}\Phi(-\Lambda^{2/3}\xi,\Lambda^{1/3}q)-\pi B_0 i\Lambda^{-2/3}\Phi'(-\Lambda^{2/3}\xi,\Lambda^{1/3}q)\}, \end{aligned} \tag{4.34}$$

where

$$\mathrm{Af}_{\mathrm{in}}(p,\beta,q)=\frac{i}{2\pi}\int_q^{\infty} e^{i(t^3/3+tp)}\frac{dt}{t-\beta} \tag{4.35}$$

is the incomplete Airy–Fresnel integral,

$$\Phi(p,q)=\frac{1}{2\pi}\int_q^{\infty} e^{i(t^3/3+tp)}dt \tag{4.36}$$

is the incomplete Airy function,

$$\Phi'(p,q)=\frac{1}{2\pi}\int_q^{\infty} it\ e^{i(t^3/3+tp)}dt \tag{4.37}$$

is the incomplete Airy function's derivative, $\xi = [(3/4)\cdot(\phi(x_1)-\phi(x_2))]^{2/3}$ is a representation of two stationary points at x_1 & x_2, β is a solution of $\phi(x_p)=\phi_0+$

$\beta^3/3-\xi\beta$ which is an indication of the pole at x_p, q is a solution of $\phi(a) = \phi_0+q^3/3-\xi q$ which represents the position of the integral boundary at $x = a$, and

$$A_0 = \xi^{1/4}\left[\frac{f(x_2)}{x_2 - x_p}\sqrt{\frac{2}{|\phi''(x_2)|}} + \frac{f(x_1)}{x_1 - x_p}\sqrt{\frac{2}{|\phi''(x_1)|}}\right] - \frac{2\beta f(x_p)}{\xi - \beta^2}, \tag{4.38}$$

$$B_0 = \xi^{-1/4}\left[\frac{f(x_2)}{x_2 - x_p}\sqrt{\frac{2}{|\phi''(x_2)|}} - \frac{f(x_1)}{x_1 - x_p}\sqrt{\frac{2}{|\phi''(x_1)|}}\right] - \frac{2f(x_p)}{\xi - \beta^2}. \tag{4.39}$$

Close quasi–stationary points

In other positions of the roll–off region, e.g. $x' = -3.1 \times 10^{-4}$ m (see Fig. 4-7(g)–(i)), first derivative of $\phi(x)$ does not go zero, meaning there are no stationary points. However, in this case, another type of critical points, quasi–stationary points, is important, when these two points are close to each other. Quasi–stationary points are *virtual* stationary points at "imaginary" positions x_{q1} and x_{q2} where $\phi'(x) = 0$. For example, if $\phi(x) = x^3 + 3x$, it has quasi–stationary points at $x_{q1} = -1i$ and $x_{q2} = 1i$.

In this case, we have four critical points, one pole, two quasi–stationary points and on integration boundary. The total contributions can be expressed as [16]

$$\begin{aligned} I \;=\; & \exp(i\Lambda\phi_0)\{-2\pi i f(x_0)\mathrm{Af_{in}}(-\Lambda^{2/3}(2/\phi''')^{1/3}\alpha, \Lambda^{1/3}\beta, \Lambda^{1/3}q) \\ & +2\pi(2/\phi''')^{1/3} f_0 \Lambda^{-1/3}\Phi(-\Lambda^{2/3}(2/\phi''')^{1/3}\alpha, \Lambda^{1/3}q) \\ & -2\pi i(2/\phi''')^{2/3} f_1 \Lambda^{-2/3}\Phi'(-\Lambda^{2/3}(2/\phi''')^{1/3}\alpha, \Lambda^{1/3}q)\}, \end{aligned} \tag{4.40}$$

where $\alpha = \min(\phi'(x))$ is an indication of two quasi–stationary points, $f_0 = f(0)$, and $f_1 = f'(0)$.

We apply Eq. 4.34 and Eq. 4.40 at both roll–off regions and the resulting PSF is shown in Fig. 4-8. The kinks shown in Fig. 4-6(b) have disappeared, and the analytical result matches that of full numerical solution.

Now that we have found a quasi–analytical solution of Part 1. Similar analysis applies to Part 2 and Part 3. The total PSF, as well as the separate contributions from these three parts are plotted in Fig. 4-9. We notice that the major contribution

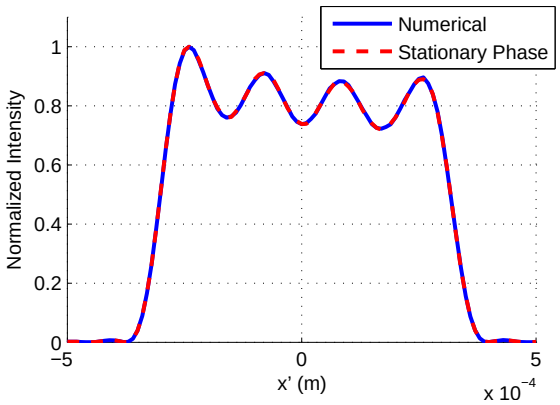

Figure 4-8: PSF at the detector for a bent hologram calculated using stationary phase approximation combining four critical points, compared with full numerical solution.

to the final PSF is from Part 1. This is because we assume a small bending so that $|R|/L \gg 1$ and $|R \cdot A| \gg 1$ (see Eq. 4.24). Calculation of Part 1 suffices if the required accuracy is not high.

4.4.3 Twisting

As another example of non–affine deformation, we consider twisting. Twisting, different from all cases discussed above, does not have an invariant axis therefore all three coordinate axes should be considered. In this section we consider twisting deformation along the optical axis (z'' axis), and instead of a rectangular–shaped volume hologram, we here use a volume hologram shaped as a cylinder (with the cylinder axis coincident with both the optical axis of propagation and the direction of the torque vector). Cylindrical hologram allows for easy application of uniform twisting torque on the hologram.

For twisting, the rotating angles at different z'' planes are [62]

$$\theta(z'') = \frac{z''}{L/2}\theta_m, \tag{4.41}$$

where θ_m is the maximum twisting angle on each side. Typical PSFs at different θ_m values are plotted in Fig. 4-10. It can be observed that with the increasing of θ_m, the PSF extends along y' axis, and its peak reduces. This can be intuitively explained as

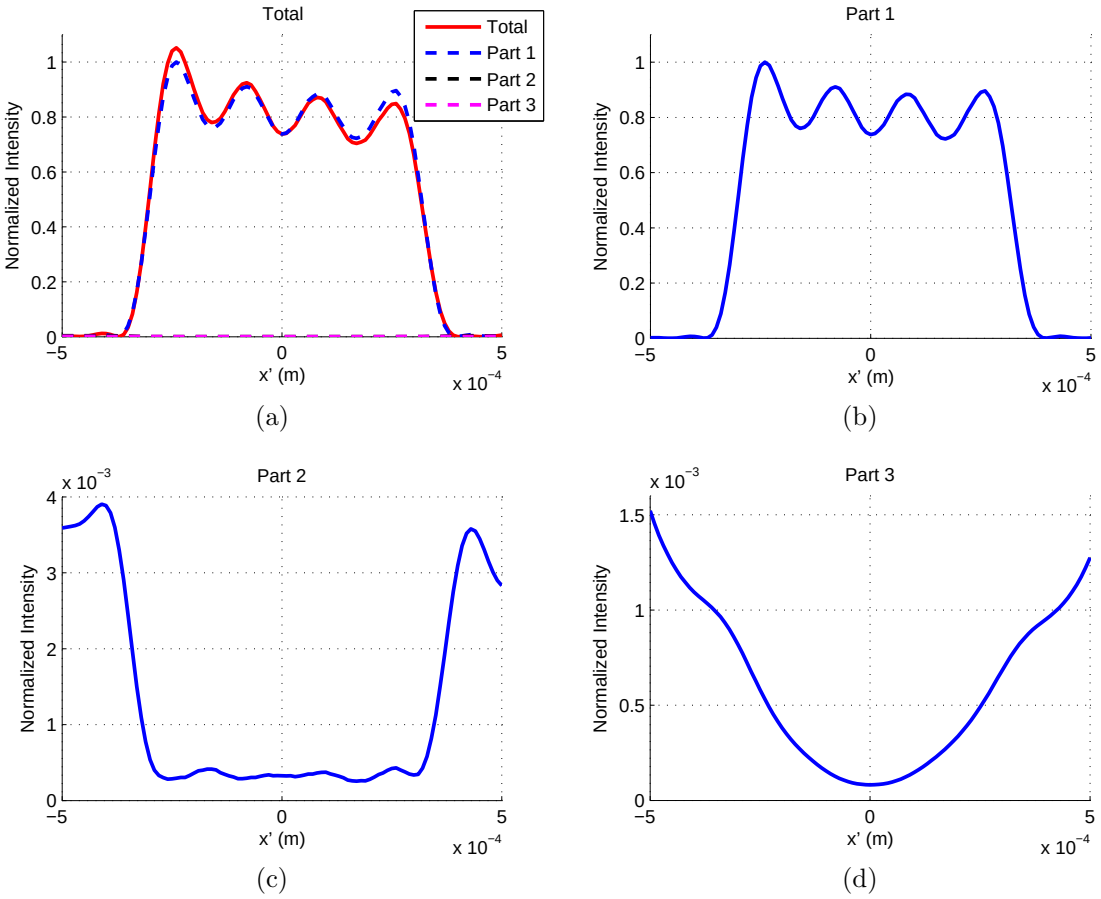

Figure 4-9: (a) PSFs calculated from Part 1–3 and combined. (b)–(d) Contributions from Part 1–3 separately.

shown in Fig. 4-11. The probe beam was diffracted by platelets located at different z'' positions with grating vectors rotated at different angles, each contributing to a spot at different position of the detector. Adding the contributions from all platelets result into the extended PSF.

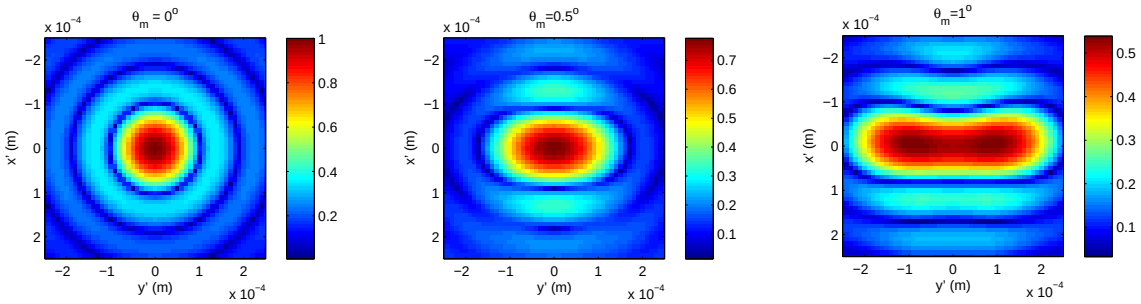

(a) (b) (c)

Figure 4-10: PSFs for twisting at different maximum twisting angles: (a) $\theta_m = 0^o$ (without deformation), (b) $\theta_m = 0.5^o$, and (c) $\theta_m = 1^o$. Note that in order to show sidelobes clearly, $\sqrt{q(x', y')}$ is plotted instead of the actual intensity, which is proportional to $|q(x', y')|^2$.

In order to derive an analytical solution, we start with the transformation matrix of twisting

$$\mathbf{T} = \begin{pmatrix} \cos(\frac{2z''}{L}\theta_m) & -\sin(\frac{2z''}{L}\theta_m) & 0 \\ \sin(\frac{2z''}{L}\theta_m) & \cos(\frac{2z''}{L}\theta_m) & 0 \\ 0 & 0 & 1 \end{pmatrix} \tag{4.42}$$

where $|\mathbf{T}| = 1$, which is clear that twisting does not change the volume of each integral

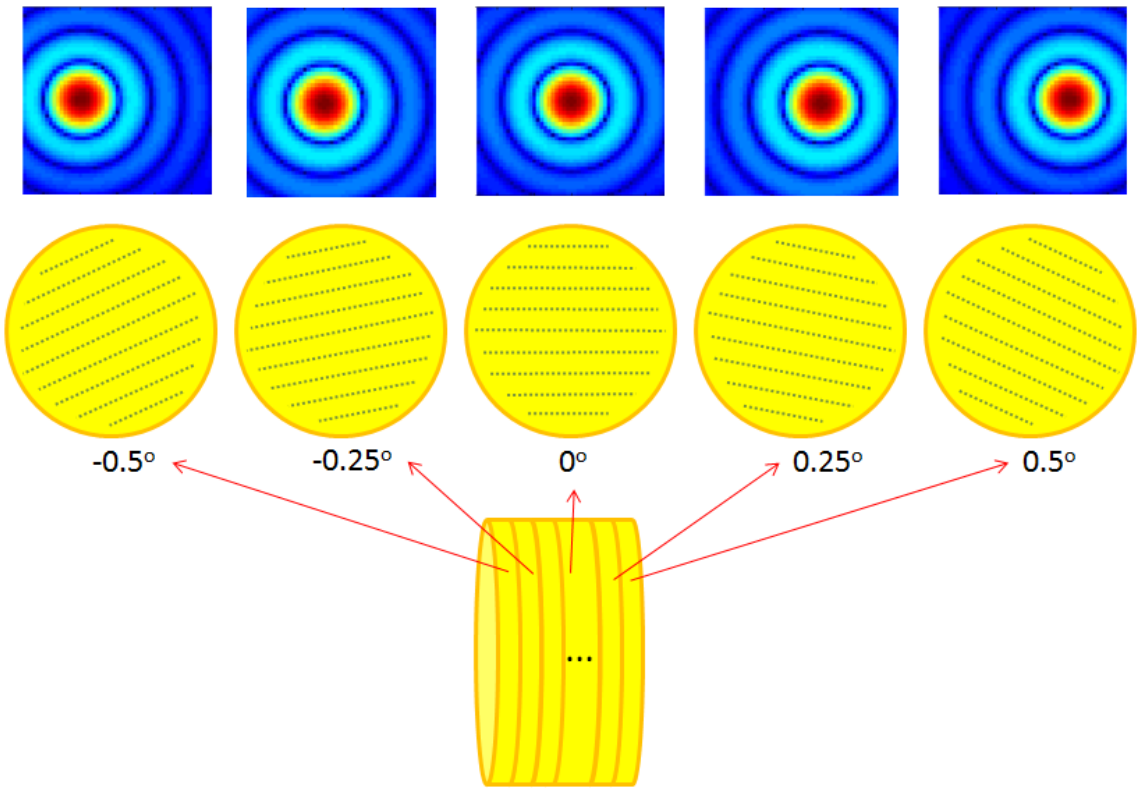

(a)

Figure 4-11: Intuitive explanation of the PSF shape after twisting.

voxel. According to Eq. 4.6, the resulting PSF is

$$\begin{aligned} q(x',y') &= \iiint \mathrm{d}x''\mathrm{d}y''\mathrm{d}z''\mathrm{circ}\left(\frac{\sqrt{x''^2+y''^2}}{R}\right)\mathrm{rect}\left(\frac{z''}{L}\right) \\ &\cdot\exp\left[j2\pi\frac{x_s(\cos(\frac{2z''}{L}\theta_m)x''-\sin(\frac{2z''}{L}\theta_m)y'')}{\lambda f_1}\right]\exp\left[-j\pi\frac{x_s^2z''}{\lambda f_1^2}\right] \\ &\cdot\exp\left[-j2\pi\frac{2x_sx''}{\lambda f_1}\right]\exp\left[-j2\pi\frac{x'(\cos(\frac{2z''}{L}\theta_m)x''-\sin(\frac{2z''}{L}\theta_m)y'')}{\lambda f_1}\right] \\ &\cdot\exp\left[-j2\pi\frac{y'(\sin(\frac{2z''}{L}\theta_m)x''+\cos(\frac{2z''}{L}\theta_m)y'')}{\lambda f_1}\right] \\ &\cdot\exp\left[j2\pi\frac{(x'^2+y'^2)z''}{2f_2^2\lambda}\right], \end{aligned} \tag{4.43}$$

where R is the radius of the cylinder. Integration along x'' and y'' can be derived exactly, reducing into

$$\begin{aligned} q(x',y') &= \int \mathrm{d}z''\mathrm{rect}\left(\frac{z''}{L}\right)\pi R^2\mathrm{jinc}(R\sqrt{u^2+v^2}) \\ &\cdot\exp\left[-i\pi\frac{x_s^2z''}{\lambda f_1^2}\right]\exp\left[i2\pi\frac{x'^2+y'^2}{2f_2^2}\frac{z''}{\lambda}\right], \end{aligned} \tag{4.44}$$

where

$$u = \frac{1}{\lambda}\left[-\frac{x_s\cos(\frac{2z''}{L}\theta_m)}{f_1}+\frac{2x_s}{f_1}+\frac{x'\cos(\frac{2z''}{L}\theta_m)}{f_2}+\frac{y'\sin(\frac{2z''}{L}\theta_m)}{f_2}\right], \tag{4.45}$$

$$v = \frac{1}{\lambda}\left[+\frac{x_s\sin(\frac{2z''}{L}\theta_m)}{f_1}-\frac{x'\sin(\frac{2z''}{L}\theta_m)}{f_2}+\frac{y'\cos(\frac{2z''}{L}\theta_m)}{f_2}\right], \tag{4.46}$$

$$\mathrm{jinc}(x) = \frac{J_1(2\pi x)}{\pi x}, \tag{4.47}$$

where J_1 is the Bessel function of the first kind [64].

Without deformation, i.e. $\theta_m = 0^{\mathrm{o}}$, the PSF can be calculated as

$$\begin{aligned} q(x',y') &= \pi R^2\cdot\mathrm{jinc}\left[\frac{R}{\lambda}\sqrt{\left(\frac{x_s}{f_1}+\frac{x'}{f_2}\right)^2+\left(\frac{y'}{f_2}\right)^2}\right] \\ &\cdot L\cdot\mathrm{sinc}\left[\frac{L}{\lambda}\left(\frac{x_s^2}{2f_1^2}-\frac{x'^2+y'^2}{2f_2^2}\right)\right]. \end{aligned} \tag{4.48}$$

This result matches with the PSF result show in Fig. 4-10(a). However, with twisting, because the integral variable z'' exists inside the jinc function, an exact analytical solution for Eq. 4.44 is not possible. A similar procedure of incorporating stationary phase method like the one used in the bending transformation above should be used.

First of all, $\sqrt{u^2+v^2}$ can be re–written as

$$\sqrt{u^2+v^2} = \frac{1}{\lambda}\sqrt{\left(\frac{x_s}{f_1}+\frac{x'}{f_2}\right)^2+\left(\frac{y'}{f_2}\right)^2} + \frac{1}{\lambda}\frac{\frac{2x_s y'}{f_1 f_2}}{\sqrt{\left(\frac{x_s}{f_1}+\frac{x'}{f_2}\right)^2+\left(\frac{y'}{f_2}\right)^2}}\frac{2z''}{L}\theta_m \qquad (4.49)$$

assuming that $(2z''\theta_m/L) \ll 1$. And the jinc function can be approximated as below [2]

$$\text{jinc}(x) = \begin{cases} \cos(\pi x) & \text{if} \quad |x| < 0.3268 \\ \sqrt{\frac{1}{\pi|\pi x|^3}}\cos(|2\pi x| - 3\pi/4) & \text{if} \quad |x| \geq 0.3268 \end{cases}. \qquad (4.50)$$

This approximation has been confirmed in Fig. 4-12.

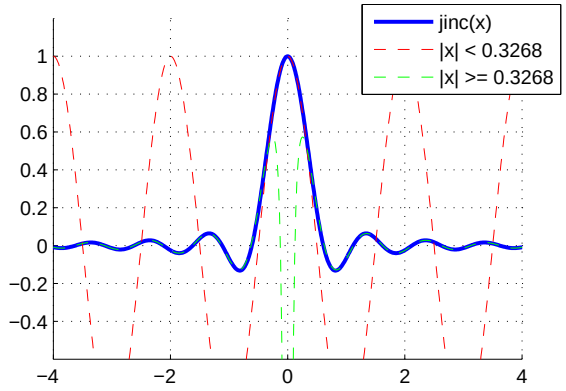

Figure 4-12: Approximation of jinc function (Eq. 4.50).

With Eq. 4.49 and Eq. 4.50, the original 1D integral (Eq. 4.44) has been reduced and expressed in the standard form of stationary phase method (Eq. 4.26). Using the same analysis discussed in Section 4.4.2, quasi–analytical solution can be derived. The resulting PSF at the detector is illustrated in Fig. 4-13, together with the difference to the result from full numerical approach. Analytical result is in agreement with the numerical result.

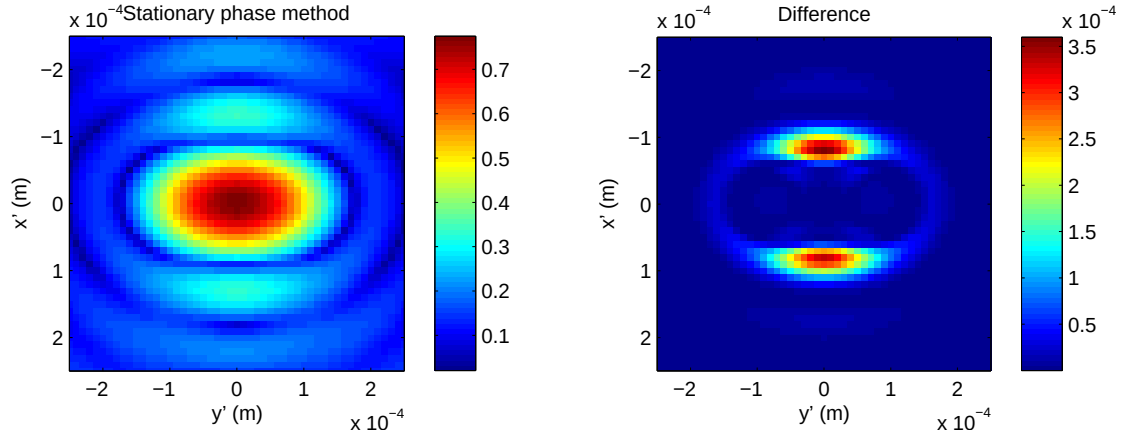

Figure 4-13: (a) PSF calculated using stationary phase method approximation, and (b) its difference to the result calculated using full numerical result (Fig. 4-10(b)). Maximum twisting angle is $\theta_m = 0.5^o$.

4.5 Conclusion

In this chapter, we proposed a quasi–analytical method for calculating the PSF in transformational volume holography. Bulk deformations are applied on the hologram, and for affine transformation, an analytical equation of the final PSF can be directly derived. However, for non–affine transformations, straightforward solution for the integral is not possible. The approximation of stationary phase method is used, and we are able to find a quasi–analytical solution. Transformational volume holography provide more design flexibility for imaging systems. And analytical solution not only reduces the computing cost, but also enhances the physical intuition between the deformation and resulting PSF. This approach proposed here is general and can be potentially applied to other types of bulk transformations, or a combinations of different types.

THIS PAGE INTENTIONALLY LEFT BLANK

Chapter 5

Subwavelength dielectric photonic cloak

In all previous chapters we have been discussing diffractive optical elements, where the wavelength of light is comparable or smaller than the fine structures of optical devices. We now turn to the subwavelength regime, where the unit feature of a device is significantly smaller than the operational optical wavelength. In subwavelength regime, the light propagating along the device does not "see" the fine structure; instead, an effective medium, i.e. an effective permittivity or refractive index, is observed. Subwavelength devices provide rich opportunities for light manipulation because the fine tuning of permittivity of dielectric materials, while not straightforward in bulk devices, can be relatively more easily realized by using elements of different sizes in the unit cell, creating an arbitrary refractive index in the desired region.

Subwavelength optical devices have found many applications [47, 48, 100, 104, 137], and are considered to be good candidates for the future of "optical circuits". In this chapter I will focus on the design of a photonic cloak using subwavelength dielectric elliptical rod arrays, which are capable of accommodating mechanical and optical components in integrated photonic devices [12, 55, 56]. These designs can significantly reduce the size of photonic devices, and find lots of applications in next–generation optical circuits.

5.1 Motivation

Photonic devices need mechanical components to support, connect and stack functional photonic components. Most previous device designs simply separate the mechanical components from the photonic components beyond a sufficient distance at which the interference is negligible. With increasing demand for smaller device sizes, it is desirable to integrate mechanical components into photonic components directly, thus making photonic devices more compact with even potential extension to the multilayered layout analogous to integrated circuits. Fig. 5-1 illustrates how mechanical components should be combined with photonic components in order to reduce the size of devices.

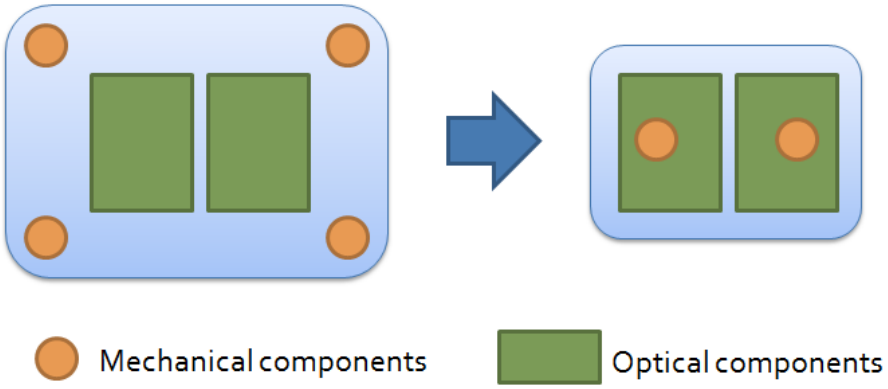

Figure 5-1: Illustration of accommodating mechanical components into photonic components, reducing the size of optical elements.

We propose a cloaking method to embed mechanical connections inside photonic components of integrated photonic devices. Different from previous cloak designs [20, 24, 38, 42, 86, 90, 92, 108, 111, 118, 137, 147, 148] generally aiming to make objects free from external electromagnetic detection, here this idea is applied to accommodating mechanical components into a photonic device in a more compact way. Our design candidate is a photonic subwavelength cloak made of elliptical rod arrays. Similar structures have been utilized in photonic crystals for both imaging [40] and nonlinear second harmonic generation [89]. Our design consists of uniform square unit cells with elliptical silicon rods immersed in air, which achieves anisotropy and homogeneity simultaneously, and will greatly facilitate the fabrication process [132]. As examples

of this cloaking design, cloaks that suppress the interference from the periphery and the inner region of the waveguide are designed and numerically verified with the finite–difference time–domain (FDTD) method. It is the first practical design for accommodating non–photonic components in integrated photonic components, which will provide more flexibility for designing future photonic devices.

For our design, a ground–plane cloak is located on a perfect electric conductor (PEC) ground plane, operated in two–dimensional (2D) plane perpendicular to the ground plane under transverse magnetic (TM) illumination (electric field lying in the 2D plane). An infinitely large cloaking region is created by transforming the space, making the ground plane interface away from its original location. In this way, the transformed medium remains homogeneous, but it has to be anisotropic in order to let the ground plane appear at its original position after the transformation (see Fig. 5-3). Elliptical rod arrays are used to achieve required anisotropy. The second example is one–dimensional cloak which is able to hide objects in a diamond shape region when illuminated by a plane wave (see Fig. 5-5). By proper tuning of the size of the unit cell and choice of constitutive parameters for the bulk material used for the rods, this cloak design works in any regime of the electromagnetic spectrum.

5.2 Implementation of anisotropy with elliptical rods

We use elliptical rod arrays (see Fig. 5-2(a)) to implement the material anisotropy. Fig. 5-2(c) shows the isofrequency curves from the dispersion diagram of a two dimensional (2D) unit cell with silicon elliptical rod (permittivity $\epsilon = 12$) immersed in air ($\epsilon = 1$). The 2D assumption generally makes sense, but our recent research has shown that exceptions do exist in extremely thin slabs [58]. A complete analysis of finite thickness effects is in the next chapter. The free space wavelength is $\lambda = 8a$, where a is the lattice constant; this operating wavelength is indicated as the bold blue line in Fig. 5-2(c). The effective refractive index for a particular wave vector $\mathbf{k}$ is

determined by $n_{\text{eff}} = c\mathbf{k}/\omega$ based on the isofrequency diagram, where c is the velocity of light in free space and ω is the frequency. From the isofrequency line, we determine the effective index surface, which is approximately an ellipse with effective principal indices $n_x = 1.30$ and $n_y = 1.80$. Note that this significant anisotropy exists only for transverse magnetic (TM) illumination, whose polarization will be utilized in this chapter. As a comparison, the isofrequency diagram of a lattice with circular rods of radius $r = 0.294a$ is illustrated in Fig. 5-2(d), where the effective index surface is a sphere with effective index $n_0 = 1.30$.

5.3 Cloaking and accommodating examples

5.3.1 Accommodation of peripheral non–photonic components

Now we proceed to design a cloak using the elliptical rod array for accommodating more peripheral non–photonic components. We start with a uniform medium above a perfect electric conductor (PEC) where the PEC is assumed to be the boundary of the photonic functional region. It is worth mentioning that although we use PEC to serve as a reflective surface for the sake of simplicity, this design also works for total internal reflection at the boundary in absence of the PEC. We then reduce the size of the medium immediately above the boundary along the y direction to create an empty area for placing more peripheral mechanical components, as shown in Fig. 5-3. The medium after transformation should be anisotropic in order for the boundary to appear virtually at its original position [69, 147], thus maintaining the photonic performance. Assuming that the size of the medium along y direction has been reduced from unit size 1 to $1 - \delta$, the relative permittivity and permeability tensors become [147]

$$\bar{\bar{\epsilon}} = \bar{\bar{\mu}} = \begin{pmatrix} 1/(1-\delta) & 0 & 0 \\ 0 & 1-\delta & 0 \\ 0 & 0 & 1/(1-\delta) \end{pmatrix}. \tag{5.1}$$

In terms of practical implementation, it is preferable to use only non–magnetic materials. Thus, under TM illumination, while keeping the z component of $\bar{\bar{\mu}}$ equal to 1, the permittivity tensor should be [147]

$$\bar{\bar{\epsilon}} = \epsilon_0 \begin{pmatrix} 1/(1-\delta)^2 & 0 & 0 \\ 0 & 1 & 0 \\ 0 & 0 & 1/(1-\delta)^2 \end{pmatrix}. \tag{5.2}$$

Therefore, the squeezed medium exhibits anisotropy with $n_x = n_0$ and $n_y = \gamma n_0$, where $\gamma = 1/(1-\delta)$.

Fig. 5-4(a) illustrates the original structure where a uniform photonic medium is terminated by a PEC boundary. The uniform medium is implemented with an array of circular silicon rods with radius $r = 0.294a$ with isotropic effective refractive index $n_0 = 1.30$, as previously calculated in Fig. 5-2(b). The thickness of the rod array and the PEC along y axis are $96a$ and $5a$, respectively. To achieve more space for peripheral mechanical components, the lower part of the uniform layer, with thickness of $54a$ along y axis immediately above the PEC is transformed to an anisotropic medium with thickness of $39a$. The corresponding squeezing factor is $\delta = 5/18$ resulting in anisotropy with $n_x = 1.30$ and $n_y = 1.80$, as we previously calculated from Fig. 5-2(a).

The resulting structure is shown in Fig. 5-4(b). From top to bottom, this structure contains four layers: (1) circular rod arrays of thickness $42a$ along y axis, (2) elliptical rod arrays of thickness $39a$, (3) PEC layer with thickness $5a$ and (4) region for more mechanical components with thickness $15a$. FDTD results of both the structures are illustrated and compared at Fig. 5-4(c)(d). It can be observed that the resulting output beam profile is the same as that of the original circularly rod structure; hence the photonic medium maintains its performance although its size is reduced and more mechanical components can be accommodated around the periphery. Some reflection appears at the boundary of the circular and elliptical rod arrays, but it can be suppressed by using anti–reflection techniques (see Section 5.4 for more details). In addition to accommodating mechanical components, this design can also be applied

to the isolation layer between two neighboring photonic components for more compact layout design in the future.

5.3.2 Accommodation of internal non–photonic components

As another example, we show how to use elliptical rod arrays for accommodating non–photonic components inside a waveguide directly. Similar to peripheral case, we first transform the space to create a parallelogram region. The non–photonic components are placed in this region. The original isotropic media above and below the parallelogram region are transformed, resulting in four triangular uniform anisotropic regions. Under TM illumination, an illustration of the transformation and resulting ray–tracing [4, 112] results are shown in Fig. 5-5.

The transformation from virtual coordinates (x, y) to physical coordinates (x', y') is [24, 142, 148]

$$x' = x; \qquad y' = \kappa y + \tau(a - |x|), \tag{5.3}$$

where $\kappa = [\tan(\alpha+\beta) - \tan\beta]/\tan(\alpha+\beta)$ and $\tau = \tan\beta$. To make the materials non-magnetic while maintaining the required refractive indices, the permittivity tensor in the $x - y$ plane becomes [142]

$$\bar{\bar{\epsilon}}' = \epsilon_0 \begin{pmatrix} 1/\kappa^2 & -\tau/\kappa^2 \\ -\tau/\kappa^2 & 1 + \tau^2/\kappa^2 \end{pmatrix}. \tag{5.4}$$

The corresponding optical axes are all aligned to the vertical axis with angle [148]

$$\theta = \frac{1}{2} \arctan \frac{2\tau}{\kappa^2 + \tau^2 - 1}. \tag{5.5}$$

Detailed design layout of the device is shown in Fig. 5-6. Here $\theta = 30°$ with effective refractive indices $n_x = 1.30$ and $n_y = 1.80$ as in the design of Fig. 5-2(a). The ambient refractive index is 1.37 which corresponds to an array of circular rods with radius $r = 0.33a$. This design was also verified with FDTD under TM plane wave

illumination. The results are shown in Fig. 5-7. A plane wave with little distortion at the output to the right of the cloak can be observed. Imperfections are mainly due to scattering at the sharp edges and reflections at the boundaries between the isotropic and anisotropic media. Since the reflection mainly occurs to the left of the parallelogram region, the overall wave profile is preserved to a large degree, with negligible energy loss. The amount of reflection at different cloaking angles (β) is plotted in Fig. 5-8. The reflection can be further suppressed by using anti–reflection techniques (see Section 5.4). Since the propagation of the wave avoids the parallelogram shape region in the photonic device, the mechanical components can be accommodated in a photonic waveguide directly while the performance is still preserved to a large extent. A mechanical connector can penetrate through this waveguide, connect with other parts of the device and stack a large number of layers of "photonic boards" analogous to "printed circuit board" (PCB). Alternatively, through this empty region, an optical fiber can deliver optical signals across this waveguide along the third dimension similar to the "jumper" in circuits. This application can be useful in future photonic industry, being able to provide more design flexibility in large scale photonic integration.

5.4 Gradient–index antireflection layers

We notice from the above results, especially Fig. 5-4 and Fig. 5-7, that there are reflections at isotropic/anisotropic interfaces due to impedance mismatch. While in many applications these reflections are negligible, in some cases they are intolerable and should be minimized. In this section we will discuss how to use gradually–varying layers to achieve impedance–matching.

Antireflection coatings by impedance matching are commonly used in optical devices. However, in real practice it is generally very challenging to impedance match two regions with high contrast of optical properties. Recently, with the rise of metamaterial research, there have been many studies on the use of anisotropic structures to manipulate the light propagation, especially at the nano–scale. This is one case

where the mismatch is particularly strong, since the boundary is often between an isotropic and an anisotropic material; perhaps for that reason, the topic of impedance matching has rarely been discussed thoroughly.

We propose impedance–matching gradually–varying layers at isotropic/anisotropic nanostructure boundaries to eliminate the reflection, and discuss the corresponding design considerations. In the scenario discussed in this chapter, increasing the number of antireflection layers, while decreasing the reflection, also degrades the performance of the device by introducing lateral shift. Therefore the number of layers should be chosen carefully to balance these two counter–acting effects. This antireflection layer design is also applicable to other index–mismatched nanostructured boundaries, or even the boundaries between nanostructures and a uniform medium [137]. In either case, one should always emphasize the balance between transmission efficiency and correct device performance.

Here we consider a boundary between isotropic and anisotropic periodic nanostructures in the photonic cloak discussed in Fig. 5-3 & Fig. 5-4.Due to the index–mismatch between isotropic region (circular rod arrays) and anisotropic region (elliptical rod arrays), reflection is prominent; hence, antireflection layers are needed.

The antireflection layer design we propose is illustrated in Fig. 5-9, where four layers are used as an example. Our design transformed the corresponding four elliptical rod layers into gradually–varying elliptical rod layers. Their sizes are chosen such that effective n_x is fixed at 1.30 but n_y changes at a linear increment of 0.10 from 1.30 to 1.80 for each antireflection layer from top to bottom. The reflection is greatly reduced, which is evident as highlighted with dashed circles in Fig. 5-10. The relationship between reflection coefficient and the number of gradient–index layers is shown in Fig. 5-11(a). It is observed that reflection can be further reduced by increasing the number of layers.

However, antireflection layers also bring undesirable side effects. These layers deviate the profile of the cloak, i.e. the effective refractive index distributions, from the desired original. Therefore, the beam no longer follows the desired trajectory but has a lateral shift at the output (see Fig. 5-10(b)), similar to the one described

in [147]. The lateral shift downgrades the performance of the photonic cloak, and as shown in Fig. 5-11(b), larger number of antireflection layers results in larger shift. Therefore, a trade–off always exists between the amount of reflection reduction and preservation of device functionality.

5.5 Conclusion

In this chapter, we presented the first practical design for integrating mechanical components into photonic devices. Elliptical rod arrays are used to realize anisotropic materials. These elliptical rods are actually a general form of binary gratings, which have been widely used to generate anisotropy (for example, see [144]). Designs that can be used for accommodating mechanical components from the periphery and inner region of a waveguide are designed and verified through the FDTD simulation. This design can be an extension and supplement of current photonic designs and provide more flexible design strategy for future photonic integration in a more compact form. Furthermore, discussions on using gradually–varying layers to minimize the unwanted reflection at interfaces and their influences on the cloaking performance have been presented.

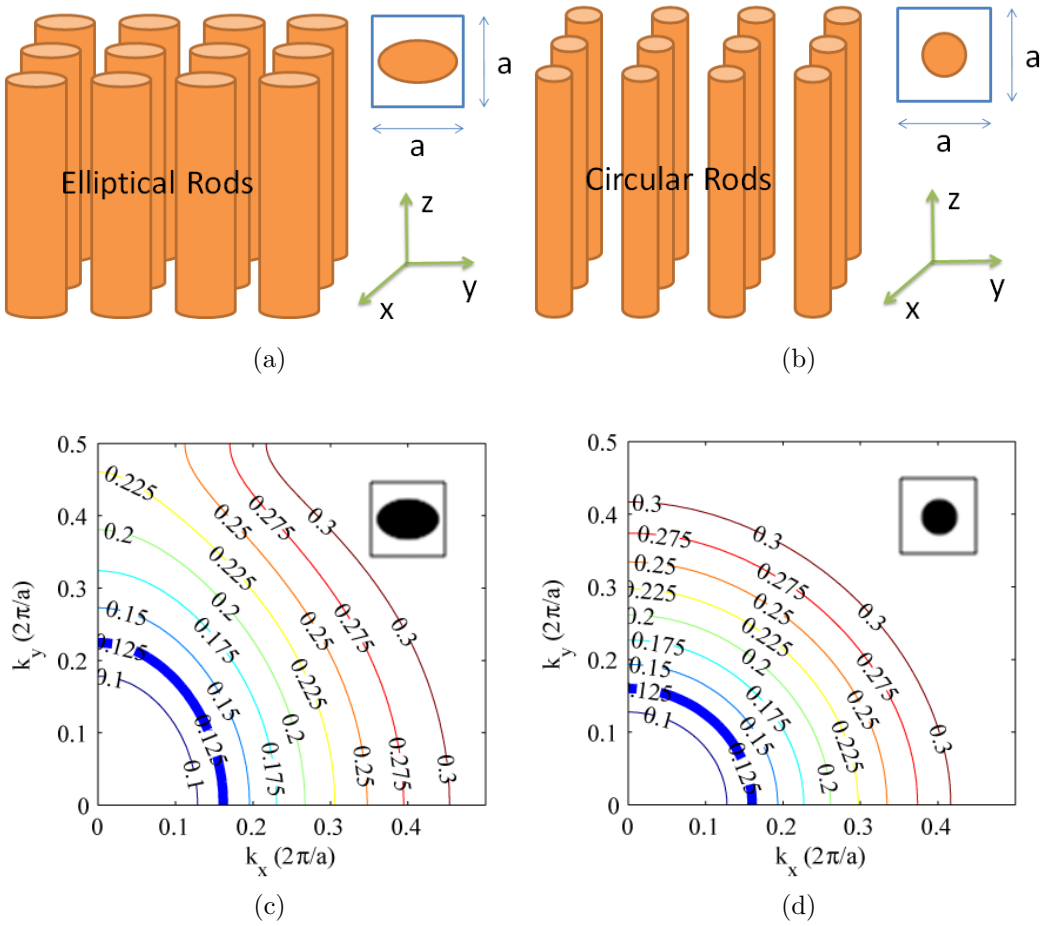

Figure 5-2: Elliptical (a) and circular (b) silicon rod lattice structure. Isofrequency diagrams of silicon elliptical (c) and circular (d) rod unit cells, where only the first TM band is shown. The size of the unit cell is $a \times a$. The long and short axes of the elliptical rod in (a) are $0.95a$ and $0.5a$, respectively; the radius of circular rod in (b) was chosen as $0.294a$ to match the effective index of the isotropic circular rod case with the effective value of the index along the x axis in the anisotropic elliptical rod case. Labels on the lines denote the corresponding normalized frequency $\omega a/2\pi c$. The bold blue lines correspond to the free space wavelength $\lambda = 8a$ used in this thesis.

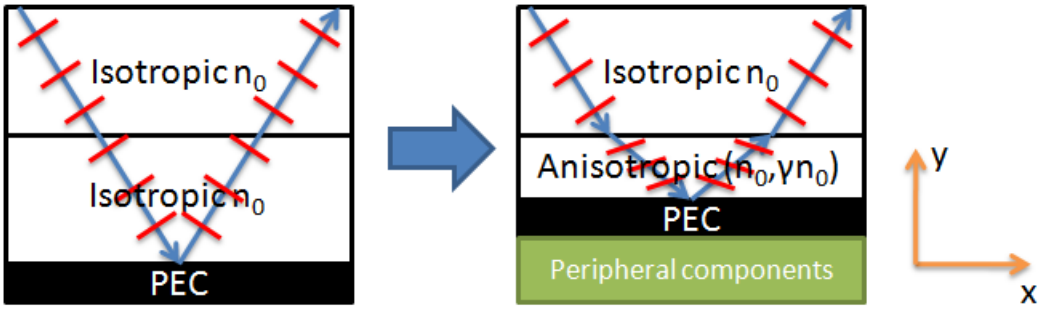

Figure 5-3: Space transformation of the first design example. More peripheral area (green) for accommodating mechanical components is created by squeezing the uniform medium into an anisotropic medium. Blue arrows are ray trajectories, and red lines illustrate wavefronts.

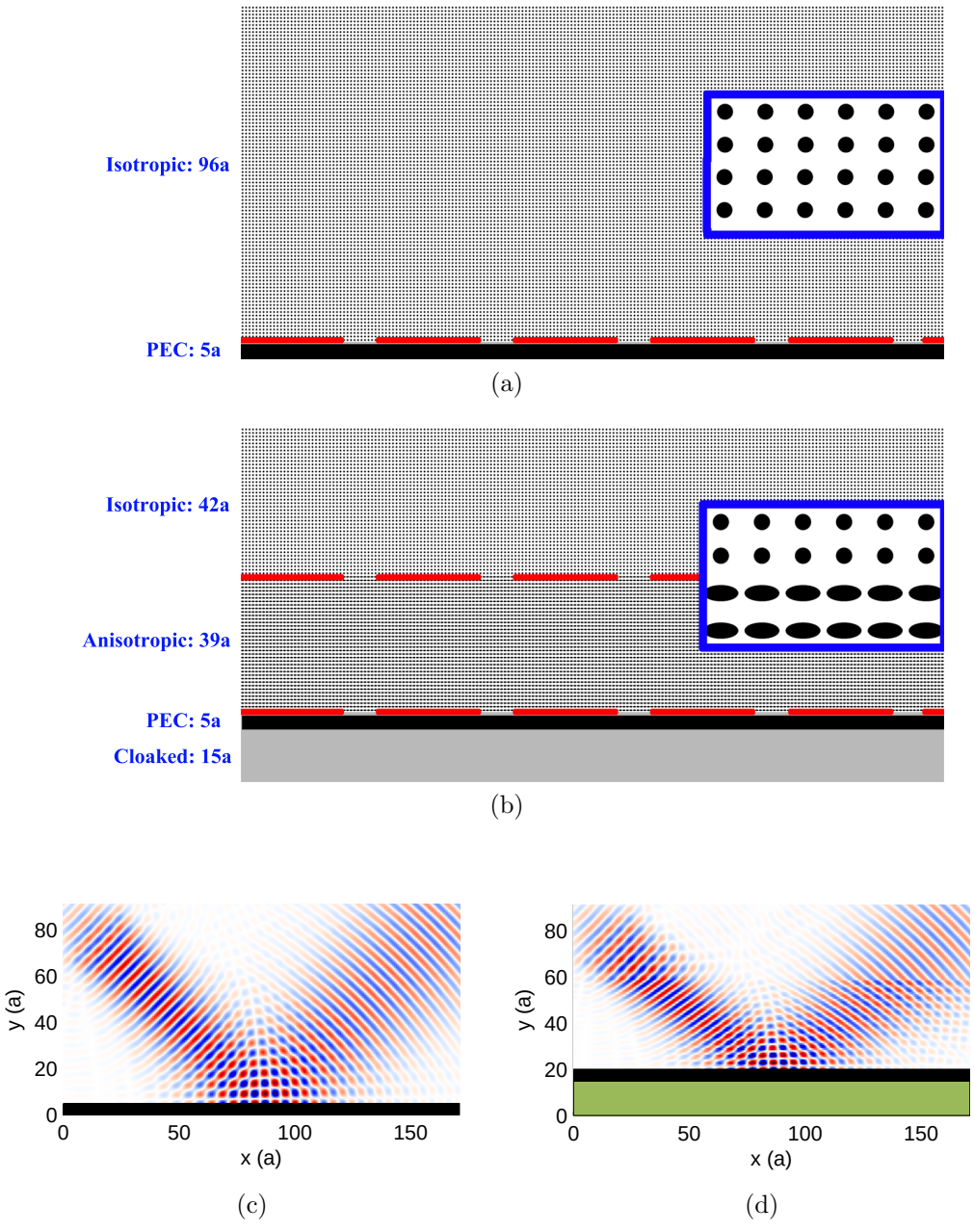

Figure 5-4: (a)(b) Original structure and the structure of the first design example. Blue boxes are the zoomed–in view of the lattices. Red lines denote the interfaces between different media: PEC, isotropic and anisotropic medium. (c)(d) FDTD results of original structure and accommodating design. Illumination is TM Gaussian source with incident angle of 45°. Black stripe is PEC and green stripe is area for accommodating mechanical components. Color shading denotes the magnetic field (H_z) distribution. Red is positive and blue is negative.

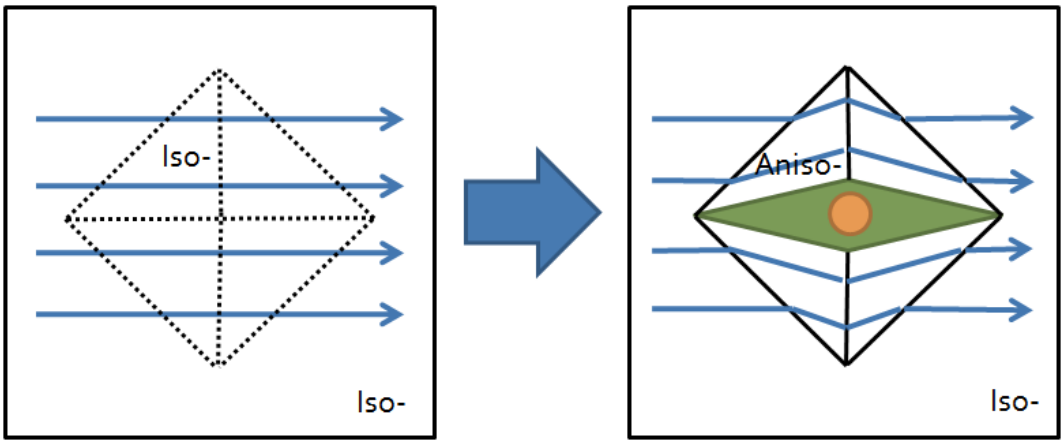

Figure 5-5: Transformation of space to create a parallelogram for accommodating internal mechanical components. Ray tracing results are illustrated. "Iso–" means isotropic and "Aniso–" means anisotropic.

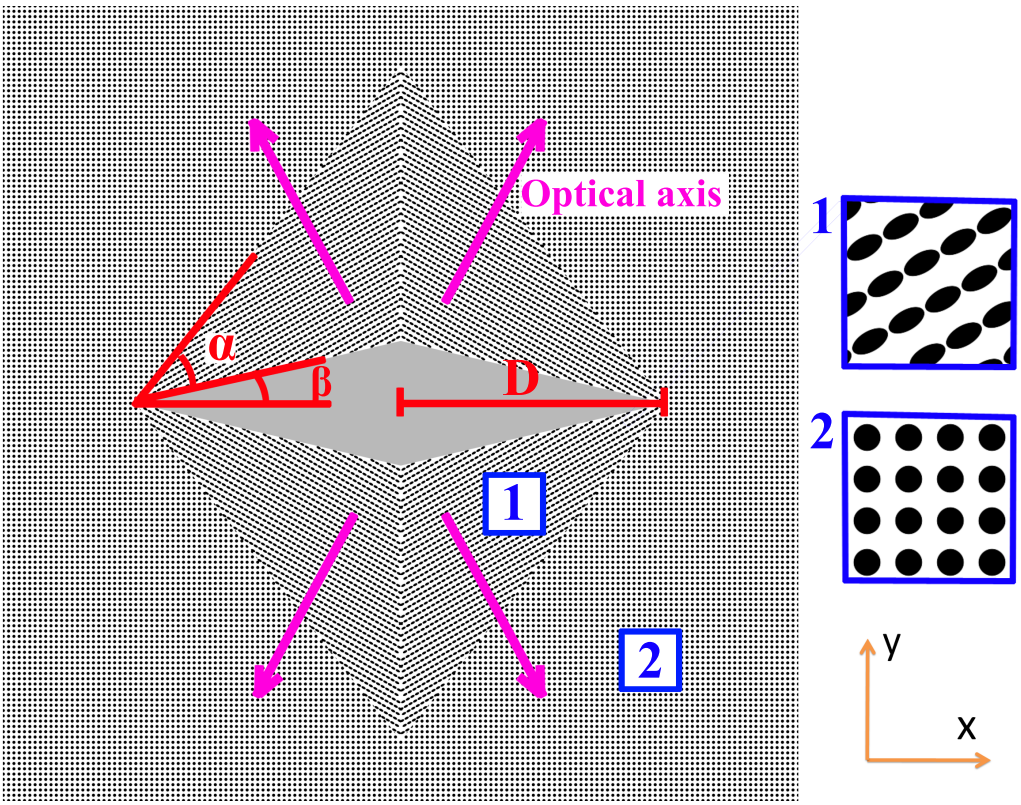

Figure 5-6: Structure of the second design example, composed of uniform elliptical and circular silicon rod arrays. Grey parallelogram in the middle is region for mechanical components and magenta arrows are the optical axes of the anisotropic media. The dimensions are $D = 50a = 6.25\lambda$, $\alpha = 38.5°$ and $\beta = 13.3°$. Note that this implementation is for proof–of–concept and is definitely scalable.

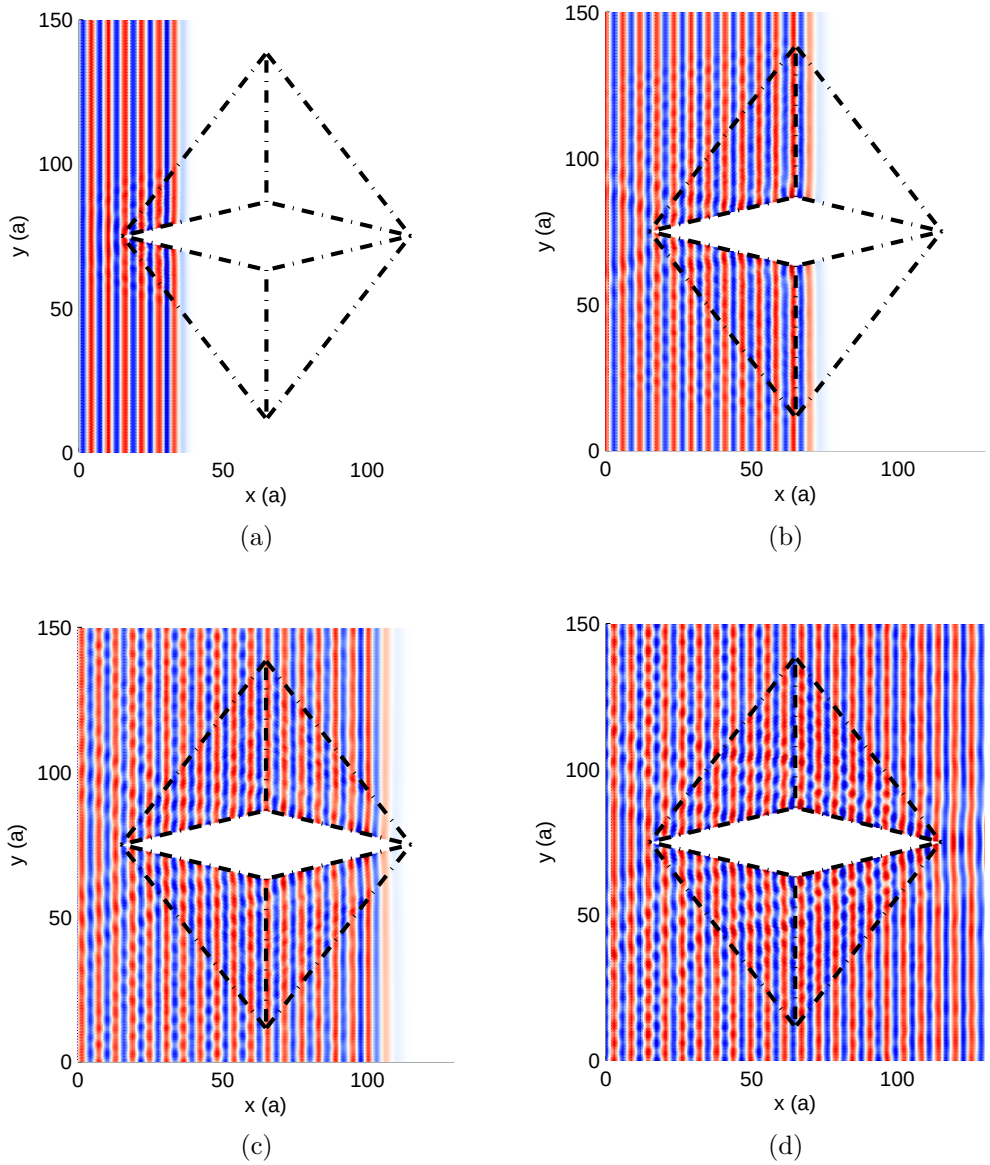

Figure 5-7: FDTD simulation results of this design illuminated by plane wave with $\lambda = 8a$ at time $t = 6.25\lambda/c$, $12.5\lambda/c$, $18.75\lambda/c$, $25\lambda/c$, respectively. Color shading denotes the magnetic field (H_z) distribution, where red is positive and blue is negative.

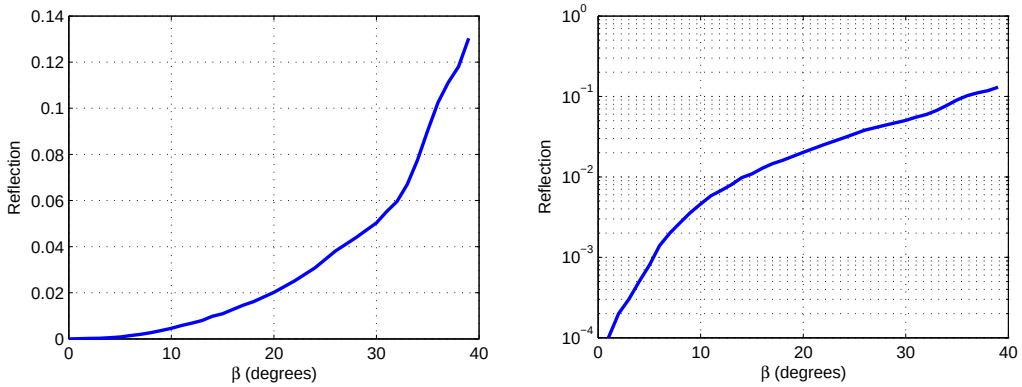

(a) (b)

Figure 5-8: Amount of reflection and scattering for diamond–shape cloak (Fig. 5-6) at different cloaking sizes (β angles) in (a) linear and (b) logarithmic scale.

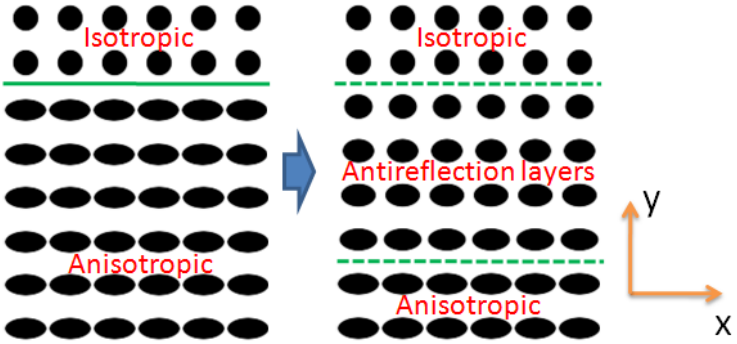

Figure 5-9: One example of gradient–index antireflection layers, where four layers are used.

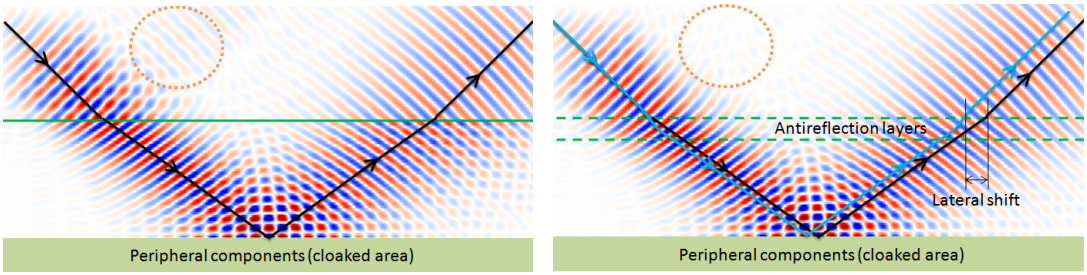

(a) (b)

Figure 5-10: FDTD simulation results and sampled ray tracing of the photonic cloak without (a) and with (b) gradient–index antireflection layers. Ray trajectories for (a) are duplicated (black arrows) in (b) as a comparison to the trajectories for (b) (light blue arrows), illustrating the resulting lateral shift. Green lines illustrates the boundary or antireflection layers between circular and elliptical rod lattices. Color shading denotes the magnetic field [H_z] distribution.

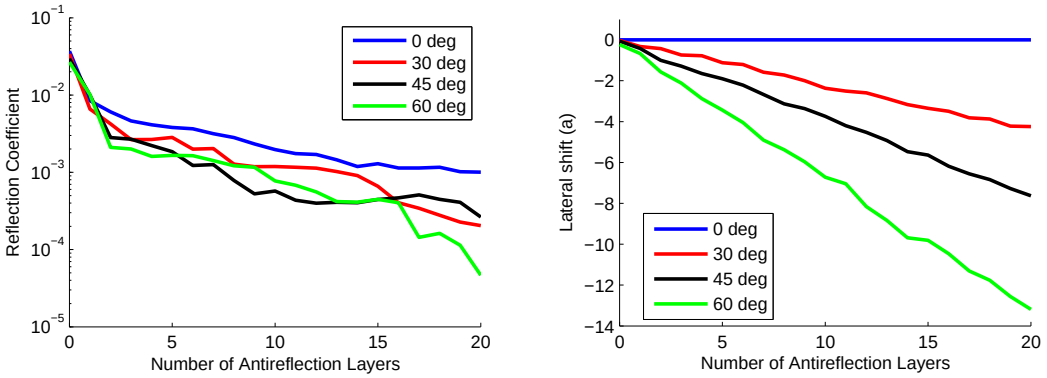

(a) (b)

Figure 5-11: Reflection coefficient (a) and lateral shift (b) with respect to the number of antireflection layers for different incident angles. Negative value for the lateral shift means a shift to negative–x direction from the correct position.

Chapter 6

Thin–film subwavelength Lüneburg lens

In previous chapter we discussed the realization of anisotropic media using subwavelength optical pupils. But the story of subwavelength elements is far from over. In this chapter, we will explore subwavelength structures' usage in realizing inhomogeneous media in the context of thin–film gradient index (GRIN) media.

GRIN media offer rich possibilities for light manipulation. In integrated optics applications, the required refractive index distribution can be emulated by patterning a substrate with subwavelength structures. By either tuning the size of each unit cell, or changing the size of the structure inside each unit cell, different effective indices can be realized. Currently the operating wavelength is significantly larger than the size of the unit cell so that these structures can be considered as effective media.

In most existing designs, refractive indices are computed using a 2D approximation, assuming that the height of the metamaterial in the third dimension is much larger than the wavelength. While in some cases this approximation is true, mostly such adiabatically variant structures are fabricated by etching holes or rods on a thin silicon film, where the height is actually even less than the optical wavelength [42, 131, 132, 137, 146]. Therefore the calculated effective indices based on 2D assumption are questionable. A 3D calculation approach is necessary. In this chapter, an analytical approach for calculating the effective indices of thin–film photonic

metamaterial devices is presented [57, 58, 59, 60].

In our group, we have designed and fabricated a subwavelength aperiodic nanostructured Lüneburg lens [131, 132]. In our fabricated Lüneburg lens design, thin–film problem is obvious where the experimental results show dislocated and aberrated focal point [131, 132]. Here we re–designed the Lüneburg lens to include the finite film thickness, improving the estimate of the expected focal point position. To design such a lens, first we need a method for estimating effective refractive index of thin–film metamaterials. Several methods have been proposed in the literature. A conventional numerical approach (we refer to it as Direct Band Diagram, DBD) in photonic crystals derives a 3D lattice cell from the original 2D cell by surrounding a finite–height rod with large spaces of air above and glass substrate below [78]. Another method takes one unit cell and retrieves the refractive index by its reflection and refraction properties [23]. These methods yield accurate results but require either 3D band or finite–difference calculations. More heuristic (but faster) effective–index methods estimate a slab–waveguide effective index first and then use it to compute a 2D band diagram or effective index [68]. These methods are generally suitable for structures with etched substrates. In contrast, our proposal essentially reverses the order of these steps: we compute an effective index from the 2D cross–section first, and then incorporate it into a slab–waveguide mode. Our method is more suitable to the metamaterial regime.

In particular, we propose the following all–analytical method for effective refractive index calculation. First, we replace the rods with a continuum of a certain effective permittivity $\epsilon_{\text{eff}}^{\text{2D}}$. We calculate $\epsilon_{\text{eff}}^{\text{2D}}$ from 2D lattice of infinite–height rods using second–order effective medium theory, and then substitute $\epsilon_{\text{eff}}^{\text{2D}}$ as the permittivity of a slab of finite thickness, acting as an effective guiding medium, sandwiched between semi–infinite spaces of air above and glass below. The geometry then becomes one of a weakly–guiding waveguide due to the small height of the effective guiding medium. This weakly–guiding effect modifies the real part of the horizontal wave–vector component, and thus a new effective permittivity $\epsilon_{\text{eff}}^{\text{3D}}$ for the finite slab of rods is derived from the waveguide dispersion relationship. We refer to this method

as Effective Guiding Medium (EGM). Comparing with rigorous 3D calculations, our method provides more physical insights, and is generally faster to compute.

To validate our method, we compare it with the DBD method. It is shown that the results of both methods are in good agreement.

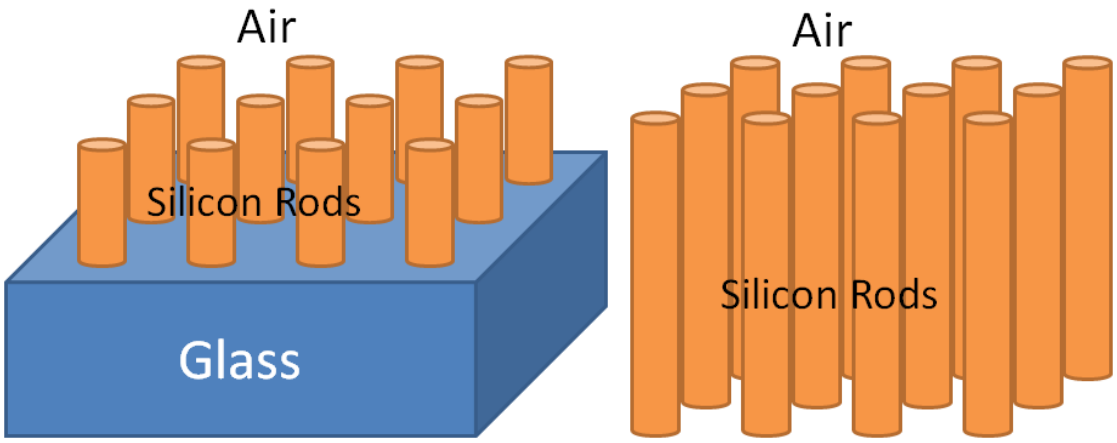

(a) (b)

Figure 6-1: (a) Finite height rod lattice structure. (b) 2D rod lattice structure assuming infinite height.

6.1 Analytical method for effective refractive index estimation

Without loss of generality, we investigate a silica glass slab covered by a square lattice (lattice constant $a = 258$ nm) of silicon rods of finite height $h = 320$ nm, variable radius r ($0 < r < a/\sqrt{2}$) and immersed in air, as illustrated in Fig. 6-1(a). The free space wavelength of light is chosen as $\lambda = 6a = 1550$ nm. This choice of a is small enough to insure that we remain in the metamaterial regime and in the propagating regime of the band diagram; and large enough that the rods can be accurately fabricated by nano–lithography [131, 132] and we do not reach the long–wavelength cutoff regime for the asymmetric waveguide. The dielectric permittivity constants for glass and silicon are $\epsilon_{\text{glass}} = 2.25$ and $\epsilon_{\text{silicon}} = 12.0$, respectively. These media are non–magnetic, so the relative permeability is taken as $\mu = 1$. The glass

slab height is assumed to be much larger than the height of the rods and the free space wavelength of the light. The corresponding 2D structure with infinite height rods and without glass substrate is shown in Fig. 6-1(b). We now proceed to describe all–analytical method, EGM, for analyzing these two geometries.

6.1.1 Effective guiding medium (EGM) method

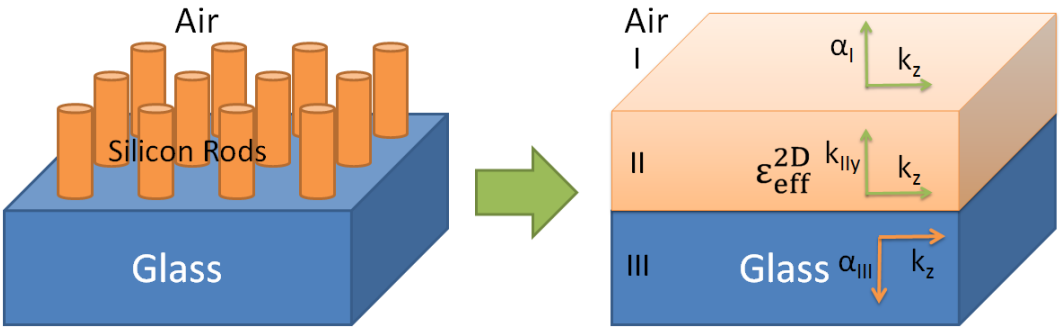

Figure 6-2: Effective guiding medium (EGM) approximation of 2D finite height rod lattice structure.

The EGM method requires analysis of a three–layer structure: (I) air, (II) effective medium waveguide and (III) glass, as shown in Fig. 6-2. The effective permittivity of the guiding medium is calculated from the second–order effective medium theory in 2D which have been derived by various authors [18, 116]. This theory starts from the effective refractive index of 1D subwavelength grating composed of air and dielectric with index n. Under TE (electric field parallel to the grating) and TM (electric field vertical to the grating) polarization incidence the effective index can be summarized, respectively, as [18, 145]

$$n_{\mathrm{TE}}^2 = n_{0\mathrm{TE}}^2 + \frac{\pi^2}{3}\left(\frac{T}{\lambda}\right)^2 f^2(1-f)^2(n^2-1)^2, \tag{6.1}$$

$$n_{\mathrm{TM}}^2 = n_{0\mathrm{TM}}^2 + \frac{\pi^2}{3}\left(\frac{T}{\lambda}\right)^2 f^2(1-f)^2 n_{0\mathrm{TM}}^6 n_{0\mathrm{TE}}^2\left(\frac{1}{n^2}-1\right)^2, \tag{6.2}$$

where

$$n_{0\mathrm{TE}}^2 = fn^2 + (1-f), \quad n_{0\mathrm{TM}}^2 = 1\Big/\left(\frac{f}{n^2} + (1-f)\right) \tag{6.3}$$

are the zeroth-order effective refractive indices, T is the period of the grating and f is the filling factor of the dielectric grooves. The effective indices of corresponding 2D subwavelength structures are then estimated as a combination of 1D structures [18, 145]

$$n_{\mathrm{2D-TE}} = \sqrt{1-f+fn_{\mathrm{TE}}^2}, \tag{6.4}$$

$$n_{\mathrm{2D-TM}} = \left(\sqrt{(1-f)+fn_{\mathrm{TM}}^2}+\sqrt{\frac{n_{\mathrm{TE}}^2}{n_{\mathrm{TE}}^2(1-f)+f}}\right)/2 \tag{6.5}$$

for both TE and TM polarizations. Note that TE and TM polarizations mentioned here are an approximation since the fields are not purely polarized in 3D structures. A more exact way to describe them is TE–like/TM–like, where electrical field is mostly parallel/vertical to the grooves [78]. However, this notation is still an approximation because the waveguide is asymmetric so there is no horizontal mirror symmetric plane. The second–order terms used in Eq. (6.1) and (6.2) better approximate the effective index in the case that the wavelength is not very large comparing with size of unit cell, e.g. $\lambda = 6a$ used in this thesis. Most current metamaterial device designs are using the zeroth–order approximation only [137], even when the unit cell size is not far smaller than the operational wavelength. This approach is fine for those devices where high accuracy results are not important. However, for devices such as Lüneburg lens, all waves are focusing to a single point so light manipulation is more challenging. Therefore, more precise effective index prediction is needed and second–order corrections are included.

The dispersion relation of the effective guiding medium, i.e. the relationship between k_z and ω, is governed by the guidance condition of an asymmetric dielectric waveguide for both TE and TM polarizations [84]

$$\begin{aligned}(\mathrm{TE}:)\ \tan(k_{\mathrm{II}y}h) &= \frac{\epsilon_{\mathrm{II}}k_{\mathrm{II}y}(\epsilon_{\mathrm{III}}\sqrt{k_z^2-\epsilon_{\mathrm{I}}\omega^2/c^2}+\epsilon_{\mathrm{I}}\sqrt{k_z^2-\epsilon_{\mathrm{III}}\omega^2/c^2})}{\epsilon_{\mathrm{I}}\epsilon_{\mathrm{III}}k_{\mathrm{II}y}^2-\epsilon_{\mathrm{II}}^2\sqrt{k_z^2-\epsilon_{\mathrm{I}}\omega^2/c^2}\sqrt{k_z^2-\epsilon_{\mathrm{III}}\omega^2/c^2}} \\ &\equiv F_{\mathrm{TE}}(k_{\mathrm{II}y}h),\end{aligned} \tag{6.6}$$

$$(\text{TM}:)\ \tan(k_{\text{II}y}h) = \frac{k_{\text{II}y}(\sqrt{k_z^2-\epsilon_{\text{I}}\omega^2/c^2}+\sqrt{k_z^2-\epsilon_{\text{III}}\omega^2/c^2})}{k_{\text{II}y}^2-\sqrt{k_z^2-\epsilon_{\text{I}}\omega^2/c^2}\sqrt{k_z^2-\epsilon_{\text{III}}\omega^2/c^2}} \equiv F_{\text{TM}}(k_{\text{II}y}h), \quad (6.7)$$

where $k_z = \sqrt{\epsilon_{\text{II}}\omega^2/c^2 - k_{\text{II}y}^2}$ is the phase–matched propagation constant. These equations can be solved by a graphical method and an example is illustrated in Fig. 6-3. It is observed that one and only one intersection is obtained for each frequency, meaning that only one fundamental mode is supported. Full dispersion relations $k_z(\omega)$ are shown in the following section.

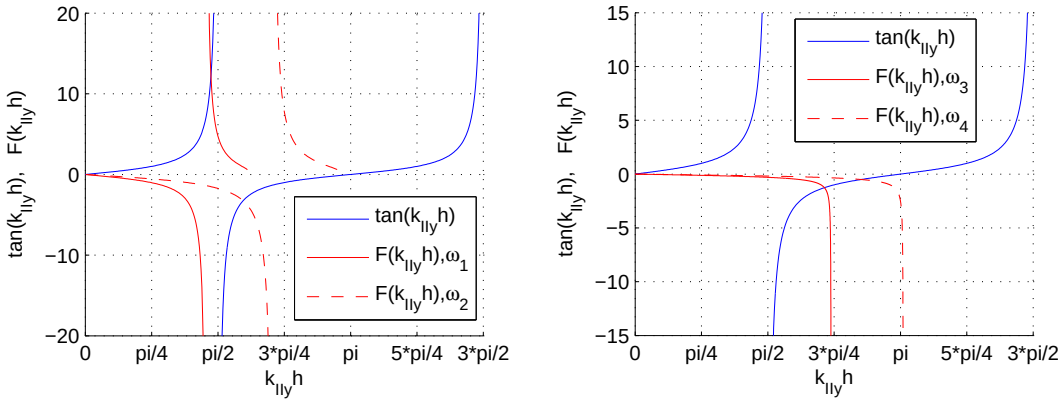

(a) (b)

Figure 6-3: Graphical solutions of wave guidance condition [Eq. (6.6) and (6.7)] for TE (a) and TM (b) polarizations. Blue and red lines are the left and right hand sides of these equations, respectively. Operating frequencies $\omega_1 = 0.11 \times 2\pi c/a$, $\omega_2 = 0.16 \times 2\pi c/a$, $\omega_3 = 0.14 \times 2\pi c/a$ and $\omega_4 = 0.18 \times 2\pi c/a$. Rod radius $r = 0.50a$.

The EGM method described above is compared with the conventional DBD method. To apply the DBD method, we need to calculate the band diagram of the 3D super cell shown in Fig. 6-4(a). The supercell height is taken as large as $H = 20a$ to better emulate the real structure of Fig. 6-1(a), where the air and glass spaces tend to infinity. In other words, we seek to minimize the interference between neighboring unit cells along the vertical (y) direction. We used the MIT Photonic–Bands (MPB) mode solver [80] to calculate the dispersion diagram. In Fig. 6-4(b–c) we show an example MPB result for our chosen lattice and the specific value $r = 0.5a$, for temporal frequency $\omega = 1/6 \times 2\pi c/a$. From Fig. 6-4(b) we observe that for the chosen values of

r and ω, the isofrequency contour [78] is almost a circle, indicating that this unit cell is isotropic. Therefore, when using DBD in this particular geometry, it is sufficient to consider $k_z(\omega)$ only. However, this is not generally true in other geometries as r or ω increase.

Figure 6-4(c) shows the mode shape for the same geometry. It can be seen that the field is effectively concentrated near the silicon rod portion of the cell. The relative intensities at two horizontal cell boundaries $y = \pm H/2$ were 5.6×10^{-6} and 3.8×10^{-6} at the top and bottom, respectively, compared to the peak value that occurred at $y = 159$ nm from the rod base. This validates our choice of H as sufficiently large.

Comparing with the DBD method, the EGM method can provide deeper physical insights with all–analytical solutions, and is generally faster since it avoids solving numerical electromagnetic solutions in 3D.

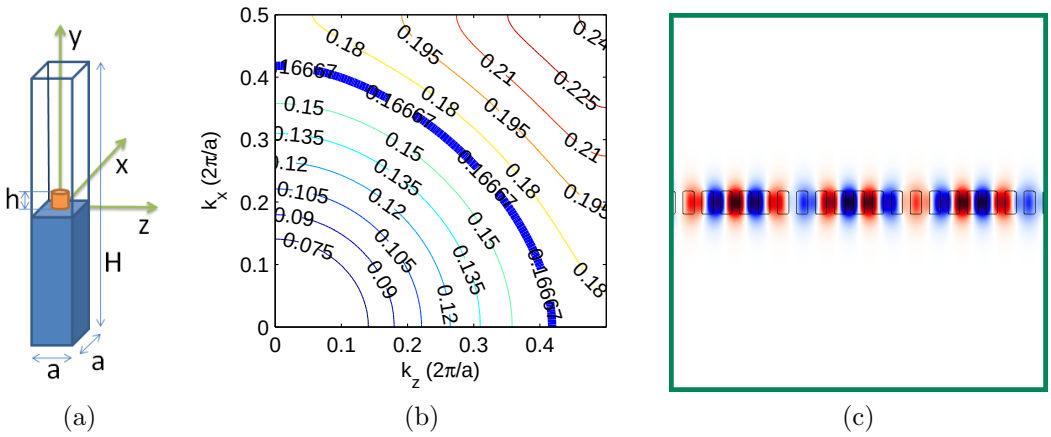

(a) (b) (c)

Figure 6-4: (a) The supercell used in the DBD method for the finite height rod lattice structure. (b) Isofrequency contour of the supercell with $r = 0.50a$ where the first band only is shown. Labels on the lines denote the corresponding normalized frequency $\omega a/2\pi c$. The bold blue line corresponds to the wavelength $\lambda = 6a$ used in this chapter. (c) Field distribution of the waveguide slab at a particular x slice. Color shading denotes magnetic field (H_y) distribution and black contours illustrate silicon rods.

6.1.2 Relationship between effective refractive index and rod radius

In this section, the relationship between the effective refractive index and rod radius is calculated. The results of EGM method are compared with the ones obtained from DBD method.

Figure 6-5(a) shows the dispersion relation of the finite–height rod lattice calculated with both DBD and EGM methods, as well as with the 2D (infinite rod height) assumption, for rod radius $r = 0.5a$. Based on the dispersion relation, effective refractive indices for unit cells with different rod radii are calculated as $n_{\text{eff}} = ck_z/\omega$, shown in Fig. 6-5(b). The results given by the DBD and EGM methods are in good agreement with each other, with maximum percentage errors of 7.3% and 6.0% for 2D and 3D cases, respectively. It is observed that the effective refractive indices of the finite–height rods are significantly different than those assuming infinite height. This is to be expected due to weak guidance: as can been seen in Fig. 6-4(c), a large portion of the field extends outside the rods to spaces of air and substrate. When the rod radii are below certain values ($0.17a$ for TE and $0.35a$ for TM), the propagation modes are not guided so the effective indices are not shown. The discontinuities observed in the 2D effective index curves for DBD method beyond certain values of rod radii ($0.40a$ for TE and $0.49a$ for TM) result from the emergence of a photonic crystal bandgap at these values. At this frequency range, even though the 2D infinite–height lattice is within the bandgap, the confined (slab waveguide) geometry is still propagating; this is because the light is mostly outside the dielectric region, so propagation takes place in the free space (hence the lower index). To calculate the propagation constant in this regime, we still need an effective index value and EGM provides it (it turns out to be large than 3, typically).

To further illustrate the influence of the height of rod lattice, calculated refractive indices corresponding to different thin–film height values are plotted in Fig. 6-6. Different polarizations and rod radii have been explored. It can be clearly observed that the effective refractive index of a thin–film is significantly different than the index

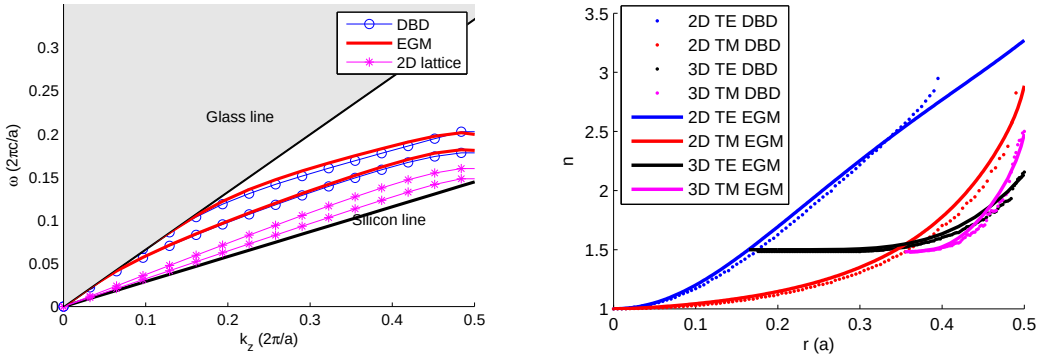

(a) (b)

Figure 6-5: (a) Comparison between the dispersion relation for finite–height silicon rod lattice [Fig. 6-1(a)] calculated from the EGM and DBD method, and the dispersion relation for infinite–height 2D rod lattice [Fig. 6-1(b)]. For each case, the two lowest bands representing the TM and TE modes are shown. (b) Relationship between effective refractive index and rod radius calculated from both methods, compared with the relationship for infinite–height 2D rod lattice. Free space wavelength of light is $\lambda = 6a = 1550$ nm.

of 2D assumption. With increasing rod height, the effective index converges into the the value under 2D assumption. Note that for large enough rods, the effective index does not exist for heights larger than certain value. This is an indication of reaching the photonic crystal bandgap.

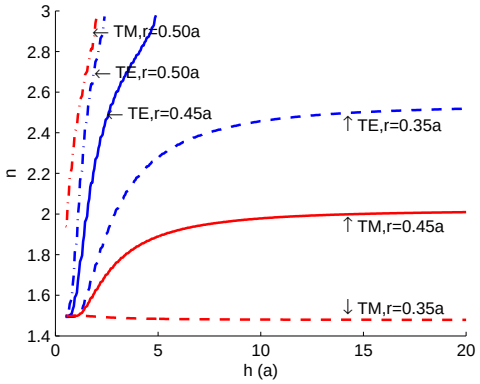

Figure 6-6: Relationship between calculated effective refractive index and height of the thin–film, at different polarizations and rod radii.

6.2 Corrected design of the subwavelength Lüneburg lens

We re–design and numerically verify the subwavelength Lüneburg lens [48, 95, 131, 132], which was previously designed under 2D assumption. Here, we still design the Lüneburg lens as a structure consisting of finite–height rods with adiabatically changing radius r across the lattice of fixed constant a. At each coordinate ρ, we emulate the Lüneburg distribution $n(\rho) = n_0\sqrt{2-(\rho/R)^2}$ by choosing the rod radius r at coordinate ρ from Fig. 6-5(b) such that $n_{\text{eff}}^{\text{3D}} = n(\rho)$, as opposed to using $n_{\text{eff}}^{\text{2D}} = n(\rho)$. The design has to be carried out separately for the TE and TM polarizations. The ambient index is chosen as $n_0 = 1.53$.

Figure 6-7 illustrates the lens structures and the corresponding 3D finite–difference time–domain (FDTD) simulation results for the actual adiabatically variant thin–film nanostructured Lüneburg lens performed by MIT Electromagnetic Equation Propagation (MEEP) [105]. The 3D model used for FDTD consists of a rectangular box of size $41a \times 24a \times 41a$ which contains perfectly matched layers on both sides of each dimension. The radius of the lens is chosen as $15a$. With plane wave illumination, almost diffraction–limited focal points at the edge can be observed for both TE and TM polarizations. For a more computationally efficient and intuitive representation we also ray–traced the field inside the Lüneburg structure using the adiabatic Hamiltonian method [49, 50, 51, 52, 73, 77, 114]. The ray position $\mathbf{q}$ and momentum $\mathbf{p}$ are obtained by solving the two sets of coupled ordinary differential equations

$$\frac{d\mathbf{q}}{d\sigma} = \frac{\partial H}{\partial \mathbf{p}}, \quad \frac{d\mathbf{p}}{d\sigma} = -\frac{\partial H}{\partial \mathbf{q}}, \tag{6.8}$$

where $H(\mathbf{q},\mathbf{p}) \equiv \omega(\rho,\mathbf{k})$ is obtained from the dispersion diagram at each coordinate $|\mathbf{q}| = \rho$ and for $\mathbf{k} \equiv \mathbf{p}$. Ray tracing results are superimposed in Fig. 6-7 with FDTD results, and are seen to be in good agreement. Furthermore, as a comparison, similar thin–film Lüneburg lens is designed using the DBD method and simulation results are shown in Fig. 6-8. It is observed that results of the all–analytical EGM method

design agree with those from the DBD method.

In Section 6.1.1 we mentioned the second–order effective medium theory for better approximation of the effective index when the wavelength is not significantly larger than the size of unit cell. To illustrate the importance of these second–order terms, we designed a thin–film Lüneburg lens using the EGM method, but the second–order terms were neglected when estimating the effective indices. The FDTD and ray–tracing results are shown in Fig. 6-9. The performance of the lens is degraded with aberrations and shifted focal position. Note that to clearly illustrate the focal points, we extended the size of the 3D FDTD model in z direction to $61a$.

To compare the redesigned lens (3D, finite height) with the original design (2D, infinite height), we repeated the design using the values of refractive indices predicted by the dispersion relation of the infinite–height rod lattice (see Fig. 6-5(b) blue and red solid curves). In this case, we are forced to use TM polarization only because the TE polarization reaches the bandgap for relatively small value of r, not leaving enough room to implement the Lüneburg profile with rod radius r large enough to be robust to practical lithography and etching methods (in our experiment, this requires $r \geq 0.27a$ [131, 132]). Also, for better illustration, the size of 3D FDTD model is modified to $41a \times 24a \times 101a$. It can be observed from the FDTD and Hamiltonian ray–tracing results shown in Fig. 6-10 that the focal point is outside the lens edge and it is strongly aberrated. This is in good agreement with the experimental results of the original design [131, 132].

6.3 Anisotropic guidance correction

The analytical method discussed above assumes that the thin–film layer can be approximated by an *isotropic* effective medium. However, in some cases this layer may be *anisotropic*. Anisotropic guidance correction is necessary when more precise design is required.

Fig. 6-11 illustrates the directions of E and H fields while the wave is propagating through the slab. Note that because all materials considered here are dielectric and

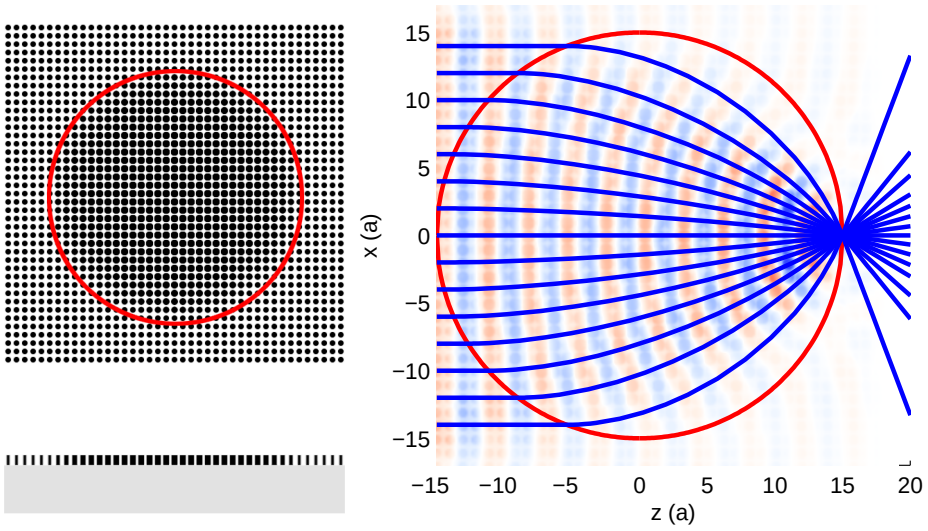

(a) (b)

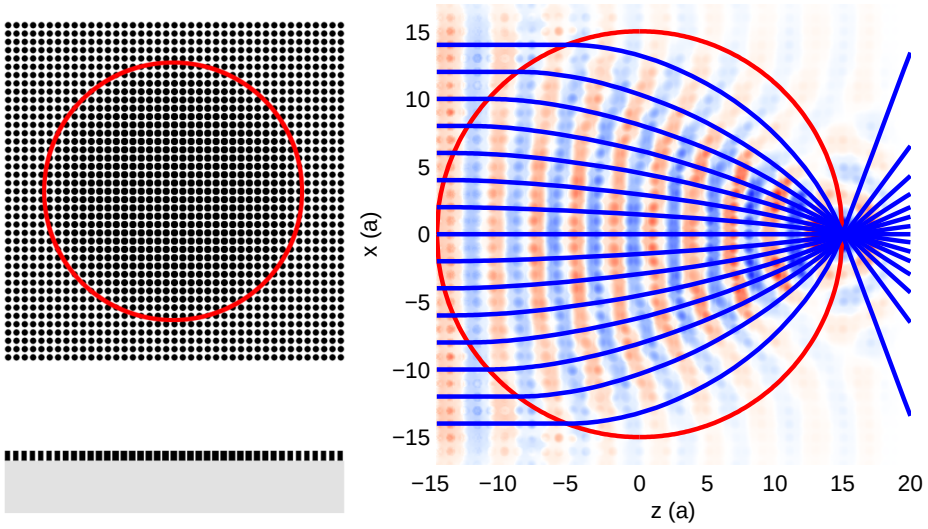

(c) (d)

Figure 6-7: (a) Top view and side view of the thin–film subwavelength Lüneburg lens designed by EGM method for TE mode and (b) the corresponding 3D FDTD and Hamiltonian ray tracing results. (c) Top view and side view for TM mode and (d) the corresponding 3D FDTD and ray tracing results. Red circles outline the edge of Lüneburg lens, where radius $R = 30a$. Blue lines are the ray tracing results and color shading denotes the field [H_y for (b) and E_y for (d)] distribution, where red is positive and blue is negative.

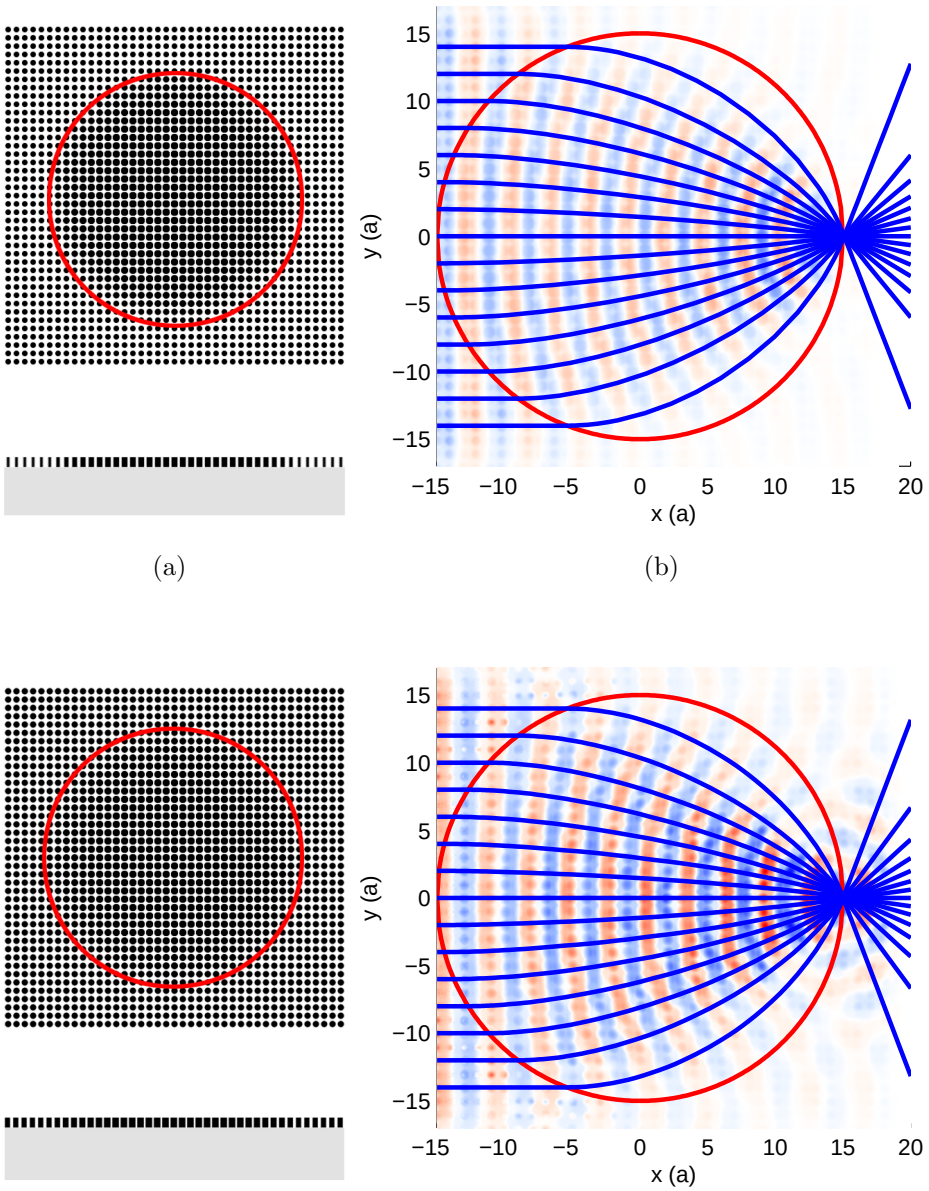

(a) (b)

(c) (d)

Figure 6-8: Structure and the corresponding 3D FDTD and Hamiltonian ray tracing for the thin–film subwavelength Lüneburg lens shown in Fig. 6-7, but designed by the DBD method instead.

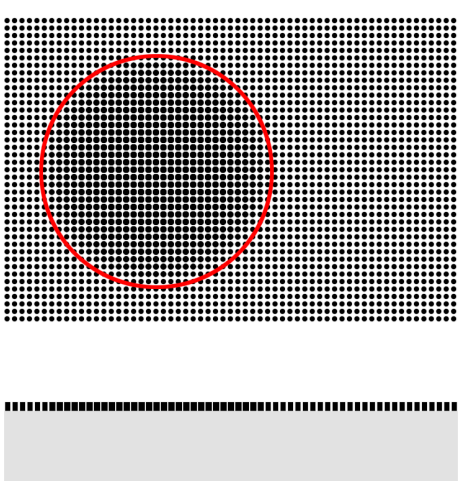

(a)

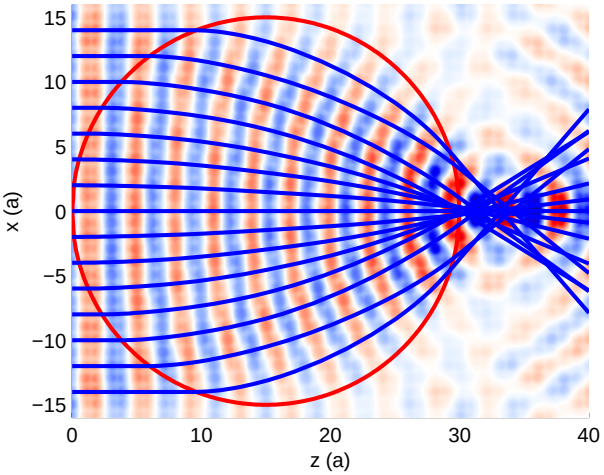

(b)

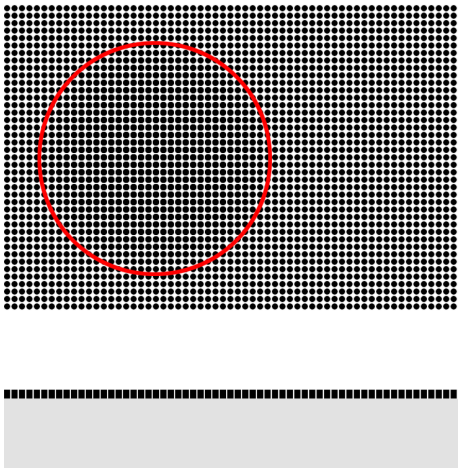

(c)

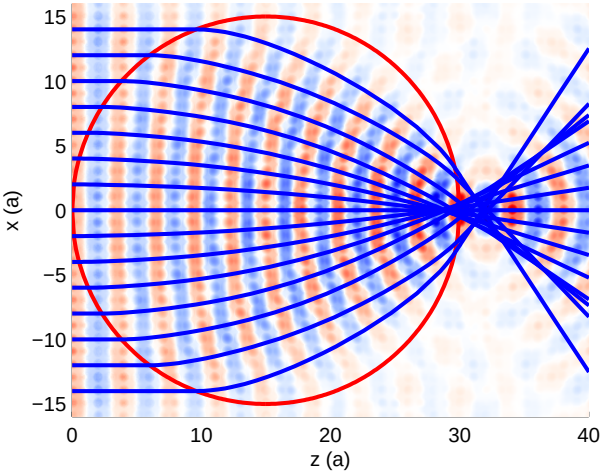

(d)

Figure 6-9: Structure and the corresponding 3D FDTD and Hamiltonian ray tracing for the thin–film subwavelength Lüneburg lens shown in Fig. 6-7, but designed using the EGM method without second–order terms when estimating the effective refractive indices.

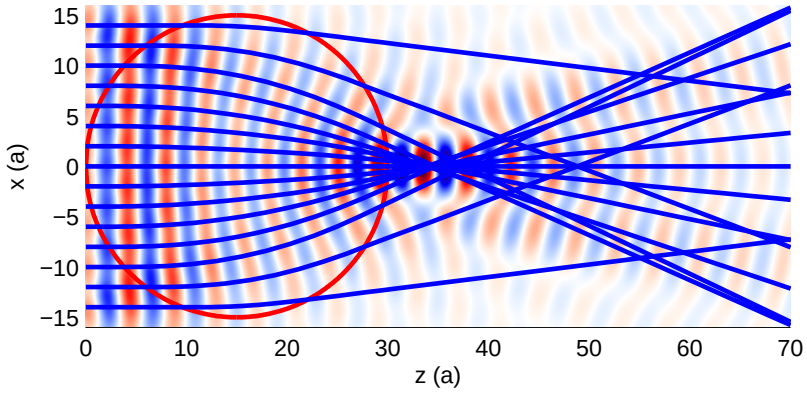

Figure 6-10: FDTD and Hamiltonian ray–tracing results of the subwavelength Lüneburg lens made of finite height silicon rods, but designed assuming infinite height. The color conventions are the same as in Fig. 6-7(b&d).

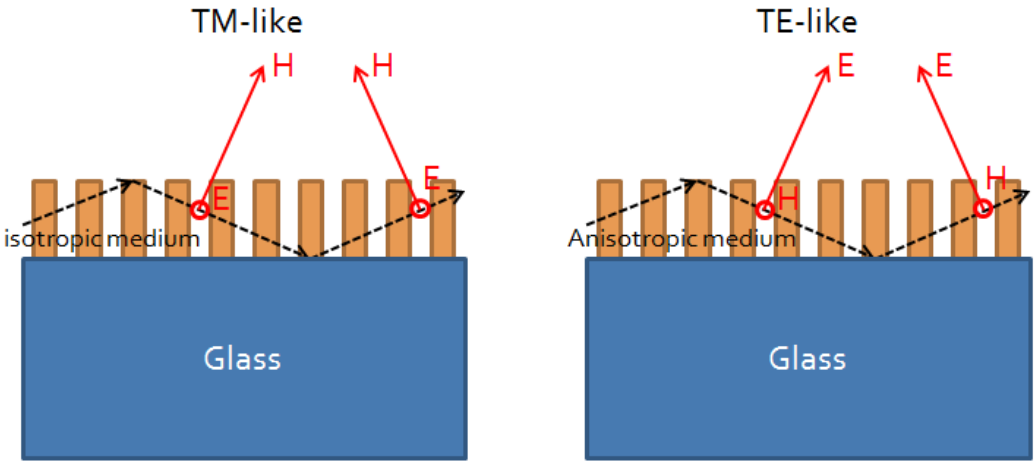

Figure 6-11: Polarization of electrical and magnetic fields while propagating along the thin–film under (left) TM–like and (right) TE–like polarizations. TE–like polarization results into an anisotropic effective medium.

non–magnetic, the polarization of magnetic field H does not matter. However, E field directions play an important role. Under TM–like polarization, E is always parallel to thin film; thus this slab can be considered isotropic. However, under TE–like polarization, because waves are bouncing back–and–forth between the two waveguide interfaces, E field is not perfectly perpendicular to the slab (that is also why this mode should be called TE–like instead of TE, to be more precise), but is tilted. E field contains two components: one is perpendicular to the slab and the other is parallel to it. These two components "see" different effective indices because they are orientated at different directions. One is parallel to the rods, while the other is vertical to them. The parallel component of E field (in x–z plane) is the same to the TM–like polarization case, which contributes to an effective permittivity along y direction; and the perpendicular component (along y direction) contributes to an effective permittivity along z direction (assuming waves are propagating along z direction).

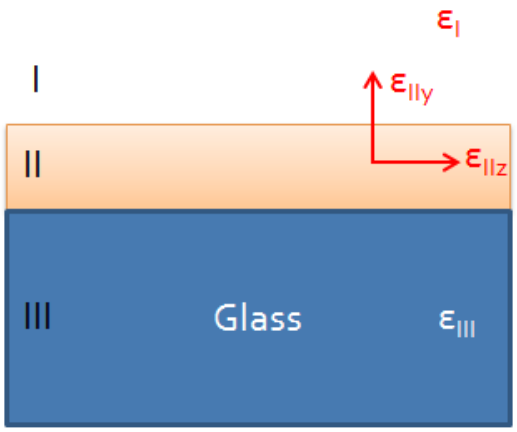

Figure 6-12: Three–layer effective structure for a thin–film slab under TE–like polarization. The middle layer now becomes anisotropic effectively.

Therefore, the thin–film layer is actually anisotropic and can be modeled by an effective anisotropic medium illustrated in Fig. 6-12. It is a uniaxial birefringent layer with optical axis perpendicular to the interface. Note that $\epsilon_{\mathrm{II}y}$ is equivalent to the effective index of an isotropic medium of TM–like polarization. We re–write the guidance condition under TE polarization assuming isotropic effective medium here

(see also Eq. 6.6)

$$\arctan\left(\frac{\epsilon_{\text{II}}\sqrt{k_z^2-\epsilon_{\text{I}}\omega^2/c^2}}{\epsilon_{\text{I}}k_{\text{II}y}}\right)+\arctan\left(\frac{\epsilon_{\text{II}}\sqrt{k_z^2-\epsilon_{\text{III}}\omega^2/c^2}}{\epsilon_{\text{III}}k_{\text{II}y}}\right)=k_{\text{II}y}\cdot h+m\pi, \quad (6.9)$$

where m is an integer. After some calculation, the guidance condition assuming an anisotropic effective medium can be written as

$$\arctan\left(\frac{\epsilon_{\text{II}z}\sqrt{k_z^2-\epsilon_{\text{I}}\omega^2/c^2}}{\epsilon_{\text{I}}k_{\text{II}y}}\right)+\arctan\left(\frac{\epsilon_{\text{II}z}\sqrt{k_z^2-\epsilon_{\text{III}}\omega^2/c^2}}{\epsilon_{\text{III}}k_{\text{II}y}}\right)=k_{\text{II}y}\cdot h+m\pi, \quad (6.10)$$

where m is an integer as well. The only difference is that we are using $\epsilon_{\text{II}z}$ for the effective permittivity of the slab layer, instead of using ϵ_{II} which equals to $\epsilon_{\text{II}y}$. Thin–film subwavelength nanostructured devices can be designed more precisely when taking the above anisotropic effect into consideration.

6.4 Conclusion

In this chapter, we designed an all–dielectric finite–thickness aperiodic nanostructured Lüneburg lens. In order to compensate for the thin–film effect, an all–analytical approach is proposed. Our method estimates the effective refractive index of the infinite–height lattice from the second–order effective medium theory, then we replace this lattice with a continuum medium of the same effective index. In this way the structure becomes one of the asymmetric waveguide, and a new effective index explicitly accounting for the thin–film effect can be derived from the waveguide dispersion relation. The results agree with those calculated using the conventional numerical treatment; but our method avoids 3D numerical calculation and provides more physical intuition. The performance of the Lüneburg lens has been verified with 3D finite–difference time–domain (FDTD) method. In the end the effect of anisotropic effective medium has been discussed.

THIS PAGE INTENTIONALLY LEFT BLANK

Chapter 7

Conclusions and future work

In this thesis, we explored various designs and applications of three dimensional pupils. Three different categories of pupils have been discussed, including:

- 3D diffractive pupils where shift variance is desirable, enabling the favorable property of depth selectivity. In Chapter 2, a volume holographic filter architecture for detecting artificial satellites in daytime has been proposed and optimized. This design is verified by a tabletop experiment. Effects of field of view, atmospheric turbulence and lens aberrations on this design have been evaluated.

- 3D diffractive pupils where shift variance and PSF manipulation are both desirable. Manipulation can be achieved by deforming the pupils, i.e. holograms. In Chapter 3 and Chapter 4, both point indenters and bulk transformations have been investigated. Especially for bulk transformations, we aim at locating analytical expressions, which are physically intuitive and computationally efficient.

- Subwavelength structures where the PSF needs to be manipulated. This manipulation is mostly realized by designing inhomogeneous and anisotropic refractive index or permittivity distributions. In Chapter 5 and Chapter 6, we explored the possibilities of fine tuning each unit cell to achieve gradient index and anisotropic materials. Three dimensional thin film effect has also been

emphasized, which are the steps towards full three dimensional pupils.

Three dimensional diffractive pupils such as volume holograms do not have to be used for detecting artificial satellites in the case of long distance imaging. While, up to now, most volume holographic imaging applications aim towards microscopy, or objects located at a short distance away. We have demonstrated in this thesis that depth selectivity can be equally applied to long–distance imaging. Our tabletop experiment implemented a prototype for this purpose. Potential applications to be explored in the future include imaging underwater through a turbulence, locating live objects through thick smoke in a fire, and all other cases where noise dominates and a significant SNR enhancement is desired. In addition, this VHF system is definitely multifunctional, and *in vivo* adjustment of this system is also available. Once this system has been built, changing the system for imaging at a different distance (depth) can be easily realized by tuning the relative distance between the two lenses of the telephoto system. Furthermore, because of the wavelength degeneracy of volume holograms, this type of 3D pupils can also be tuned to function at different wavelengths, including at least infrared and ultraviolet.

Besides shift variance, deforming the exterior of 3D pupils provides richer design opportunities through the manipulation of PSFs. We have investigated the deformations from point indenters and bulk transformations. In the future, these deformed 3D pupils can be realized in experiment. First we define the PSFs required for different imaging purposes, such as a narrow mainlobe PSF, a suppressed sidelobe PSF, or even a rotating PSF. In the next step, a proper deformation is calculated using optimization approach. The analytical relationship investigated in Chapter 4 could facilitate this process. Once the deformations for desired PSFs are found, experiments may be performed to utilize this deformed 3D pupil. This experiment prototype can be applied to various applications, e.g. biological imaging. Changing the transformations exerted on the hologram allows for a switching of PSFs. Thus an object could be probed through different systems using just one architecture.

It is also beneficial to explore larger deformations, where the material of the pupils not only redistributes, but also becomes, for example, anisotropic. The effect

of anisotropy should be considered in deriving the analytical deformation–PSF relationship. Material anisotropy makes this problem more difficult, but on the other hand it also provides possibilities of more potentially interesting properties and phenomena. For dealing with anisotropy, it is helpful to make an analogy between this diffractive regime with subwavelength regime, where anisotropy has been discussed and considered as a standard tool.

As has been discussed, the deformation is applied upon an already recorded pattern of plane–wave interference, thus design flexibility is limited. To create more complex patterns, a phase or amplitude mask could be placed in one or both of the recording beams; this could potentially record arbitrary permittivity patterns on the hologram. Resulting recorded pattern manipulates the PSF in combination with the deformations. Note that due to the diffraction limit, this pattern is limited to the diffractive regime, unless the hologram is used at longer (infrared) wavelengths.

In subwavelength regime, there are also various directions for exploration. Now that inhomogeneity [60, 131] and anisotropy [143, 148], have been realized, many complex subwavelength optical elements can be designed in a similar manner, especially those for integrated optical systems and future "optical circuits", including modulators, waveguides, couplers, collimators, and even nanostructured optical sources and detectors. Three dimensional device designs are readily available, since our approach can be easily extended to the third dimension. The current major obstruction in developing 3D devices is the limited 3D fabrication methods available, not the design itself.

Three dimensional subwavelength devices should be inserted into the pupil plane of an optical system in order to achieve the desired PSF or relevant optical functionality. Note that the (almost) free modulation of "effective" material properties in these subwavelength devices enables lots of flexibilities in pupil design. This problem again becomes an "inverse problem", i.e. one is required to design a subwavelength 3D pupil, giving the input–output relationship, desired PSF, or required system functionality. We could use a similar approach as the one presented in Chapter 3, to first locate the permittivity or refractive index distribution of the 3D pupil. From this a final device

structure design is straightforward based on the analytical or numerical approaches presented in Chapter 5 & 6. Inverse problem and optimization, though interesting and very helpful, are always hard problems and difficult to tackle. Starting from simple designs is important and can potentially shed lights on future complicated ones. In addition, ray tracing can be used to aid this process. Ray tracing, given its pleasing advantages of physical intuitions and computational efficiency, is a good candidate to be used as an intermediate step for converting the input–output relationship to the final permittivity distribution.

Furthermore, subwavelength devices do not have to be restricted in manipulating optical fields only. Proper deformation of the structure (similar to the volume hologram deformation in diffractive regime) further enriches design possibilities. Thus, *in vivo* adjustment of optical properties can also be realized for subwavelength 3D pupils.

Bibliography

[1] *Manufacturable Gradient Index Optics (M-GRIN).* Broad Agency Announcement, Defense Advanced Research Projects Agency, 2010.

[2] M. Abramowitz and I. A. Stegun. *Handbook of mathematical functions: with formulas, graphs, and mathematical tables.* Dover Publications, 1965.

[3] V. M. Agranovich, Y. R. Shen, R. H. Baughman, and A. A. Zakhidov. Linear and nonlinear wave propagation in negative refraction metamaterials. *Physical Review B*, 69(16):165112, 2004.

[4] A. Akbarzadeh and A. J. Danner. Generalization of ray tracing in a linear inhomogeneous anisotropic medium: a coordinate-free approach. *Journal of the Optical Society of America A.*, 27(12):2558–2562, Dec 2010.

[5] R. Anthony. Observation of non-rayleigh scattering in the spectrum of the day sky in the region 0.56 to 2.2 microns. *Journal of Atmospheric Sciences*, 10:60–63, 1953.

[6] G. Barbastathis. Imaging properties of three-dimensional pupils. In *Computational Optical Sensing and Imaging*, page CMC4. Optical Society of America, 2005.

[7] G. Barbastathis, M. Balberg, and D. J. Brady. Confocal microscopy with a volume holographic filter. *Optics Letters*, 24(12):811–813, Jun 1999.

[8] G. Barbastathis and D. J. Brady. Multidimensional tomographic imaging using volume holography. *Proceedings of the IEEE*, 87(12):2098–2120, 1999.

[9] G. Barbastathis, F. Mok, and D. Psaltis. Non-volatile readout of shift multiplexed holograms, 1999. US Patent 5,978,112.

[10] G. Barbastathis and D. Psaltis. Shift-multiplexed holographic memory using the two-lambda method. *Optics Letters*, 21(6):432–434, 1996.

[11] G. Barbastathis and D. Psaltis. Volume holographic multiplexing methods. *Holographic data storage*, pages 21–62, 2000.

[12] G. Barbastathis, B. Zhang, H. Xu, H. Gao, Y. Luo, H. Sun, C. W. Qiu, and T. Han. Affine transformational optics. In *Laser Science*, page LWD3. Optical Society of America, 2011.

[13] W. L. Barnes, A. Dereux, and T. W. Ebbesen. Surface plasmon subwavelength optics. *Nature*, 424(6950):824–830, 2003.

[14] Z. Bomzon, G. Biener, V. Kleiner, and E. Hasman. Radially and azimuthally polarized beams generated by space-variant dielectric subwavelength gratings. *Optics Letters*, 27(5):285–287, 2002.

[15] M. Born, E. Wolf, and A. B. Bhatia. *Principles of optics: electromagnetic theory of propagation, interference and diffraction of light*. Cambridge Univ Pr, 1999.

[16] V. A. Borovikov. *Uniform stationary phase method*. London: Institution of Electrical Engineers, 1994.

[17] V. A. Borovikov and B. Y. Kinber. *Geometrical theory of diffraction*. London: Institution of Electrical Engineers, 1994.

[18] R. Bräuer and O. Bryngdahl. Design of antireflection gratings with approximate and rigorous methods. *Applied Optics*, 33(34):7875–7882, 1994.

[19] L. Burger, I. A. Litvin, and A. Forbes. Simulating atmospheric turbulence using a phase-only spatial light modulator. *South African Journal of Science*, 104(3-4):129–134, 2008.

[20] W. Cai, U. K. Chettiar, A. V. Kildishev, and V. M. Shalaev. Optical cloaking with metamaterials. *Nature Photonics*, 1(4):224–227, 2007.

[21] B. D. F. Casse, W. T. Lu, Y. J. Huang, E. Gultepe, L. Menon, and S. Sridhar. Super-resolution imaging using a three-dimensional metamaterials nanolens. *Applied Physics Letters*, 96(2), 2010.

[22] C.-H. Chang, L. Tian, W. R. Hesse, H. Gao, H. J. Choi, J.-G. Kim, M. Siddiqui, and G. Barbastathis. From two-dimensional colloidal self-assembly to three-dimensional nanolithography. *Nano Letters*, 11(6):2533–2537, 2011.

[23] X. Chen, T. M. Grzegorczyk, B. I. Wu, J. Pacheco Jr, and J. A. Kong. Robust method to retrieve the constitutive effective parameters of metamaterials. *Physical Review E*, 70(1):016608, 2004.

[24] X. Chen, Y. Luo, J. Zhang, K. Jiang, J. B. Pendry, and S. Zhang. Macroscopic invisibility cloaking of visible light. *Nature Communications*, 2:176, 2011.

[25] H. Cheng. *Advanced analytic methods in applied mathematics, science, and engineering*. Boston: LuBan Press, 2007.

[26] Q. Cheng, H. F. Ma, and T. J. Cui. Broadband planar luneburg lens based on complementary metamaterials. *Applied Physics Letters*, 95(18), 2009.

[27] H. J. Choi, H. Gao, L. Tian, C.-H. Chang, J.-G. Kim, C.-H. Hsieh, and G. Barbastathis. Talbot lithography using aperiodic structures. In *Optical MEMS and Nanophotonics (OMN), 2011 International Conference on*, pages 21–22. IEEE, 2011.

[28] S. A. Collins Jr and H. J. Caulfield. Optical holographic interconnects: categorization and potential efficient passive resonated holograms. *Journal of the Optical Society of America A*, 6(10):1568–1577, 1989.

[29] O. M. Conde, J. Pérez, and M. F. Cátedra. Stationary phase method application for the analysis of radiation of complex 3-d conducting structures. *Antennas and Propagation, IEEE Transactions on*, 49(5):724–731, 2001.

[30] J. C. Cooke. Stationary phase in two dimensions. *IMA Journal of Applied Mathematics*, 29(1):25–37, 1982.

[31] H. Cory and C. Zach. Wave propagation in metamaterial multi-layered structures. *Microwave and Optical Technology Letters*, 40(6):460–465, 2004.

[32] A. Degiron, J. J. Mock, and D. R. Smith. Modulating and tuning the response of metamaterials at the unit cell level. *Optics Express*, 15(3):1115–1127, 2007.

[33] G. Dolling, C. Enkrich, M. Wegener, C. M. Soukoulis, and S. Linden. Simultaneous negative phase and group velocity of light in a metamaterial. *Science*, 312(5775):892, 2006.

[34] S. Doric and E. Munro. General solution of the non-full-aperture luneburg lens problem. *Journal of the Optical Society of America*, 73:1083–1086, 1983.

[35] T. Driscoll, H.-T. Kim, B.-G. Chae, B.-J. Kim, Y.-W. Lee, N. M. Jokerst, S. Palit, D. R. Smith, M. Di Ventra, and D. N. Basov. Memory metamaterials. *Science*, 325(5947):1518–1521, September 18 2009.

[36] J. E. Eaton. *An Extension of the Luneburg-Type Lenses*. Rep. No. 4110, Naval Res. Lab., 1953.

[37] N. Engheta and R. W. Ziolkowski. *Metamaterials: Physics and engineering explorations*. Wiley-IEEE Press, 2006.

[38] T. Ergin, N. Stenger, P. Brenner, J. B. Pendry, and M. Wegener. Three-dimensional invisibility cloak at optical wavelengths. *Science*, 328(5976):337, 2010.

[39] N. Fang, D. Xi, J. Xu, M. Ambati, W. Srituravanich, C. Sun, and X. Zhang. Ultrasonic metamaterials with negative modulus. *Nature Materials*, 5(6):452–456, 2006.

[40] S. Feng, Z. Y. Li, Z. F. Feng, B. Y. Cheng, and D. Z. Zhang. Imaging properties of an elliptical-rod photonic-crystal slab lens. *Physical Review B*, 72(7):075101, 2005.

[41] W. M. Folkner and M. H. Finger. Photon statistical limitations for daytime optical tracking. *The Telecommunications and Data Acquisition Progress Report 42-99, July-September 1989*, pages 90–97, 1989.

[42] L. H. Gabrielli, J. Cardenas, C. B. Poitras, and M. Lipson. Silicon nanostructure cloak operating at optical frequencies. *Nature Photonics*, 3(8):461–463, 2009.

[43] J. T. Gallo and C. M. Verber. Model for the effects of material shrinkage on volume holograms. *Applied Optics*, 33(29):6797–6804, 1994.

[44] H. Gao and G. Barbastathis. Design of volume holograpic imaging point spread functions using multiple point deformations. In *Digital Holography and Three-Dimensional Imaging*, page DTu3C. 6. Optical Society of America, 2012.

[45] H. Gao and G. Barbastathis. Volume hologram filter design for mitigation of daytime sky brightness in satellite detection. In *Frontiers in Optics*, page FTh2F.3. Optical Society of America, 2012.

[46] H. Gao and G. Barbastathis. Design and optimization of point spread functions in volume holographic imaging systems. In *Digital Holography and Three-Dimensional Imaging*, page DTh3A. 6. Optical Society of America, 2013.

[47] H. Gao, S. Takahashi, L. Tian, and G. Barbastathis. Nonlinear kerr effect aperiodic lüneburg lens. In *Optical MEMS and Nanophotonics, 2010 International Conference on*, pages 179–180. IEEE, 2010.

[48] H. Gao, S. Takahashi, L. Tian, and G. Barbastathis. Aperiodic subwavelength lüneburg lens with nonlinear kerr effect compensation. *Optics Express*, 19(3):2257–2265, 2011.

[49] H. Gao, L. Tian, and G. Barbastathis. Hamiltonian ray-tracing with wigner distribution function for wave propagation in inhomogeneous media. In *Frontiers in Optics*. Optical Society of America, 2010.

[50] H. Gao, L. Tian, and G. Barbastathis. Hamiltonian and phase-space representation of spatial solitons. *Optics Communications*, 318:199–204, 2014.

[51] H. Gao, L. Tian, B. Zhang, and G. Barbastathis. Iterative nonlinear beam propagation using hamiltonian ray tracing and wigner distribution function. *Optics Letters*, 35(24):4148–4150, 2010.

[52] H. Gao, L. Tian, B. Zhang, and G. Barbastathis. Hamiltonian description of spatial solitons. In *Nonlinear Optics: Materials, Fundamentals and Applications*. Optical Society of America, 2011.

[53] H. Gao, J. M. Watson, J. S. Stuart, and G. Barbastathis. Design of volume hologram filters for suppression of daytime sky brightness in artificial satellite detection. *Optics express*, 21(5):6448–6458, 2013.

[54] H. Gao, J. M. Watson, J. S. Stuart, and G. Barbastathis. Detection of artificial satellites using optimized volume hologram filters. In *Digital Holography and Three-Dimensional Imaging*, page DW5A. 4. Optical Society of America, 2013.

[55] H. Gao, B. Zhang, and G. Barbastathis. A ground-plane cloak made of subwavelength elliptical rod arrays. In *Progress in Electromagnetic Research Symposium*, page 24, 2011.

[56] H. Gao, B. Zhang, and G. Barbastathis. Photonic cloak made of subwavelength dielectric elliptical rod arrays. *Optics Communications*, 2011.

[57] H. Gao, B. Zhang, and G. Barbastathis. Anisotropic guidance correction on the analytical design approach of thin-film photonic lüneburg lens. In *Progress In Electromagnetics Research Symposium*, 2013.

[58] H. Gao, B. Zhang, S. G. Johnson, and G. Barbastathis. Guidance condition correction into the design of two dimensional nanophotonic devices. In *Optical MEMS and Nanophotonics (OMN), 2011 International Conference on*, pages 223–224. IEEE Photonics Society, 2011.

[59] H. Gao, B. Zhang, S. G. Johnson, and G. Barbastathis. Analytical approach for design of thin-film photonic luneburg lens. In *Progress In Electromagnetics Research Symposium*, 2012.

[60] H. Gao, B. Zhang, S. G. Johnson, and G. Barbastathis. Design of thin-film photonic metamaterial lüneburg lens using analytical approach. *Optics Express*, 20(2):1617–1628, 2012.

[61] D. A. Genov, S. Zhang, and X. Zhang. Mimicking celestial mechanics in metamaterials. *Nature Physics*, 5(9):687–692, 2009.

[62] J. M. Gere and B. J. Goodno. *Mechanics of materials, 8th edition*. Cengage Learning, 2012.

[63] H. F. Ghaemi, T. Thio, D. E. Grupp, T. W. Ebbesen, and H. J. Lezec. Surface plasmons enhance optical transmission through subwavelength holes. *Physical Review B*, 58(11):6779, 1998.

[64] J. W. Goodman. *Introduction to Fourier optics*. Roberts and Company Publishers, 2005.

[65] C. Gu, H. Fu, and J.-R. Lien. Correlation patterns and cross-talk noise in volume holographic optical correlators. *Journal of the Optical Society of America A*, 12(5):861–868, 1995.

[66] C. Gu, J. Hong, I. McMichael, R. Saxena, and F. Mok. Cross-talk-limited storage capacity of volume holographic memory. *Journal of the Optical Society of American A*, 9(11):1978–1983, 1992.

[67] A. S. Gutman. Modified luneberg lens. *Journal of Applied Physics*, 25(7):855–859, 1954.

[68] M. Hammer and O. V. Ivanova. Effective index approximations of photonic crystal slabs: a 2-to-1-d assessment. *Optical and Quantum Electronics*, 41(4):267–283, 2009.

[69] T. Han and C. W. Qiu. Isotropic nonmagnetic flat cloaks degenerated from homogeneous anisotropic trapeziform cloaks. *Optics Express*, 18(12):13038–13043, 2010.

[70] P. Hariharan. *Optical Holography: Principles, techniques and applications*. Cambridge University Press, 1996.

[71] J. F. Heanue, M. C. Bashaw, and L. Hesselink. Volume holographic storage and retrieval of digital data. *Science*, 265(5173):749–752, Aug 5 1994. JID: 0404511; ppublish.

[72] E. Hecht. *Optics (4th Edition, Section 6.4)*. Addison-Wesley, 2002.

[73] R. Horstmeyer, S. B. Oh, R. Raskar, and H. Gao. Alternative models of the rotating beam. In *Digital Holography and Three-Dimensional Imaging*, page DWC23. Optical Society of America, 2011.

[74] J. V. Hughes. Sky brightness as a function of altitude. *Applied Optics*, 3(10):1135–1138, 1964.

[75] A. Ishikawa, T. Tanaka, and S. Kawata. Negative magnetic permeability in the visible light region. *Physical Review Letters*, 95(23):237401, 2005.

[76] G. L. James. *Geometrical theory of diffraction for electromagnetic waves*. The Institution of Engineering and Technology, 1979.

[77] Y. Jiao, S. Fan, and D. A. B. Miller. Designing for beam propagation in periodic and nonperiodic photonic nanostructures: Extended hamiltonian method. *Physical Review E*, 70(3):036612, Sep 2004.

[78] J. D. Joannopoulos, S. G. Johnson, J. N. Winn, and R. D. Meade. *Photonic Crystals: Molding the flow of light (2nd Edition)*. Princeton U. P., 2008.

[79] K. L. Johnson. *Contact mechanics*. Cambridge University Press, 1985.

[80] S. G. Johnson and J.D. Joannopoulos. Block-iterative frequency-domain methods for maxwell's equations in a planewave basis. *Optics Express*, 8:173–190, 2001.

[81] J. G. Kim, H. J. Choi, H. Gao, I. Cornago, C. H. Chang, and G. Barbastathis. Mass replication of multifunctional surface by nanoimprint of high aspect ratio tapered nanostructures. In *Optical MEMS and Nanophotonics (OMN), 2012 International Conference on*, pages 71–72. IEEE, 2012.

[82] H. Kogelnik. Coupled wave theory for thick hologram gratings. *Bell System Technical Journal*, 48(9):2909–2947, 1969.

[83] H. Kogelnik. Coupled wave theory for thick hologram gratings. *Bell System Technical Journal*, 48(9):2909–2947, 1969.

[84] J. A. Kong. *Electromagnetic Wave Theory*. EMW Publishing, 2008.

[85] H. Lee, X. Gu, and D. Psaltis. Volume holographic interconnections with maximal capacity and minimal cross talk. *Journal of Applied Physics*, 65:2191, 1989.

[86] U. Leonhardt. Optical conformal mapping. *Science*, 312(5781):1777–1780, June 23 2006.

[87] H. Y. S. Li and D. Psaltis. Three-dimensional holographic disks. *Applied Optics*, 33(17):3764–3774, 1994.

[88] H.-Y. S. Li, Y. Qiao, and D. Psaltis. Optical network for real-time face recognition. *Applied Optics*, 32(26):5026–5035, 1993.

[89] J. Li, Z. Li, and D. Zhang. Effects of shapes and orientations of reversed domains on the conversion efficiency of second harmonic wave in two-dimensional nonlinear photonic crystals. *Journal of Applied Physics*, 102(9):093101–093101–5, 2007.

[90] J. Li and J. B. Pendry. Hiding under the carpet: A new strategy for cloaking. *Physical Review Letters*, 101(20), 2008. Compilation and indexing terms, Copyright 2009 Elsevier Inc.; M1: Compendex.

[91] C. S. Liang, D. A. Streater, J. M. Jin, E. Dunn, and T. Rozendal. A quantitative study of luneberg-lens reflectors. *Antennas and Propagation Magazine, IEEE*, 47(2):30–42, 2005.

[92] R. Liu, C. Ji, J. J. Mock, J. Y. Chin, T. J. Cui, and D. R. Smith. Broadband ground-plane cloak. *Science (New York, N.Y.)*, 323(5912):366–369, Jan 16 2009. JID: 0404511; ppublish.

[93] W. T. Lu and S. Sridhar. Superlens imaging theory for anisotropic nanostructured metamaterials with broadband all-angle negative refraction. *Physical Review B*, 77(23):233101, Jun 2008.

[94] Y.-S. Lu, H. Xu, H. Gao, C. M. Hsieh, B. Zhang, H. Sun, and G. Barbastathis. Design and fabrication of dielectric nanostructured bending adaptor for optical frequencies. In *Optical MEMS and Nanophotonics (OMN), 2012 International Conference on*, pages 172–173. IEEE, 2012.

[95] R. K. Lüneburg. *Mathematical Theory of Optics*. Brown U. P., 1944.

[96] Y. Luo, P. J. Gelsinger, J. K. Barton, G. Barbastathis, and R. K. Kostuk. Optimization of multiplexed holographic gratings in pq-pmma for spectral-spatial imaging filters. *Optics Letters*, 33(6):566–568, 2008.

[97] Y. Luo, I. K. Zervantonakis, S. B. Oh, R. D. Kamm, and G. Barbastathis. Spectrally resolved multidepth fluorescence imaging. *Journal of Biomedical Optics*, 16(9):096015, 2011.

[98] H. F. Ma and T. J. Cui. Three-dimensional broadband ground-plane cloak made of metamaterials. *Nature Communications*, 1(3):1–6, 2010.

[99] H. F. Ma, W. X. Jiang, X. M. Yang, X. Y. Zhou, and T. J. Cui. Compact-sized and broadband carpet cloak and free-space cloak. *Optics Express*, 17:19947–19959, 2009.

[100] C. F. R. Mateus, M. C. Y. Huang, Y. Deng, A. R. Neureuther, and C. J. Chang-Hasnain. Ultrabroadband mirror using low-index cladded subwavelength grating. *Photonics Technology Letters, IEEE*, 16(2):518–520, 2004.

[101] D. T. Moore. Gradient-index optics: a review. *Applied Optics*, 19(7):1035–1038, 1980.

[102] S. B. Oh and G. Barbastathis. Wigner distribution function of volume holograms. *Optics Letters*, 34(17):2584–2586, 2009.

[103] S. B. Oh, Y. Luo, and G. Barbastathis. Psf of 3d pupils: Diffraction tomography formulation. In *Digital Holography and Three-Dimensional Imaging*, page DWE5. Optical Society of America, 2011.

[104] A. Ono, J. Kato, and S. Kawata. Subwavelength optical imaging through a metallic nanorod array. *Physical Review Letters*, 95(26):267407, 2005.

[105] A. F. Oskooi, D. Roundy, M. Ibanescu, P. Bermel, J.D. Joannopoulos, and S. G. Johnson. Meep: A flexible free-software package for electromagnetic simulations by the fdtd method. *Computer Physics Communications*, 181(3):687–702, 2010.

[106] Kyoo-Chul Park, Hyungryul J. Choi, Chih-Hao Chang, Robert E. Cohen, Gareth H. McKinley, and George Barbastathis. Nanotextured silica surfaces with robust superhydrophobicity and omnidirectional broadband supertransmissivity. *ACS Nano*, 6(5):3789–3799, 2012.

[107] J. B. Pendry. Negative refraction makes a perfect lens. *Physcal Review Letters*, 85(18):3966–3969, Oct 2000.

[108] J. B. Pendry, D. Schurig, and D. R. Smith. Controlling electromagnetic fields. *Science*, 312(5781):1780–1782, 2006.

[109] D. Psaltis. Coherent optical information systems. *Science*, 298(5597):1359, 2002.

[110] D. Psaltis, D. Brady, X. G. Gu, and S. Lin. Holography in artificial neural networks. *Nature*, 343(6256):325–330, 1990.

[111] C. Qiu, L. Hu, B. Zhang, B. I. Wu, S. G. Johnson, and J. D. Joannopoulos. Spherical cloaking using nonlinear transformations for improved segmentation into concentric isotropic coatings. *Optics Express*, 17(16):13467–13478, 2009.

[112] A. L. Rivera, S. M. Chumakov, and K. B. Wolf. Hamiltonian foundation of geometrical anisotropic optics. *Journal of the Optical Society of America A*, 12(6):1380–1380, 1995.

[113] D. C. Robertson, A. Berk, and L. S. Bernstein. Modtran: A moderate resolution model for lowtran 7. *Spectral Sciences Inc.*, 1989.

[114] P. S. J. Russel and T. A. Birks. Hamiltonian optics of nonuniform photonic crystals. *Lightwave Technology, Journal of*, 17; 17(11):1982–1988, 1999.

[115] J. M. Russo and R. K. Kostuk. Temperature dependence properties of holographic gratings in phenanthrenquinone doped poly (methyl methacrylate) photopolymers. *Applied Optics*, 46(30):7494–7499, 2007.

[116] S. M. Rytov. Electromagnetic properties of a finely stratified medium. *Soviet Physics JETP-USSR*, 2(3):466–475, 1956.

[117] G. R. Schmidt. Compound optical arrays and polymer tapered gradient index lenses (phd thesis). *University of Rochester*, 2009.

[118] D. Schurig, J. J. Mock, B. J. Justice, S. A. Cummer, J. B. Pendry, A. F. Starr, and D. R. Smith. Metamaterial electromagnetic cloak at microwave frequencies. *Science*, 314(5801):977, 2006.

[119] V. M. Shalaev. Transforming light. *Science*, 322:384–386, 2008.

[120] A. Sinha and G. Barbastathis. Resonant holography. *Optics Letters*, 27(6):385–387, 2002.

[121] A. Sinha and G. Barbastathis. Volume holographic telescope. *Optics Letters*, 27(19):1690–1692, 2002.

[122] A. Sinha and G. Barbastathis. Volume holographic imaging for surface metrology at long working distances. *Optics Express*, 11(24):3202–3209, 2003.

[123] A. Sinha, G. Barbastathis, W. Liu, and D. Psaltis. Imaging using volume holograms. *Optical Engineering*, 43:1959, 2004.

[124] A. Sinha, W. Sun, T. Shih, and G. Barbastathis. Volume holographic imaging in transmission geometry. *Applied Optics*, 43(7):1533–1551, 2004.

[125] D. R. Smith, J. B. Pendry, and M. C. K. Wiltshire. Metamaterials and negative refractive index. *Science*, 305(5685):788, 2004.

[126] D. R. Smith, S. Schultz, P. Markoš, and C. M. Soukoulis. Determination of effective permittivity and permeability of metamaterials from reflection and transmission coefficients. *Physical Review B*, 65(19):195104, 2002.

[127] D. R. Smith, D. C. Vier, T. Koschny, and C. M. Soukoulis. Electromagnetic parameter retrieval from inhomogeneous metamaterials. *Physical Review E*, 71(3):36617, 2005.

[128] D. H. Spadoti, L. H. Gabrielli, C. B. Poitras, and M. Lipson. Focusing light in a curved-space. *Opt.Express*, 18:3181–3186, 2010.

[129] A. Stein and G. Barbastathis. Axial imaging necessitates loss of lateral shift invariance. *Applied Optics*, 41(29):6055–6061, 2002.

[130] C. A. Swainson (alias J. C. Maxwell). Problems. *Cambridge Dublin Math. J.*, 8:188–189, 1854.

[131] S. Takahashi. Design and fabrication of micro-and nano-dielectric structures for imaging and focusing at optical frequencies (phd thesis). *Massachusetts Institute of Technology*, 2011.

[132] S. Takahashi, C.-H. Chang, S. Y. Yang, and G. Barbastathis. Design and fabrication of dielectric nanostructured luneburg lens in optical frequencies. In *Optical MEMS and Nanophotonics, 2010 International Conference on*, pages 179–180. IEEE, 2010.

[133] K. Tian and G. Barbastathis. Resonant holographic imaging in confocal cavities. In *Lasers and Electro-Optics, 2003. CLEO'03. Conference on*. IEEE, 2003.

[134] K. Tian, T. Cuingnet, Z. Li, W. Liu, D. Psaltis, and G. Barbastathis. Diffraction from deformed volume holograms: perturbation theory approach. *JOSA A*, 22(12):2880–2889, 2005.

[135] L. Tian, H. Gao, and G. Barbastathis. Digital holographic imaging of multiphase flows. In *Computational Optical Sensing and Imaging*, page CWB5. Optical Society of America, 2011.

[136] A. Vakil and N. Engheta. Transformation optics using graphene. *Science*, 332(6035):1291, 2011.

[137] J. Valentine, J. Li, T. Zentgraf, G. Bartal, and X. Zhang. An optical cloak made of dielectrics. *Nature Materials*, 8(7):568, 2009.

[138] B. Vasić, G. Isić, R. Gajić, and K. Hingerl. Controlling electromagnetic fields with graded photonic crystals in metamaterial regime. *Optics Express*, 18(19):20321–20333, 2010.

[139] D. H. R. Vilkomerson and D. Bostwick. Some effects of emulsion shrinkage on a holograms image space. *Applied Optics*, 6(7):1270–1272, 1967.

[140] J. M. Watson, P. Wissmann, S. B. Oh, M. Stenner, and G. Barbastathis. Computational optimization of volume holographic imaging systems. In *Computational Optical Sensing and Imaging*. Optical Society of America, 2007.

[141] B. I. Wu, W. Wang, J. Pacheco, X. Chen, T. M. Grzegorczyk, and J. A. Kong. A study of using metamaterials as antenna substrate to enhance gain. *Progress In Electromagnetics Research*, 51:295–328, 2005.

[142] S. Xi, H. Chen, B. I. Wu, and J. A. Kong. One-directional perfect cloak created with homogeneous material. *Microwave and Wireless Components Letters, IEEE*, 19(3):131–133, 2009.

[143] H. Xu, X. Shi, F. Gao, H. Sun, and B. Zhang. Ultrathin three-dimensional thermal cloak. *Physical Review Letters*, 112(5):054301, 2014.

[144] X. Xu, Y. Feng, Y. Hao, J. Zhao, and T. Jiang. Infrared carpet cloak designed with uniform silicon grating structure. *Applied Physics Letters*, 95:184102, 2009.

[145] W. Yu, T. Konishi, T. Hamamoto, H. Toyota, T. Yotsuya, and Y. Ichioka. Polarization-multiplexed diffractive optical elements fabricated by subwavelength structures. *Applied Optics*, 41(1):96–100, 2002.

[146] T. Zentgraf, J. Valentine, N. Tapia, J. Li, and X. Zhang. An optical "janus" device for integrated photonics. *Advanced Materials*, 22(23):2561–2564, 2010.

[147] B. Zhang, T. Chan, and B. I. Wu. Lateral shift makes a ground-plane cloak detectable. *Physical Review Letters*, 104(23):233903, 2010.

[148] B. Zhang, Y. Luo, X. Liu, and G. Barbastathis. Macroscopic invisibility cloak for visible light. *Physical Review Letters*, 106(3):033901, 2011.